

**GAAT (SOCKEYE SALMON, *ONCORHYNCHUS NERKA*) MIGRATION UP THE
GAAT HÉENI (SILVER SALMON RIVER): INFLUENCE OF ATMOSPHERIC
RIVERS ON HYDROLOGIC VARIABILITY**

by

Devin Wittig

B.Kin., University of Alberta, 2016

B.Ed., Yukon University, 2022

THESIS SUBMITTED IN PARTIAL FULFILLMENT OF
THE REQUIREMENTS FOR THE DEGREE OF
MASTER OF SCIENCE
IN
NATURAL RESOURCES AND ENVIRONMENTAL STUDIES

UNIVERSITY OF NORTHERN BRITISH COLUMBIA

July 2025

© Devin Wittig, 2025

Committee Members

Supervisor: Stephen Déry. PhD

Department of Geography, Earth and Environmental Sciences

University of Northern British Columbia

Prince George, Canada

Committee Member: Peter Jackson. PhD

Department of Geography, Earth and Environmental Sciences

University of Northern British Columbia

Prince George, Canada

Committee Member: Jonathan Moore. PhD

Biological Science (Primary) and Resource and Environmental Management

Simon Fraser University

Vancouver, Canada

Abstract

Atmospheric rivers (ARs) drive hydrometeorological variability, influencing precipitation, river discharge and water temperature. This study quantifies how ARs contribute to precipitation and hydrology in the Gaat Héeni (Silver Salmon River) Watershed, a key migration corridor for Sockeye Salmon. I integrate ERA5-Land reanalysis and the SIO-R1 AR catalog with in-situ hydrometric measurements and biological monitoring data, including video observations at a waterfall barrier and escapement counts from a weir. This approach enables me to evaluate how AR-driven changes in hydrologic conditions subsequently influence Sockeye Salmon migration success.

Sockeye Salmon jump success, modelled using logistic regression, was primarily influenced by river discharge, with peak success occurring at 10–12 m³ s⁻¹ discharge levels. Jump success at SR3-3 declined at discharge levels above 16 m³ s⁻¹ or below 9 m³ s⁻¹. Although water temperatures of 13–15 °C coincided with optimal jump success, water temperature was not a statistically significant predictor, reducing confidence in its influence relative to discharge.

Results show that AR events contributed between 15.9% and 39.1% of seasonal precipitation from 1991 to 2023, with the highest contributions in fall (37.9%) and winter (24.1%). During the 2024 monitoring season, an AR event on 22–24 July triggered a discharge surge from 8.7 to 30.0 m³ s⁻¹ within two days, reflecting the watershed's rapid hydrologic response. Centroid lag analysis revealed a median discharge lag of 1.6 days following AR-driven precipitation, underscoring the sensitivity of discharge timing to ARs.

Table of Contents

Committee	ii
Abstract.....	iii
Table of Contents.....	iv
List of Tables.....	vi
List of Figures.....	vii
Acknowledgments.....	ix
Glossary.....	x
Chapter 1: INTRODUCTION.....	1
1.1 Territorial Acknowledgement	1
1.2 Motivation.....	1
1.3 Gaat Héeni Watershed Physiography	3
1.4 Objectives	6
1.5 Thesis Structure	7
Chapter 2: LITERATURE REVIEW.....	8
2.1 Changing Climate	8
2.2 Meteorological Phenomena	10
2.3 Reanalysis Products	13
2.4 Gaat Physiology	14
2.5 Effects of Hydrologic Variability on Gaat.....	17
2.6 Effects of Changing Water Temperature	20
Chapter 3: DATA.....	22
3.1 Reanalysis Data.....	22
3.2 Meteorological Data.....	22
3.3 Hydrologic Data	24
3.4 SIO-R1 Atmospheric River Catalog.....	24
3.5 Escapement Data.....	25

Chapter 4: METHODS	26
4.1 Installation of Meteorological Station	27
4.2 Extraction and Validation of Reanalysis Data	28
4.3 Climatology of the Gaat Héeni Watershed	31
4.4 Atmospheric River Climatology	32
4.5 Impact of ARs on the Study Region	33
4.6 Discharge Sensitivity to Daily Precipitation and AR Events.....	35
4.7 Quantifying Optimal Hydrological Conditions for Successful Gaat Barrier Passage	38
4.8 Influence of Jump Success on Gaat arrival at Gaat Áayi.....	42
 Chapter 5: RESULTS	 44
5.1 Meteorological Data.....	44
5.2 Extraction and Validation of Reanalysis Data	47
5.3 Climatology of Study Region	51
5.4 Atmospheric River Climatology	56
5.5 Impact of ARs on the study region	58
5.6 Discharge Sensitivity to Daily Precipitation and AR Events.....	62
5.7 Quantifying Optimal Hydrological Conditions for Successful Gaat Barrier Passage	64
5.8 Influence of Jump Success on daily Gaat arrival at Gaat Áayi.....	67
 Chapter 6: DISCUSSION	 69
6.1 Contribution of ARs to Seasonal and Annual Precipitation	69
6.2 The Impact of Changing Atmospheric River Patterns on Gaat	70
6.3 Hydrological thresholds for Gaat Arrival at Gaat Áayi	72
6.4 Evaluating the Effectiveness of Video Monitoring for Assessing Fish Passage Success	75
 Chapter 7: CONCLUSION	 76
7.1 Summary	76
7.2 Study Limitations.....	80
7.3 Future Direction	82
 REFERENCES	 85

List of Tables

Table 3.1: Meteorological Station Metadata.....	23
Table 3.2: Hydrologic Station Metadata	24
Table 5.1: Wald Z-Test Results for Hydrologic Predictors of Gaat Jump Success at SR3-3.....	67

List of Figures

Figure 1.1 Map of Gaat Héeni Watershed and Regional Context	2
Figure 1.2: Annual Gaat Áayi Escapement Totals, 1980–2022	3
Figure 1.3: Photograph of SR3-3	5
Figure 1.4: Taku River Daily Discharge, January 2018–December 2020	6
Figure 2.1: Schematic of Atmospheric River Structure and Intensity	10
Figure 2.2: Lower Llewellyn Daily Rainfall 2013-2023	12
Figure 2.3: Snow Water Equivalent Across Yukon and Northwestern BC	13
Figure 4.1: Gaat Héeni Meteorological Station Installation	28
Figure 4.2: Flowchart showing methods for Section 4.7	38
Figure 4.3: Laminar Flow Zone Within the SR3-3 Channel.....	39
Figure 5.1: Daily Meteorological and Hydrological Observations at Gaat Héeni	46
Figure 5.2: Validation of ERA5-Land Temperature Data	47
Figure 5.3: Validation of ERA5-Land Snow Water Equivalent Data	48
Figure 5.4: Validation of ERA5-Land Snow Depth Data	49
Figure 5.5: Validation of ERA5-Land Daily Precipitation Data	50
Figure 5.6: Validation of ERA5-Land Monthly Precipitation Data	51
Figure 5.7: Monthly Temperature Distribution in the Gaat Héeni Watershed	52
Figure 5.8: Monthly Snow Water Equivalent in the Gaat Héeni Watershed.....	53
Figure 5.9: Monthly Snow Depth for the Gaat Héeni Watershed.....	53
Figure 5.10: Annual Precipitation Distribution in the Gaat Héeni Watershed	54
Figure 5.11: Monthly Distribution of Total Precipitation, Snowfall, and Rainfall	55
Figure 5.12: Monthly Atmospheric River Frequency and Net IVT	56

Figure 5.13: Atmospheric River Monthly Distribution and Net IVT	57
Figure 5.14: Monthly Distribution of Atmospheric River Separated by Decade	58
Figure 5.15: Seasonal Precipitation Attributed to ARs in the Gaat Héeni Watershed	59
Figure 5.16: Annual Precipitation Attributed to ARs in the Gaat Héeni Watershed	60
Figure 5.17: Monthly Precipitation Attributed to ARs in the Gaat Héeni Watershed.....	61
Figure 5.18: Mann-Kendall Trend Analysis: Precipitation in the Gaat Héeni Watershed	61
Figure 5.19: Monthly Contribution of ARs to Total Precipitation, June-October 2024	63
Figure 5.20: Daily Discharge and Precipitation, June-October, 2025	64
Figure 5.21: Daily Number of Jump Attempts at SR3-3, July 2024	65
Figure 5.22: Predicted Jump Success Dependent on Discharge and Water Temperature	66

Acknowledgements

Gunalchéesh, thank you (Tlingit Language, 2024), to the Taku River Tlingit First Nation (TRTFN) for supporting this research on their traditional and unceded territory. TRTFN has stewarded this land for time immemorial, and I hope my research contributes to its continued stewardship. I would also like to thank Mark Connor, Dr. Stephen Déry, Dr. Peter Jackson, Dr. Jonathan Moore, Dr. Eran Hood, Lisa Rickard, Robin Brand, Dr. Christopher Sergeant, Brittany Milner, Dr. Bruno Sobral, Tawni Drinnan, and any reviewers I may have missed for their time and efforts. I would also like to thank funders, including the Natural Sciences and Engineering Research Council of Canada, through a Discovery Grant, Polar Research Canada, and the Council of Yukon First Nations, for their support.

Glossary

Atmospheric River (AR): A synoptic-scale corridor of intense moisture transport (>1500 km), linked to extratropical cyclones and strong low-level winds.

ERA5-Land: A high-resolution (0.1°) reanalysis dataset from the European Centre for Medium-Range Weather Forecasts (ECMWF), reconstructing historical land-atmosphere interactions.

Escapement: The proportion of Salmon that successfully migrate upstream to spawn is provided at an annual timescale.

Gaat (Sockeye Salmon; *Oncorhynchus nerka*): A keystone anadromous salmonid in the Taku River Basin, highly sensitive to hydrological shifts.

Gaat Héeni (Silver Salmon River): The river addressed in this research serves as a critical migration corridor for Gaat.

Gaat Áayi (Silver Salmon Lake): A primary spawning habitat within the Taku River Basin and the spawning location of Gaat migrating up the Gaat Héeni. It holds high ecological and cultural significance as the only lake-spawning habitat accessible by the Taku River Tlingit First Nation without aircraft.

Integrated Water Vapour Transport (IVT): A standardized metric quantifying atmospheric moisture flux ($\text{kg m}^{-1} \text{s}^{-1}$) to classify AR strength and assess precipitation potential.

Optimal Passage Conditions: The hydrometric thresholds defining the discharge and water temperature ranges that maximize Gaat migration success.

SIO-R1 Atmospheric River Catalog: A dataset from Scripps Institution of Oceanography tracking AR landfalls along the North American West Coast.

SR3-3: A hydrodynamic barrier within the Gaat Héeni canyon, featuring obstructions and high turbulence that hinder Gaat passage.

Chapter 1: INTRODUCTION

1.1 Territorial Acknowledgement

I begin by acknowledging that the land on which this research occurred is the traditional and unceded territory of the Taku River Tlingit First Nation (TRTFN).

1.2 Motivation

The motivation for this project is rooted in the unique characteristics of the Gaat Héeni River (Silver Salmon River; Figure 1.1). The Gaat Héeni River, characterized by its steep canyon constriction, multiple natural barriers, continuous meteorological and hydrometric monitoring, and a multi-decadal record of culturally significant Gaat (Sockeye Salmon; *Oncorhynchus nerka*) escapement, provides an opportunity to quantify how atmospheric rivers (ARs) drive hydrologic variability and influence migration success.

Gaat Áayi (Kuthai Lake), one of the four major Gaat spawning lakes in the Taku River Watershed, is critical to TRTFN and is the location of one of their focal Gaat monitoring programs. As the only spawning lake TRTFN can access without aircraft, Gaat Áayi has high cultural and food security value. From 2006 to 2023, the number of Gaat reaching Gaat Áayi remained low, with partial run collapses in 2018 and 2021. In contrast, 2024 exhibited a marked resurgence, with a record escapement of 13,375 Gaat (Figure 1.2). Field work by the TRTFN Fisheries Department has determined that the canyon in the lower Gaat Héeni presents a migration barrier to Gaat under both low and high discharge (Taku River Tlingit Fisheries Department, 2017). Additionally, observations from TRTFN fisheries staff have shown an increase in the frequency with which the Gaat Héeni Watershed experiences these low and high discharge conditions (Taku River Tlingit Fisheries Department, 2019).



Figure 1.1: Map illustrating the extent of the Gaat Héeni Watershed (grey polygon) in northwestern British Columbia, Canada. Key monitoring infrastructure is highlighted, including meteorological (orange triangles), snow survey (blue circles), and video monitoring (green squares) stations. The inset map (top right) shows the study area's location within the broader context of British Columbia and the Yukon border region.

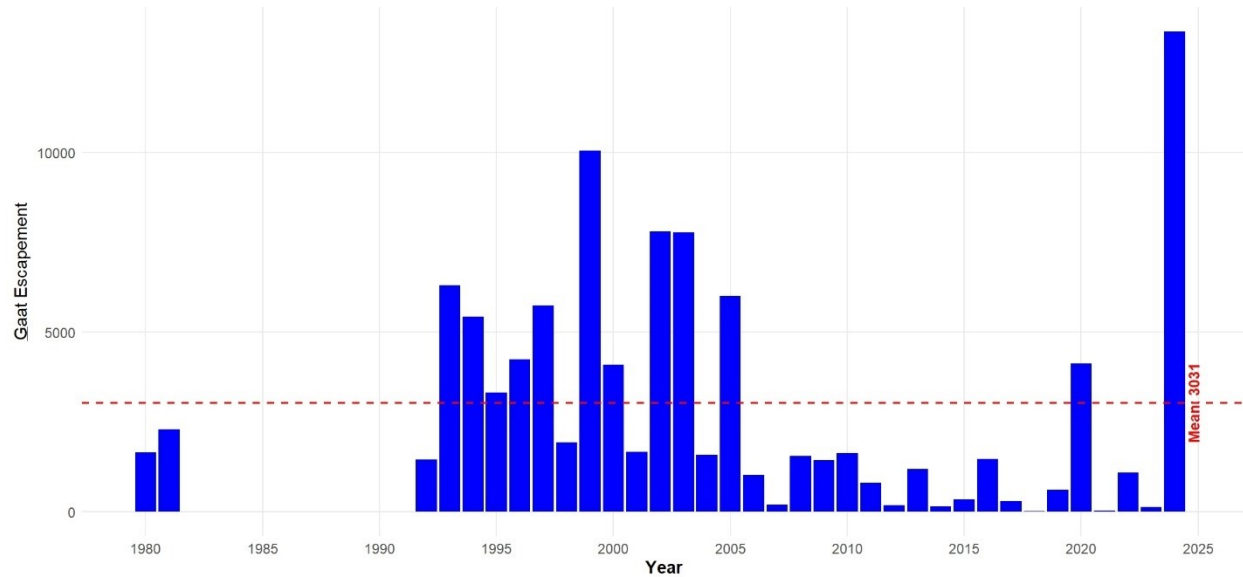


Figure 1.2: Annual escapement of Gaat (*Oncorhynchus nerka*) into Gaat Áayi from 1980 to 2024. Gaat Áayi is the only major spawning lake in the Taku River Watershed accessible to the Taku River Tlingit First Nation without aircraft. Escapement has remained consistently low from 1991-2023, with near collapses in 2018 (13) and 2021 (26). In contrast, 2024 recorded the highest escapement on record, with 13,375 Gaat returning to spawn. No escapement data were collected from 1982 to 1991.

The selection of this region for my work is driven by the limited research coverage on ARs and impacts on meteorological variables in the area, the potential impact of ARs to the hydrology of the Gaat Héeni, and the effect of river discharge and water temperature on Gaat. The presence of the Gaat Héeni canyon as a significant migration obstacle for Gaat (Taku River Tlingit Fisheries Department, 2022), further underscores the importance of investigating the influence of ARs on hydrologic conditions in the region. By examining the impacts of ARs on Gaat migration and hydrologic variability, the study aims to contribute to the conservation of culturally important Gaat populations and inform management strategies in the face of changing environmental conditions.

1.3 Gaat Héeni Watershed Physiography

The Gaat Héeni Watershed lies on the lee side of the Coast Mountains, resulting in lower precipitation and runoff compared to more western watersheds (Taku River Tlingit Fisheries Department, 2017). Gaat Áayi, shaped by subglacial processes, has substrates of chert,

limestone, and argillite (Aitken, 1958) favorable for Gaat spawning (Eiler et al., 1992).

Downstream of Gaat Áayi, Gaat Héeni meanders through an alluvial deposit, creating large groundwater aquifers that enhance conditions for Gaat spawning and rearing (Taku River Tlingit Fisheries Department, 2017). For the final 700 m before its confluence with the Nakina River, Gaat Héeni descends steeply through a canyon characterized by multiple geomorphic barriers, including the obstruction designated as SR3-3 (Taku River Tlingit Fisheries Department, 2017; Figure 1.3).

The Gaat Héeni canyon is divided into three sub-reaches (Taku River Tlingit Fisheries Department, 2017) based on geomorphic features and channel obstructions that influence water flow and fish movement. The first segment, Sub-reach 1 (SR1), extends approximately 150 m upstream from the Nakina River confluence. It is a boulder channel comprising a series of pools with a gradient of about 11%, tightly confined by bedrock and large boulders (Taku River Tlingit Fisheries Department, 2017). Sub-reach 2 (SR2) has a length of around 420 m with a gentler gradient of 4% and does not present any significant migration barriers (Taku River Tlingit Fisheries Department, 2017). The final segment, Sub-reach 3 (SR3), represents the upper canyon portion, extending for approximately 110 m with an 11% slope (Taku River Tlingit Fisheries Department, 2017). Segment SR3 contains five rated obstacles; SR3-3 is the most pronounced, serving as the principal geomorphic constraint. SR3-3 consists of a protruding drop with the vertical height between pools being approximately 2.5 m (Taku River Tlingit Fisheries Department, 2017).



Figure 1.3: Photograph of SR3-3, the primary hydraulic barrier in the Gaat Héeni canyon. SR3-3 consists of a cascading drop with a vertical separation of approximately 2.5 m between pools (Taku River Tlingit Fisheries Department, 2022).

Except for its alpine ridges and scattered wetlands, the Gaat Héeni Watershed is largely forested and spans an elevation gradient of 303 m to 1766 m. Lacking long-term hydrometric stations, hydrologic parameters are calculated by utilizing reanalysis data (Section 3.1). United States Geological Survey (2024) data for the Taku River, a station near Juneau, Alaska, highlights typical spring snowmelt runoff and fall storm-influenced high flows, excluding summer glacial outbursts (Figure 1.4).

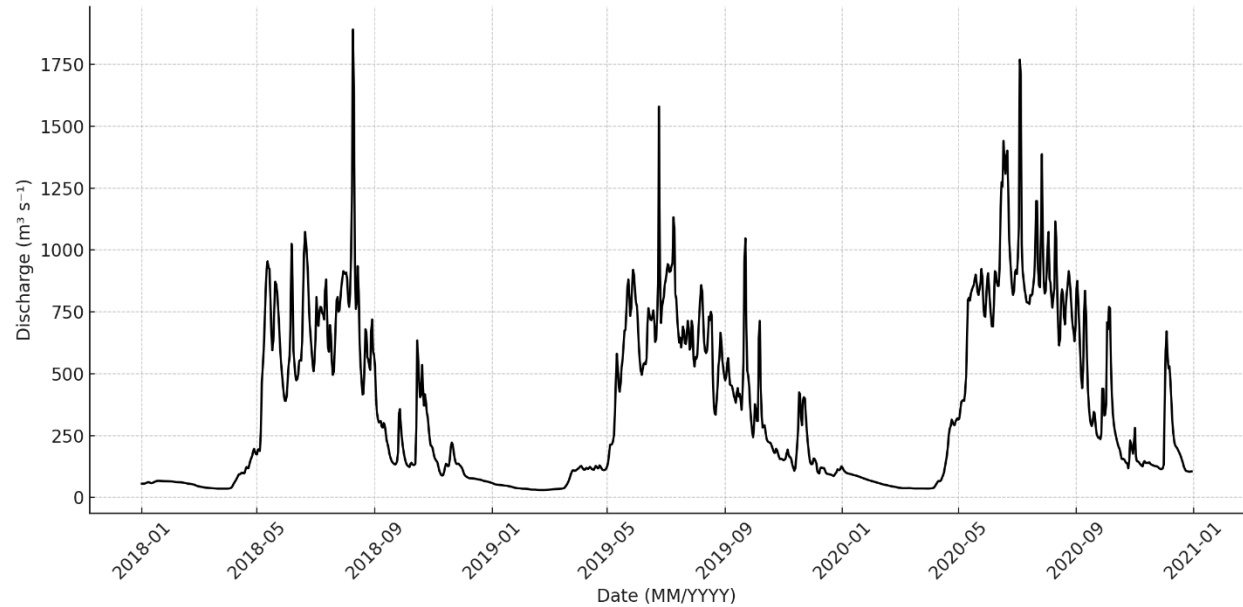


Figure 1.4: Hourly discharge ($\text{m}^3 \text{s}^{-1}$) from the Taku River near Juneau, Alaska, recorded by the United States Geological Survey (USGS) between 2018 and 2020. The hydrograph reveals a consistent seasonal pattern dominated by spring snowmelt and late summer to fall rainfall events. Discharge exceeds $1000 \text{ m}^3 \text{s}^{-1}$ multiple times yearly, reflecting contributions from snowmelt and intense precipitation events. (United States Geological Survey, 2024)

1.4 Objectives

The objectives of this research are:

1. To assess the contribution of ARs to meteorological variables within the Gaat Héeni Watershed.
2. To identify the water temperature and river discharge conditions that allow for the successful transit of Gaat to Gaat Áayi.
3. To provide fisheries managers with tools to identify impactful flow and/or water temperature values.

1.5 Thesis Structure

This thesis is structured into seven chapters, each contributing to the discussion of how ARs influence hydrological variability and Gaat migration. Chapter 2 provides a literature review covering AR dynamics, climate change, and hydrological variability, emphasizing the role of ARs in shaping freshwater ecosystems and Gaat migration. It also examines the strengths and limitations of reanalysis datasets, including the ERA5-Land reanalysis product. Chapter 3 outlines the datasets used within this work, including ERA5-Land (Muñoz-Sabater et al., 2021), in-situ meteorological and hydrometric data from stations within the Gaat Héeni Watershed, the SIO-R1 AR catalog (Gershunov et al., 2017) and escapement records from the Taku River Tlingit First Nation Fisheries Department. Chapter 4 validates ERA5-Land reanalysis data against in-situ observations, outlines the analytical methods used to identify AR events, quantifies their effects on discharge and precipitation, and models how discharge and water temperature influence Gaat migration success. Chapter 5 presents the results, including validation of ERA5-Land precipitation and temperature data, characterization of AR climatology and impacts in the study region, analysis of AR-driven changes in daily precipitation and discharge, and statistical relationships between AR-driven hydrologic variability and Gaat migration. Chapter 6 discusses these findings in the context of hydrological change, fisheries management, and Gaat conservation. Finally, Chapter 7 synthesizes the thesis's key conclusions, limitations, and future direction.

Chapter 2: LITERATURE REVIEW

This literature review examines hydrometeorological factors shaping hydrological variability and Gaat escapement. The review begins by exploring the impacts of climate change, including shifting temperature regimes, altered precipitation patterns, and evolving snowmelt dynamics. It subsequently analyzes ARs, discussing climatology, moisture transport mechanisms, and influence on precipitation and river discharge. The review then explores the impacts of climate change, including shifting temperature regimes, altered precipitation patterns, and evolving snowmelt dynamics. It also evaluates the applicability and limitations of reanalysis products, such as ERA5-Land, in modelling hydrometeorological trends. Additionally, it investigates Gaat physiology, focusing on metabolic constraints, behavioural adaptations, and environmental stressors affecting migration. Finally, the literature review synthesizes research on the effect of river discharge and water temperature on Gaat.

2.1 Changing Climate

Climate change is a long-term alteration in climate patterns, identifiable through statistical analysis of changes in mean and variability of climate properties, persisting for decades or longer (IPCC, 2025). It can result from natural processes, such as volcanic eruptions (Gerlach, 2011), or anthropogenic influences, notably increasing greenhouse gas concentrations and land use changes (Wood et al., 2023). These changes manifest as rising global temperatures, altered precipitation patterns, and more frequent extreme weather events (Frandsen & Hasselbalch, 2024).

Climate change is significantly affecting British Columbia, Southeast Alaska, and Yukon (BCSAKY), particularly through shifts in temperature, snowfall, and precipitation patterns

(Fraser & Jackson, 2018; Hawcroft et al., 2012). Rising temperatures are causing earlier spring thaws and shifting vegetation dynamics, with projections indicating a 3.9–6.9 °C increase in mean air temperature from 1961–1990 by the end of the twenty-first century (Reid et al., 2022; SNAP-EWHALE, 2012). Warming also alters snow accumulation and melt timing (Foster et al., 2016). The proportion of rain and rain-on-snow events is accelerating, leading to reduced spring snowpack and earlier melts (Arora et al., 2025; Thériault et al., 2023), which heightens spring flood risks and reduces water availability in drier months (Hay & McCabe, 2010; Foster et al., 2016). Additionally, increased rainfall intensity is expected to exacerbate flooding and disrupt ecological systems reliant on stable precipitation patterns (Hay & McCabe, 2010).

The Yukon River, whose headwaters lie adjacent to the Gaat Héeni Watershed, is experiencing rapid climate change, with rising precipitation and air temperatures (Hay & McCabe, 2010).

Higher water temperatures are inducing heat stress in Chinook Salmon (*Oncorhynchus tshawytscha*) during spawning migrations (Cunningham et al., 2018; Howard & Von Biela, 2023). These changes are impacting both freshwater ecosystems and marine habitats in the Pacific Ocean bordering the BCSAKY region (Feddern et al., 2023).

2.2 Meteorological Phenomena

The meteorological phenomenon examined in this thesis is the atmospheric river (Figure 2.1).

ARs are defined as elongated (>1500 km) bands of atmospheric moisture transport, typically associated with strong low-level winds ahead of the cold front of an extratropical cyclone (Gimeno et al., 2012; Gomis-Cebolla et al., 2023; Ralph et al., 2020; Sharma & Déry, 2020). A key characteristic of ARs is their high integrated water vapour transport (IVT), which quantifies the total water vapour flux through a vertical column of the atmosphere. Studies have established an IVT threshold of $\geq 250 \text{ kg m}^{-1} \text{ s}^{-1}$ for AR classification (Espinoza et al., 2018; Gershunov et al., 2017; Ralph et al., 2019).

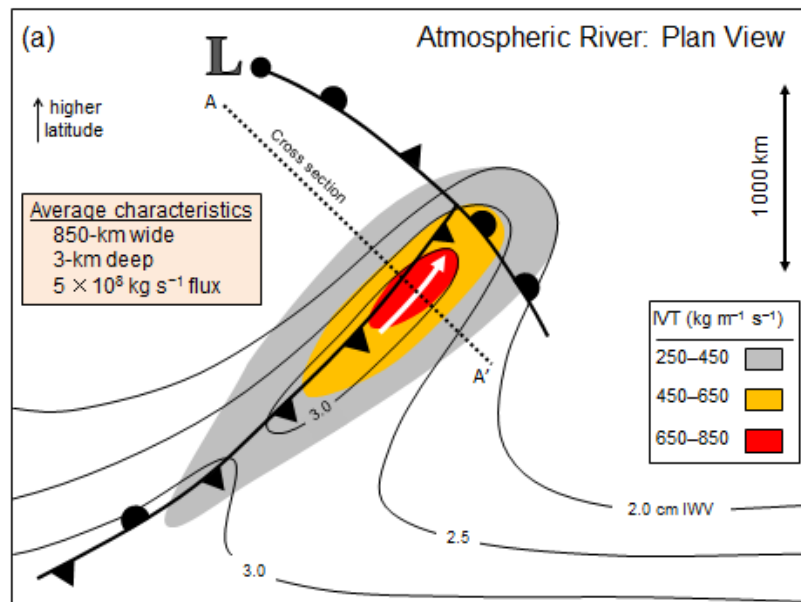


Figure 2.1: Schematic summary of the structure and strength of an atmospheric river, illustrating integrated water vapour transport (IVT) and integrated water vapour (IWV; Glossary of Meteorology, 2022). ARs are narrow corridors of intense moisture flux, typically >1500 km in length, linked to extratropical cyclones and low-level jets.

Strong low-level winds in ARs often precede the cold fronts of extratropical cyclones, influencing weather patterns and precipitation (Payne et al., 2020). These winds enhance moisture transport in the lower troposphere, where ARs interact with the low-level jet stream (Park et al., 2021). When moist air is lifted over topography or converges with frontal systems,

extreme precipitation can result (Lavers et al., 2020). Additionally, extratropical cyclones facilitate the development of low-level jets, which transport warm, moist air from the tropics into mid-latitudes (Guo et al., 2020). This interaction drives heavy precipitation and intensifies cyclogenesis, reinforcing storm development (Eiras-Barca et al., 2018). Understanding these processes is essential for understanding the formation of ARs (Lavers et al., 2020).

ARs provide significant contributions to total precipitation (Sharma & Déry, 2020) and fluctuations in river discharge (Dettinger, 2011; Ralph et al., 2020). Landfalling ARs trigger increases in river discharge, often producing rapid runoff and flooding in affected basins (Ralph et al., 2019). Within the British Columbia and southeastern Alaska (BCSAK) region, ARs contribute between 11% to 22% of river runoff (Sharma & Déry, 2020). Moreover, these events can elevate runoff levels by 12.5 times compared to non-AR-related runoff (Zhou et al., 2025). The heightened runoff accelerates water transport into river systems, resulting in elevated discharge levels (Davie & Quinn, 2019). ARs also contribute between 5% and 33% of total precipitation in the BCSAK region (Sharma & Déry, 2020). As the frequency of ARs increases, particularly in the fall season, their associated precipitation is expected to rise through 2100 (Radić et al., 2015). These shifts are likely to heighten the risk of flooding and other hydrological hazards, with significant environmental and societal consequences (Rahman et al., 2023). This finding is corroborated by Sobral & Déry (2024), who reported that ARs significantly influenced the water budget in the Nechako River Watershed, situated in northern British Columbia. Their study revealed that ARs account for 21% of the basin's annual precipitation, with contributions reaching up to 45% of seasonal rainfall and 24% of seasonal snowfall.

Data provided by Sagar (2023) and supported by the SIO-R1 AR Catalog (Gershunov et al.,

2017) identified an AR event on 1 December 2020 at the Llewellyn Glacier weather station (Figure 2.2). This event resulted in 106.6 mm of rain at Llewellyn Glacier (Sagar, 2023). This observed AR may have contributed to the 209% of seasonal Snow Water Equivalent (SWE; Figure 2.3) seen in Atlin during March 2021 (Kolot et al., 2021).

TRTFN Fisheries observed elevated flows through the Gaat Héeni canyon during the 2021 Gaat migration period, which may have resulted from the earlier AR event and subsequent snowpack conditions.

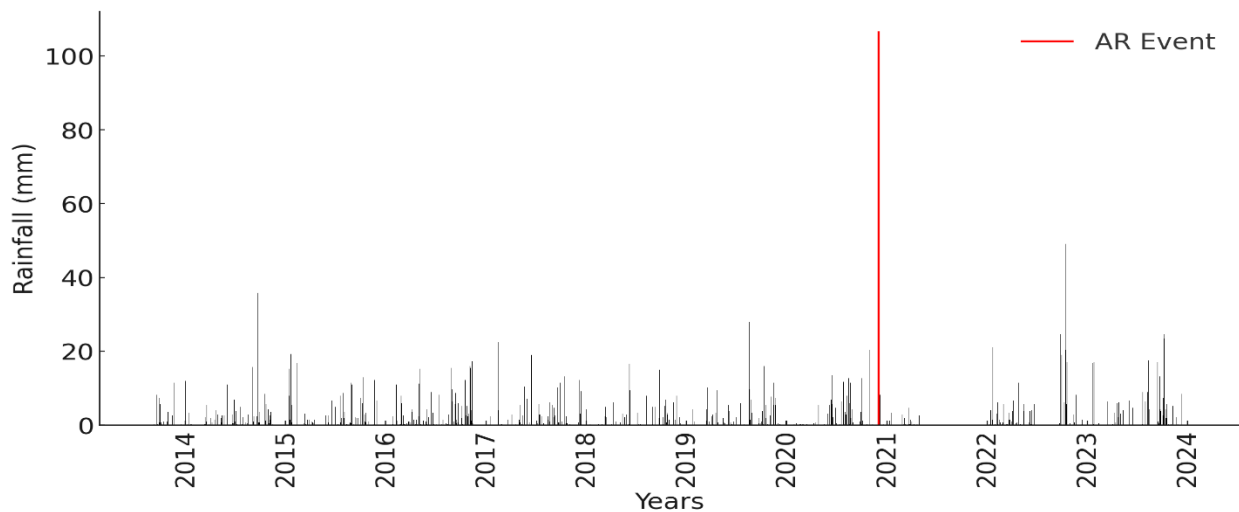


Figure 2.2: Time series of daily rainfall (mm) recorded at the Llewellyn Glacier meteorological station. An atmospheric river event on 1 December 2020 delivered 106.6 mm of rainfall (Sagar, 2023).

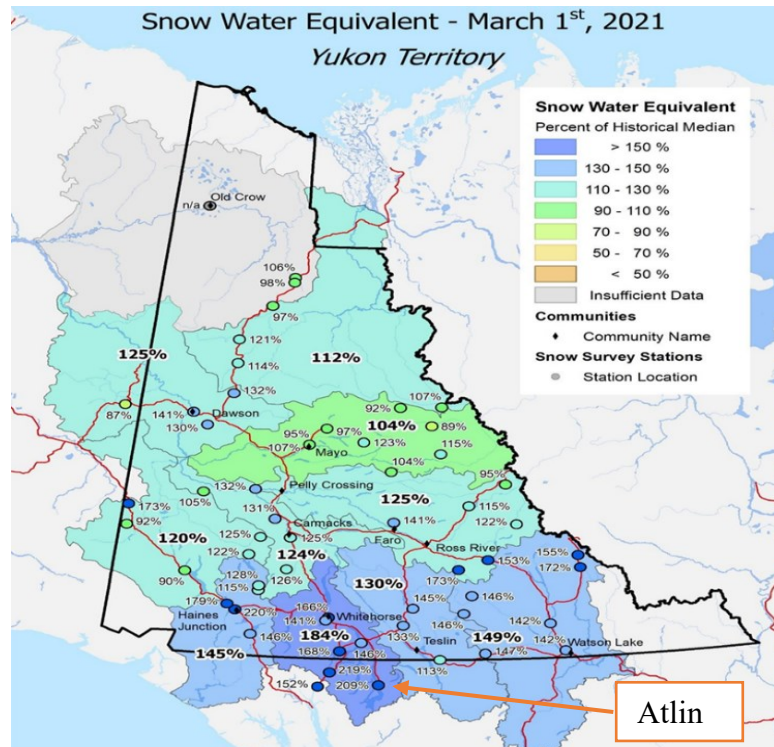


Figure 2.3: Spatial distribution of snow water equivalent (SWE) as a percentage of the historical median across Yukon Territory. SWE values in the southern and central Yukon were substantially above average, with widespread measurements exceeding 130%. Elevated SWE in Atlin, 209% of seasonal, indicates deep snowpack storage potential preceding the spring freshet (Kolot et al., 2021).

2.3 Reanalysis Products

Reanalysis products are comprehensive datasets that provide a detailed record of various meteorological and surface variables over a historical period. These products integrate model data with in-situ observations, including ground-based and satellite measurements, to produce a consistent global dataset (Hersbach et al., 2020). Reanalysis products such as ERA5 (Hersbach et al., 2020), ERA5-Land (Muñoz-Sabater et al., 2021), CaSPAr (Mai et al., 2020), Daymet (Thornton et al., 2022), and ClimateNA (Wang et al., 2016) provide comprehensive datasets for meteorological and surface variables over historical periods.

Given its centrality to my research, I will provide a more detailed discussion of the ERA5 (Hersbach et al., 2020) and ERA5-Land products (Muñoz-Sabater et al., 2021). The fifth generation of the ECMWF Reanalysis (ERA5), developed by the European Centre for Medium-

Range Weather Forecasts (ECMWF) as part of the Copernicus Climate Change Service, is a prominent reanalysis product (Hersbach et al., 2020). ERA5 assimilates a broad range of satellite and in-situ measurements to develop a numerical model. This methodology generates hourly global datasets with a horizontal resolution of $0.25^{\circ} \times 0.25^{\circ}$ ($\sim 27.75 \text{ km} \times 27.75 \text{ km}$) for the atmosphere and $0.5^{\circ} \times 0.5^{\circ}$ ($\sim 55 \text{ km} \times 55 \text{ km}$) for ocean waves (Hersbach et al., 2020). ERA5 provides a high-resolution record of the global atmosphere, land surface, and ocean waves from 1950 to the present, with data updated in near real-time, offering an invaluable resource for climate and weather analysis (Hersbach et al., 2020). ERA5 exhibits improved agreement with observations in terms of temporal and spatial correlations compared to other reanalysis products, making it a valuable resource for climatological and meteorological studies (Tarek et al., 2020).

ERA5-Land enhances the capabilities of the ERA5 dataset by providing a higher spatial resolution of 0.1° ($\sim 9 \text{ km}$) and focusing on land surface variables, offering up to 53 parameters related to the water and energy cycles (Muñoz-Sabater et al., 2021). This refined dataset is useful in mountainous regions and winter months due to its ability to distinguish between rain and snow, improving the representation of precipitation dynamics (Muñoz-Sabater et al., 2021).

2.4 Gaat Physiology

Gaat, Sockeye Salmon (*Oncorhynchus nerka*), is one of the smaller species of Pacific Salmon, typically measuring ~ 50 to $\sim 80 \text{ cm}$ in length and weighing between ~ 2 to $\sim 7 \text{ kg}$ (Beacham et al., 2004; Fisheries, 2025). A 2009 study of Fraser River (British Columbia) Gaat reported a mean fork length of $\sim 59 \text{ cm}$ and an average weight of $\sim 2.5 \text{ kg}$ for adult fish sampled (Thomas, 2010).

Gaat follow a complex life cycle, requiring physiological adaptations throughout its three to five-year lifespan (Fisheries, 2025; Hruska et al., 2010). Most Gaat populations exhibit a "lake-type"

life history, where the fry emerge from river gravel, migrate to a lake for 1-3 years before becoming smolts and migrating to the Pacific Ocean to grow (Beacham et al., 2004; Fisheries, 2025). After two to five years at sea, they return to freshwater to spawn and die (Beamish et al., 2016; Fisheries, 2025; Quinn, 2005; Ruggerone & Irvine, 2018). This spawning typically occurs over the summer or fall (Beacham et al., 2014; English et al., 2005).

Anatomically, Gaats have a broad head, large eyes, and a terminal mouth lined with sharp teeth (Fisheries, 2025). Gaats have large eyes positioned to the sides of their heads that allow them to spot prey, but are also adapted to see a wide range of light, including ultraviolet. Spawning phase males develop an exaggerated snout as well as a humped back referred to as a kype (Fisheries, 2025; Morton, 1965). At the juvenile stages, Gaats' diet consists primarily of zooplankton and shifts to encompass a variety of organisms after they migrate to the ocean (Farley et al., 2007; Fisheries, 2025). These organisms include squid, decapod larvae, Pacific sandlance (*Ammodytes hexapterus*; Tyler et al., 2001), and micronektonic organisms (Radchenko & Mathisen, 2004). Upon beginning their upriver migration to spawn, Gaats cease feeding (Rand et al., 2006) and rely on endogenous energy stores (Eliason et al., 2011).

Gaats exhibit a striking transformation in coloration during their spawning phase, transitioning from a silvery-blue oceanic appearance to vibrant red bodies and greenish heads (Khrustaleva, 2024). The bodies of male Gaats turn bright red, and their heads take on a greenish hue, enhancing their visibility and appeal to females (Foote et al., 2004). Females also undergo a colour change, becoming redder, though their coloration is typically less intense than that of males (Hanson & Smith, 1967).

The swimming performance of Gaats influences their growth and reproductive success (Burt et

al., 2012; Kocan et al., 2006). Migration over long distances imposes significant energetic demands, requiring Gaat to maintain sustained aerobic activity and exert bursts of anaerobic power to navigate turbulent river currents and natural obstacles (Birnie-Gauvin et al., 2023). Numerous studies have documented the adverse effects of environmental stressors such as rising water temperatures, infectious diseases, and pollutants on swimming ability, which ultimately reduce migration success and increase physiological strain (Burt et al., 2012; Kocan et al., 2006; Wagner et al., 2005).

During their upriver migration, Gaat rely on lipid reserves accumulated during their oceanic phase, which are metabolized to support the sustained effort required for migration (Crossin et al., 2009; Eliason et al., 2011; Magnoni et al., 2006). Migration speed varies considerably among Gaat populations, driven by environmental conditions and population-specific physiological traits (Crossin et al., 2004; Hinch & Bratty, 2000; Quinn, 1988). In the Fraser River, the average swimming speed of migrating Gaat has been estimated at 2.4 km h^{-1} (Quinn, 1988). This supports work showing that the most efficient swimming speeds for mature Gaat are estimated at 1.8 km h^{-1} , with efficient swimming occurring within the range of $1.0\text{--}2.6 \text{ km h}^{-1}$ (Hinch & Bratty, 2000). Factors such as water temperature and river discharge exert a significant influence on energy expenditure during migration, with elevated temperatures accelerating metabolic rates and hastening depletion of energy stores, thus increasing the risk of premature exhaustion (Carey et al., 2019; Groot, 1995; Prystay et al., 2020; Rand et al., 2006). Furthermore, migration conditions such as elevated river discharge conditions further strain these energy reserves, contributing to elevated mortality rates in this critical upriver migration phase (Crossin et al., 2009; Rand et al., 2006).

As ectothermic fish, Gaat's body temperature is in direct thermal equilibrium with the water they inhabit, meaning their metabolic rate is tightly coupled to water temperature (Crossin et al., 2008). This thermal equilibrium directly influences the metabolic and physiological processes of Gaat, including: metabolic rate (Crossin et al., 2008; Young et al., 2006), migration speed (Hanson et al., 2008), and swimming performance (Eliason et al., 2011; Farrell, 2009). The relationship between environmental temperature and metabolic rate in salmon is well-established, with warmer water leading to higher energy demands (Hanson et al., 2008), reduced oxygen uptake (Brett, 1971; Steinhausen et al., 2008) and increased physiological stress (Eliason et al., 2011). Supporting this, Eliason et al. (2011) found that at least 50% of the aerobic scope is needed for the Coastal Weaver Gaat populations to reach their spawning area. These ectothermic characteristics limit Gaat's ability to maintain optimal physiological function when environmental conditions deviate from historical norms (Crossin et al., 2008). In response to rising temperatures, specific populations of Gaat have adjusted their migration timing or sought out cooler water refugia, showing behaviour modification to environmental stressors (Gonia et al., 2006; Mathes et al., 2010). For example, Coastal Weaver Gaat have shifted their migration period up to six weeks earlier from 1995 to 2008 (Eliason et al., 2011). Additionally, modelling has shown that with a projected 2 °C increase in river temperature by 2100, Fraser River Gaat will migrate ~10 days earlier than Gaat in 2010 (Reed et al., 2011). Finally, Gaat in the Columbia River system now initiate their migration 10.3 days earlier than in the 1940s, likely as a direct response to warming water temperatures (Carey et al., 2017; Crozier et al., 2011).

2.5 Effects of Hydrologic Variability on Gaat

Variation in river discharge influences Gaat migration success, timing, and survival to spawning grounds (Henderson et al., 1992; Quinn et al., 1997; Rand et al., 2006). The magnitude and

seasonality of these discharge patterns are affected by hydrometric inputs including changes in snowfall (Déry et al., 2016; Kang et al., 2014), rainfall (Milliman et al., 2008; Modarres & Ouarda, 2013), air temperature (Blöschl, 1991), and anthropogenic disturbances (Bathurst et al., 2017; Graf, 2006; Huang et al., 2015). Moreover, as discussed in Section 2.1, meteorological phenomena including ARs can further amplify runoff, increasing it by up to 12.5 times (Zhou et al., 2025).

Building on this, watershed characteristics further modulate how hydrometric inputs affect river discharge. In boreal forests, the seasonal freeze-thaw cycle increases runoff and infiltration when soils are frozen, while also limiting groundwater recharge (Shanley & Chalmers, 1999). Meanwhile, the structure and composition of forest stands influence soil infiltration capacity, with mature forest cover enhancing water retention and reducing surface runoff (Rahmat et al., 2018). However, differences in forest age, soil type, and vegetation characteristics affect the extent to which watersheds can absorb and store water (Rahmat et al., 2018). Clearcutting in Finland's boreal forests led to elevated runoff rates, gradually returning to baseline levels as forest cover regenerated (Ide et al., 2013). Climate change further complicates watershed-scale hydrology, with warmer temperatures leading to increased snow accumulation and earlier snowmelt, increasing spring discharge in high-latitude areas (Adam et al., 2009; Fallot et al., 1997).

The timing, frequency, magnitude, and duration of discharge events (Poff et al., 1997) shape a range of fluvial habitat characteristics. These include channel morphology (Hauer et al., 2011; Mosley, 1982), sediment transport (Lenzi et al., 2006; Turcotte et al., 2011), flow refugia (Mathers et al., 2022; Sueyoshi et al., 2014), thermal refugia (Mathers et al., 2022), bank erosion

(Hooke, 1979), extensive woody debris recruitment (Comiti et al., 2016), water quality (Mattikalli et al., 1996), hydrologic connectivity (Grantham, 2013), and the thermal regime (Dickson et al., 2012; White et al., 2017). In the Tagliamento River, a large gravel-bed system draining the Italian Alps, floods approaching 200% of bankfull discharge mobilise the entire braid-belt, entirely reworking high bars and islands (Surian et al., 2009). These elevated discharge levels drive bank retreats up to 6 m, forcing channel realignment and redistribution of coarse bed material (Surian et al., 2009). Additionally, maintaining hydrologic connectivity requires minimum discharge thresholds that vary for each section of a river. Grantham (2013) found that flow requirements for sustaining connectivity varied among different sections of Sausal Creek, a tributary of California's Russian River Basin.

Variation in river discharge influences the bioenergetic feasibility of Gaat migration and subsequent spawning success (Hinch & Rand, 1998; Rand et al., 2006). Elevated Fraser River discharges in 1997 ($7500 \text{ m}^3 \text{ s}^{-1}$, ~50 % above the 1956 low-flow benchmark) led to simulated energy depletion in Gaat 1000 km upstream (Rand et al., 2006). In 2001, under lower discharge levels ($5400 \text{ m}^3 \text{ s}^{-1}$), Gaat reached the spawning grounds with energy reserves within normal ranges (Hinch & Rand, 1998). Yet it is prolonged sub-bankfull flows that most acutely constrain migrations. In British Columbia's Koeve River, mature Gaat avoided freshwater during periods of low water, delaying until rainfall restored river discharge (Atlas et al., 2021). Similarly, low discharge contributed to the near-complete failure of the Snake River Gaat run in 2015 (Crozier et al., 2020).

Within the same watershed, the Taku River Tlingit Fisheries Department has observed that both high and low discharge on the Gaat Héeni River can obstruct migration, documenting cases of

fish holding downstream during extreme flood and drought events (TRTFN Fisheries Department, 2022).

2.6 Effects of Changing Water Temperature

Water temperature influences the migration of Gaat by affecting metabolic rates (Atlas et al., 2021; Islam et al., 2019), aerobic scope (Eliason et al., 2011), stress responses (Mathes et al., 2010), and behavioural decisions (Jeffries et al., 2012; Martins et al., 2012). Field and modelling studies have demonstrated thresholds and dose-response relationships between temperature and migration success in natural watersheds (Atlas et al., 2021; Eliason et al., 2011).

River discharge influences water temperature, with high discharge buffering rivers against heating by adding volume and accelerating downstream transport. Low river discharge can result in shallow, slow-moving water that warms rapidly. In the Koeve River, discharge levels below $4 \text{ m}^3 \text{ s}^{-1}$ elevated water temperatures by 2–3 °C, resulting in the mortality of half the Gaat population (Atlas et al., 2021). Modelling in the Fraser River showed a 20 % summer-flow decline yields ~ 0.9 °C warming and doubles days > 20 °C (Islam et al., 2019). Thus, elevated summer discharge tempers peak water temperatures, while drought-level lows intensify thermal stress on migrating Gaat.

Across decadal time frames, persistent elevation of water temperature in the Fraser River has intensified metabolic stress on migrating Gaat (Islam et al., 2019). Sustained exposure of Gaat to water temperature ≥ 19 °C has been causally linked to prolonged en route holding, delayed arrival at spawning grounds, and heightened pre-spawn mortality (Jeffries et al., 2012; Martins et al., 2012).

Telemetry and escapement records for the Columbia–Snake River corridor reveal contrasts in successful Gaat migration. During the hot, low discharge summer of 2015, only 8–12 % of adult Snake River Gaat reached their headwater spawning grounds after passing Bonneville Dam, compared with the typical 60–80 % survival (Crozier et al., 2020). River temperatures held at 22–23 °C for prolonged periods, forming a thermal barrier that halted migrations and triggered mass stranding and disease outbreaks (Crozier et al., 2020).

Behavioural studies confirm that Gaat actively avoid elevated water temperatures by seeking thermal refugia. Telemetry studies of early-run Gaat in the Harrison River reveal a marked thermal constraint on migration success. When river temperatures reached highs of 21.5 °C, 16% of tagged Gaat reached their natal grounds. In contrast, when entry temperatures remained below 18 °C, 72% of migrating Gaat completed the journey without resorting to thermal refuge (Mathes et al., 2010).

Emerging evidence suggests Gaat are adapting to changes in water temperature (Armstrong et al., 2016; Eliason et al., 2011; Reed et al., 2011). In the Fraser River, Gaat populations traversing long, high-energy corridors possess greater aerobic scope and higher thermal optima than coastal Gaat from shorter, cooler routes (Eliason et al., 2011). Fraser River field studies likewise show that warm migration years favour individuals with superior cardiorespiratory performance, strengthening selection for these traits (Armstrong et al., 2016). In contrast, eco-evolutionary simulations for Columbia River Gaat (Snake River stock) project that the first upstream entry could advance by ~10 days under a +2 °C scenario, cutting quasi-extinction risk by 83 % relative to non-evolving populations (Reed et al., 2011).

Chapter 3: DATA

Chapter 3 presents the datasets used in this thesis. For additional details on the region's physiography, refer to Section 1.3 and Figure 1.1. The datasets introduced below include: reanalysis datasets (Section 3.1), meteorological data (Section 3.2), hydrological data (Section 3.3), the SIO-R1 Atmospheric River Catalog (Section 3.4), and escapement data from Gaat Áayi (Section 3.5).

3.1 Reanalysis Data

ERA5-Land (Muñoz-Sabater et al., 2021) data were extracted over the Gaat Héeni Watershed domain (55°N–58.5°N, 132°W–134°W) to assess long-term meteorological variability. The dataset, with a 0.1° (~9 km) spatial resolution, was extracted at an hourly timescale for 1991–2024 and aggregated to daily values for comparison with in-situ meteorological and hydrometric records.

The extracted variables were air temperature (°C), snow depth (cm), SWE (mm), total precipitation (mm), geopotential ($\text{m}^2 \text{s}^{-2}$), and snowfall (m of water equivalent). These variables were used to analyze seasonal and interannual variability in precipitation phase partitioning, snow accumulation, and temperature trends.

3.2 Meteorological Data

Meteorological data were obtained from four stations in and around the Gaat Héeni Watershed to characterize temperature, precipitation, snow depth, and SWE. These stations, listed in Table 3.1, include: Llewellyn Glacier, Atlin (ECCC Station 1200560), Gaat Héeni, and the Atlin Lake Snow Survey site (Government of British Columbia Station 4E02B), each providing hourly meteorological observations.

The Llewellyn Glacier Station (2013–2024) records total rainfall (mm), whereas the Atlin Station (1981–2021; ECCC Station 1200560) provides a long-term record of air temperature ($^{\circ}\text{C}$), snow depth (cm), and total rainfall (mm). The Gaat Héeni Station, installed in 2024 (Section 4.1), records total precipitation (mm), wind speed (km h^{-1}), air temperature ($^{\circ}\text{C}$), relative humidity (%) and atmospheric pressure (hPa). The Atlin Lake Snow Survey Station (2004–2024; Government of British Columbia Station 4E02B) provides SWE (mm) and snow depth (cm) measurements.

Table 3.1: Meteorological station metadata (Environment and Climate Change Canada, 2024; Government of British Columbia, 2024).

Station	Climate ID	Variables	Latitude ($^{\circ}\text{N}$), Longitude ($^{\circ}\text{W}$)	Elevation (m)	Period of Record
Llewellyn Glacier	N/A	Rainfall (mm)	59.1054, 134.0379	890	2013-2024
Atlin	1200560	Snow Depth (cm)	59.5780, 133.6895	696	1981-2021
		Air Temperature ($^{\circ}\text{C}$)			
		Total Precipitation (mm)			
		Snowfall (cm)			
		Rainfall (mm)			
<u>Gaat Héeni</u>	N/A	Total Precipitation (mm)	59.1538, 133.0428	533	2024
		Wind Speed (km h^{-1})			
		Air Temperature ($^{\circ}\text{C}$)			
		Relative Humidity (%)			
		Atmospheric Pressure (hPa)			
Atlin Lake	4E02B	SWE (mm)	59.5886, 133.7102	730	2004-2024
		Snow Depth (cm)			

3.3 Hydrologic Data

Hydrologic data from two stations in the Gaat Héeni Watershed monitor water temperature, river discharge, and river level (Table 3.2). Each station records data at an hourly resolution, allowing for detailed analysis of hydrological variability. The Lower Gaat Héeni Station records hourly water temperature ($^{\circ}\text{C}$) from 2021 to 2024 whereas the Gaat Héeni Station, installed in 2024, measures hourly river discharge ($\text{m}^3 \text{s}^{-1}$), level (m), and velocity (m s^{-1}).

Table 3.2: Hydrologic station metadata (C. Sergeant, personal communication, 15 January 2024).

Station	Variables	Latitude ($^{\circ}\text{N}$), Longitude ($^{\circ}\text{W}$)	Elevation (m)	Period of Record
Lower <u>Gaat Héeni</u>	Water Temperature ($^{\circ}\text{C}$)	59.1152, 133.0025	315	2021-2024
<u>Gaat Héeni</u>	Discharge ($\text{m}^3 \text{s}^{-1}$)	59.1538, 133.0428	533	2024
	Level (m)			
	Velocity (m s^{-1})			

3.4 SIO-R1 Atmospheric River Catalog

Although multiple AR identification tools exist at both global and regional scales (Gershunov et al., 2017; Guan & Waliser, 2019; Vallejo-Bernal et al., 2023), this thesis uses the Scripps Institution of Oceanography's (SIO)-R1 AR Catalog (Gershunov et al., 2017; <http://cw3e.ucsd.edu/Publications/SIO-R1-Catalog/>, accessed 5 March 2025) to characterize AR activity and IVT. The SIO-R1 catalog was constructed using 6-hourly specific humidity and wind data at a $2.5^{\circ} \times 2.5^{\circ}$ spatial resolution, derived from the NCEP–NCAR (National Centers for Environmental Prediction–National Center for Atmospheric Research) reanalysis dataset (Kalnay et al., 1996). AR events are identified using an IVT threshold $\geq 250 \text{ kg m}^{-1} \text{ s}^{-1}$, ensuring a consistent framework for detecting moisture transport events. The catalog provides information on AR frequency, duration, and landfall locations, with data covering the North American West Coast (20°N to 60°N) from January 1948 to December 2024. Validation by Gershunov et al.

(2017) against Neiman et al. (2008) employed Special Sensor Microwave Imager (SSM/I) observations and demonstrated strong agreement between the datasets, reinforcing its reliability for AR analysis.

For this study, I focus on 1991 to 2024, aligning with extracted ERA5-Land data (Section 3.1) to facilitate a robust assessment of AR-driven hydroclimatic impacts. AR landfall locations were extracted from 55°N to 60°N, aligning with the study region.

3.5 Escapement Data

Escapement data for Gaat are monitored at a weir located downstream of Gaat Áayi, managed by TRTFN. TRTFN Fisheries (2024) collects and shares these data with the Department of Fisheries and Oceans Canada. Escapement counts are obtained through a weir structure, with the sole passage point continuously monitored by both a motion capture camera system and field technicians. Data from 1980-1981 and 1992-2024 have been collected, with observations occurring annually between July and September (Figure 1.2). For 2024, Fisheries and Oceans Canada provided daily arrival counts of Gaat at Gaat Áayi.

Chapter 4: METHODS

This section outlines the methodologies that will be used to investigate hydroclimatic variability, reanalysis data validation, AR climatology, and passage dynamics. A meteorological station (Section 4.1) has collected meteorological and hydrological measurements, including air temperature, atmospheric pressure, wind speed, total precipitation, relative humidity, discharge, river level, and river velocity. ERA5-Land reanalysis data will be extracted and validated against in-situ observations (Section 4.2) using bias, root mean square error (RMSE), and the coefficient of determination (R^2). The climatology of the Gaat Héeni Watershed will be characterized (Section 4.3) by analyzing long-term trends in air temperature, precipitation, and snowpack conditions. AR climatology will be examined using the SIO-R1 AR Catalog (Section 4.4), applying spatial and temporal classification criteria to identify and track AR landfall events. The impact of ARs on watershed scale hydroclimatic conditions will be assessed (Section 4.5) by quantifying AR contributions to total precipitation and evaluating seasonal and interannual variability. Section 4.6 outlines the methods used to quantify the timing and sensitivity of daily discharge responses to precipitation events in the Gaat Héeni Watershed during the 2024 monitoring period. The analysis applies event-based classification of AR and non-AR precipitation, constructs dual-axis hydrographs, and calculates precipitation centroid lags to peak discharge to characterize event-scale hydrological responses. Finally, video monitoring and a logistic regression with a logit function will assess how discharge and water temperature influence Gaat passage success through SR3-3 (Section 4.7). Section 4.8 outlines the methods used to quantify the influence of daily jump success at SR3-3 on Gaat arrival anomalies at Gaat Áayi using linear regression models at lag intervals of one, two, and three days.

4.1 Installation of Meteorological Station

An initial review of meteorological and hydrometric stations within and adjacent to the Gaat Héeni Watershed revealed a lack of verifiable data. To address this gap, the first phase of this research involved installing a hydrometric station on the Gaat Héeni (Figure 4.1). Located on the west bank of the Gaat Héeni River at 533 m above sea level, this station records air temperature ($^{\circ}\text{C}$), atmospheric pressure (hPa), wind speed (m s^{-1}), total precipitation (mm), relative humidity (%), discharge ($\text{m}^3 \text{s}^{-1}$), river level (m), and river velocity (m s^{-1}). Instrumentation is anchored on a 3 m stainless-steel tripod, which supports the R.M. Young Wind Monitor 05103 (wind speed and direction) and a Meter Group ATMOS-14 sensor (air temperature, relative humidity, and atmospheric pressure). Data are recorded by an XLINK500-IR-1 datalogger with integrated Iridium telemetry, powered by a 50 W solar panel and a 120 Ah AGM battery in a weatherproof enclosure. A separate scaffold, erected 4 m from the tripod, supports the OTT Pluvio² total precipitation gauge to ensure unobstructed catchment and minimal flow disturbance. A non-contact radar flow-meter system (Sommer RQ-30a) is deployed on an adjacent structure to measure river discharge continuously. All sensors log data at 15-minute intervals and transmit hourly to the Hydromet Cloud network. Data collection began on 17 June 2024 and continues to the present, with discharge measurements suspended for the winter starting on 15 October 2024.



Figure 4.1: This year-round meteorological station, photographed on 9 October 2024, monitors meteorological and hydrological conditions in the Gaat Héeni Watershed. It records total precipitation (mm), wind speed (m s^{-1}), air temperature ($^{\circ}\text{C}$), relative humidity (%), and atmospheric pressure (hPa), with data collected by an OTT Pluvio², RM Young wind monitor, and ATMOS-14 sensor. A 50-watt solar panel supplies power, and an XLINK500 datalogger with Iridium telemetry transmits data remotely. A nearby OTT RQ-30a radar sensor provides measurements of river discharge ($\text{m}^3 \text{s}^{-1}$), level (m), and velocity (m s^{-1}).

4.2 Extraction and Validation of Reanalysis Data

Reanalysis data for the Gaat Héeni Watershed and adjacent regions (Figure 1.1) were extracted from the ERA5-Land reanalysis product (Muñoz-Sabater et al., 2021) for the period 1991-2023.

The extracted variables were air temperature at 2 m (K), snow depth (cm), snow depth water equivalent (m of water equivalent), total precipitation (mm), geopotential ($\text{m}^2 \text{s}^{-2}$), and snowfall (m of water equivalent). ERA5-Land data, available on a 0.1° (octahedral) reduced Gaussian grid with hourly resolution (Copernicus Climate Change Service, 2019), were extracted for grid cells encompassing in-situ validation sites and aggregated to a daily timescale. To ensure consistency, in-situ observations were converted from Pacific Standard Time (PST) to Universal Coordinated Time (UTC) prior to validation (Clelland et al., 2024).

Daily ERA5-Land values for air temperature, snow depth, and snow depth water equivalent were calculated by averaging the extracted hourly values over each 24-hour period.

Air temperature at 2 m (in degrees Kelvin [K]) was converted to degrees Celsius (°C) by applying the linear relation (Hall et al., 2024; Preston-Thomas, 1990) shown in Equation 1:

$$T_{\text{°C}} = T_K - 273.15 \quad (1)$$

Daily total precipitation and snowfall values were computed using Equation 2, where tp represents total precipitation in millimeters and d is the day of interest (Copernicus Climate Change Service, 2019). The value of tp at $d+1$ 00 UTC accounted for the total precipitation accumulated during the preceding 24-hour period.

$$tp [mm] = tp_{d+1 \text{ 00UTC}} [m] \times 1000 \quad (2)$$

Snow depth water equivalent (SWE) in ERA5-Land is expressed in meters of water equivalent and represents the depth of water that would result across the grid cell if the entire snowpack melted (Kouki et al., 2023; Muñoz-Sabater et al., 2021). To convert SWE to from meters (m) millimeters (mm), the SWE values are multiplied by 1000.

ERA5-Land performance was assessed at two meteorological stations: Atlin (ECCC Station 1200560) and Atlin Lake (Government of British Columbia Station 4E02B). A date-matched dataset was created to ensure a robust comparison by aligning daily in-situ observations with daily aggregated ERA5-Land outputs. Accuracy was quantified using bias (mean difference), root mean square error (RMSE), coefficient of determination (R^2), and the p-value to assess statistical significance.

Surface elevation for each ERA5-Land grid cell was derived from the geopotential ($\text{m}^2 \text{s}^{-2}$), which represents gravitational potential energy per unit mass (Gershunov et al., 2017).

Geopotential elevation (m) was obtained by dividing geopotential by standard gravitational acceleration ($g = 9.80665 \text{ m s}^{-2}$; Copernicus Climate Change Service, 2019).

To account for elevation differences between ERA5-Land grid cells and in-situ meteorological stations during air temperature validation, a standard lapse rate correction of $-6.5 \text{ }^\circ\text{C km}^{-1}$ was applied (Kattel & Yao, 2018; Li et al., 2015). This correction adjusts ERA5-Land air temperature outputs to better reflect in-situ elevations by compensating for the typical decrease in air temperature with altitude.

The elevation difference, $\Delta Elev$ (m), was calculated as the in-situ elevation minus the ERA5-Land grid cell elevation. For example, at Atlin (ECCC station 1200560), the station elevation was 697 m, while the ERA5-Land elevation was 673.6 m, resulting in a $\Delta Elev$ of 23.4 m. The unadjusted ERA5-Land air temperature is T_{ERA5} ($^\circ\text{C}$), and the resulting elevation-adjusted air temperature is T_{adj} ($^\circ\text{C}$). The lapse rate-adjusted air temperature was calculated as:

$$T_{adj} = T_{ERA5} + \left(\frac{-6.5}{1000}\right) \times \Delta Elev \quad (3)$$

SWE and snow depth were validated at a daily temporal scale using in-situ data from Atlin Lake (Government of British Columbia Station 4E02B) collected between 2004 and 2023. To improve agreement between ERA5-Land outputs and observed values, bias correction was applied following the approach outlined by Chen et al. (2013).

Bias was calculated as the difference between the ERA5-Land values and the corresponding in-situ observations (Equation 4a). This metric quantifies the over- or underestimation in the

ERA5-Land dataset. The number of paired observations is denoted by N , *ERA5Land* refers to the modelled values, and *InSitu* refers to the observed values. *Bias* was calculated as:

$$Bias = \frac{1}{N} \sum (ERA5Land - InSitu) \quad (4a)$$

The bias-corrected value, *BiasCorr*, was then derived by subtracting the *Bias* calculated in 4a from each *ERA5-Land* value. The bias-corrected ERA5-Land value was calculated as:

$$BiasCorr = ERA5Land - Bias \quad (4b)$$

Time series plots were used to analyze seasonality and long-term variability in snow depth (cm) and SWE (mm).

ERA5-Land precipitation and snowfall data were validated against in-situ measurements from the Atlin (ECCC Station 1200560) meteorological station at daily and monthly timescales.

Scatter plots incorporating a 1:1 line were used to visualize the relationship between modelled and observed values.

4.3 Climatology of the Gaat Héeni Watershed

The ERA5-Land data validated in Section 4.2 were used to characterize the climatology of the Gaat Héeni Watershed. ERA5-Land reanalysis data, including daily temperature, snowfall, SWE, total precipitation, snow depth, and geopotential, were extracted for 1991–2023. Data were spatially averaged across all ERA5-Land grid cells whose centroids intersected the Gaat Héeni Watershed boundary to produce a representative climatological overview. Spatially averaged data were computed across grid cells at the native hourly resolution (UTC scale) before any temporal aggregation. For air temperature, an elevation correction was applied (Equation 2) to

account for the difference between the mean elevation of the ERA5-Land extracted grid cells (915 m) and the Gaat Héeni Watershed's mean elevation (955 m).

Monthly air temperature data were visualized using a box and whisker plot, while SWE and snow depth were visualized through time series plots to assess interannual variability. Rainfall was derived by calculating the difference between total precipitation and snowfall (Espinoza et al., 2018).

Total precipitation and snowfall extracted from ERA5-Land were visualized using a stacked bar chart to illustrate the annual distribution of rainfall and snowfall. Rainfall was derived by subtracting snowfall from total precipitation (Jeoung et al., 2022; Li et al., 2025). Monthly distributions of total precipitation, snowfall, and rainfall were also represented using box and whisker plots to highlight seasonal patterns, interquartile ranges (IQRs), and outliers.

Annual and monthly precipitation trends were analyzed to assess long-term variability in moisture input and phase partitioning between rain and snow. Total precipitation and snowfall were plotted as a stacked bar chart to illustrate the annual distribution of rainfall and snowfall. Monthly distributions of total precipitation, snowfall, and rainfall were visualized using box and whisker plots to illustrate seasonal patterns, IQRs, and outliers.

4.4 Atmospheric River Climatology

Section 4.4 investigates the spatial distribution, frequency, and intensity of ARs making landfall between 55°N and 60°N from 1 January 1991 to 31 December 2023. This period corresponds to meteorological and hydrometric data availability, as outlined in Sections 3.3 and 3.4. The SIO-R1 AR Catalog (Gershunov et al., 2017) was adapted for daily resolution to identify and

classify AR landfall events. The methodological framework follows the approach outlined by Gershunov et al. (2019), incorporating a set of specific criteria. Each daily time step was analyzed for spatial patterns of contiguous grid cells with $IVT \geq 250 \text{ kg m}^{-1} \text{ s}^{-1}$ to identify ARs. Only events extending at least 1500 km in length and intersecting the coastline were classified as ARs. The coastal grid cell exhibiting the maximum IVT was designated as the landfalling location for each event. To maintain temporal continuity, the landfalling location of a single AR event could not shift more than 1000 km ($\sim 8.9^\circ$ latitude) between consecutive days. Additionally, two ARs making landfall in the same general coastal region were classified as distinct events if separated by at least 24 hours. The SIO-R1 AR catalog was used to analyze seasonal variability, interannual trends, and changes in AR intensity across the study period.

To assess the seasonal distribution of ARs, I calculated the monthly frequency of AR landfall events and the associated mean net IVT for each month from 1991 to 2023. The net IVT for each month was determined by summing the IVT values of all AR landfall events occurring within that month across the 33 years, providing a cumulative measure of moisture transport associated with ARs. Monthly statistical distributions, including mean, median, IQR, and total range, were computed, with outliers defined as values exceeding 1.5 times the IQR (Gautam & Singh, 2022). To further explore potential decadal-scale shifts in AR activity, the study period was divided into three sub-periods (1991–2001, 2002–2012, and 2013–2023), with each sub-period analyzed separately using the same statistical metrics applied to the full dataset.

4.5 Impact of ARs on the Study Region

Building on the methodology outlined in Sections 4.3 and 4.4, Section 4.5 quantifies AR contributions to seasonal and annual precipitation in the Gaat Héeni Watershed. The analysis

covers January 1991 to December 2023, aligning with the SIO-R1 AR Catalog and the ERA5-Land reanalysis dataset extracted in Section 4.2 (Gershunov et al., 2017; Sharma & Déry, 2020).

Following the methodology outlined in Section 4.4, ARs are defined as contiguous grid cells with an IVT $\geq 250 \text{ kg m}^{-1} \text{ s}^{-1}$, extending at least 1500 km and intersecting the coastline between 55°N and 60°N (Gershunov et al., 2017). To quantify the portion of precipitation attributed to ARs, I identify the initial AR landfalling day and the following day (Gershunov et al., 2017). This accounts for the lag time as ARs move inland from the coast (Sobral & Déry, 2023) and mitigates some uncertainty related to UTC-to-local time differences in precipitation datasets (Sharma & Déry, 2020).

I integrate AR landfalling events from the SIO-R1 AR Catalog with ERA5-Land precipitation, snowfall data, and the derived rainfall calculated in Section 4.3. To ensure spatiotemporal consistency, ERA5-Land data are averaged across the Gaat Héeni Watershed (Sharma and Déry, 2020) with precipitation classified as AR-driven when the IVT criterion is met (Equation 5). The fraction of precipitation attributed to ARs (F_{AR}) is then calculated as the ratio of total precipitation during AR landfall days (P_{AR} , mm) to the total seasonal precipitation (P_{Total} , mm).

$$F_{AR} = \frac{P_{AR}}{P_{Total}} \quad (5)$$

The seasonal variability of AR-driven precipitation is calculated by computing the fraction of total precipitation attributed to ARs for each season, revealing seasonal dependencies in AR contributions. Seasons are delineated as spring (March–May), summer (June–August), fall (September–November), and winter (December–February) (Sobral & Déry, 2023). To evaluate long-term variability, the study period is stratified into three sub-periods (1991–2001, 2002–

2012, and 2013–2023), ensuring consistency with the AR climatology trend analysis outlined in Section 4.2.

I constructed a stacked bar chart spanning the 33-year study period (1991–2023) to visualize interannual variability in AR-driven and non-AR-driven precipitation. This plot quantifies annual precipitation totals attributable to AR events (blue bars) and non-AR precipitation (grey bars).

I also calculated decadal means for 1991–2001, 2002–2012, 2013–2023, and the whole 1991–2023 period to contextualize longer-term patterns.

Furthermore, a Mann-Kendall (MK) test (Kendall, 1948; Mann, 1945) is employed at both annual and seasonal scales to detect monotonic trends in AR-driven precipitation, with statistical significance assessed at the 95% confidence level. A significance threshold of 0.05 indicates that results with p-values of 0.05 or below are deemed statistically significant (Ravi & Odorico, 2005). This approach enables the identification of potential shifts in AR frequency and their contribution to total precipitation over time.

4.6 Discharge Sensitivity to Daily Precipitation and AR Events

Section 4.6 describes the methodology used to examine how daily discharge and precipitation in the Gaat Héeni Watershed are influenced by AR events, with a specific focus on event-scale hydrological responses. The objective is to determine the timing and sensitivity of discharge to AR-driven precipitation during the 2024 monitoring season.

Identification of AR events followed the IVT threshold approach outlined in Section 4.4, using landfall data from the updated SIO-R1 AR Catalog (Gershunov et al., 2017). Events were classified as ARs when $IVT \geq 250 \text{ kg m}^{-1} \text{ s}^{-1}$ along a contiguous corridor of at least 1500 km in

length. The AR also had to land on the North American west coast between 55°N and 60°N to be included in the analysis. Following the approach in Section 4.5, precipitation was attributed to AR activity if it occurred on the AR landfall day or the following day.

Daily precipitation and discharge data were aggregated from hourly data collected at the Gaat Héeni meteorological and hydrometric stations (Sections 3.2 and 3.3). Daily data were used to align with the daily resolution of the SIO-R1 AR catalog. Each day in the dataset from 17 June to 10 October 2024 was classified as either AR-driven or non-AR-driven, enabling the partitioning of precipitation by source. To summarize precipitation distribution, grouped bar charts were used to compare cumulative AR and non-AR contributions, consistent with the seasonal AR precipitation quantification methods described in Section 4.5. These classifications were used to construct a dual-axis hydrograph (Mathai & Mujumdar, 2022), in which daily discharge is overlaid with AR-driven and non-AR-driven precipitation.

Defining the hydrological response in the Gaat Héeni Watershed involved quantifying the lag between the precipitation centroid and peak discharge based on daily precipitation and discharge records. Precipitation events comprised one or more consecutive days with ≥ 1 mm of precipitation, separated by at least one precipitation-free day (Li et al., 2023). For each identified event, the precipitation centroid time (t_{WC}) was computed to represent the effective timing of water input into the system. The precipitation centroid time (t_{WC}) is the weighted mean timing of precipitation during an event, representing when the majority of the event's precipitation occurred. Precipitation centroid time was calculated using Equation 6, where P_i is the precipitation (mm) recorded during the i th hour, t_i is the timestamp (in days), and n is the total number of daily observations within the precipitation event (Dingman, 2015).

$$t_{wc} = \frac{\sum_{i=1}^n P_i \times t_i}{\sum_{i=1}^n P_i} \quad (6)$$

To evaluate the hydrologic response of the Gaat Héeni Watershed to each precipitation event, the time of peak discharge, t_{pk} , was identified as the timing of the maximum observed streamflow following the precipitation event. The timing of the precipitation input was characterized using the precipitation centroid time (t_{wc}). The lag between the precipitation centroid and the resulting discharge peak, referred to as the centroid lag to peak discharge (t_{LPS}), measures the watershed's response time. This lag, expressed in days, is expressed in Equation 7:

$$t_{LPS} = t_{PK} - t_{WC} \quad (7)$$

4.7 Quantifying Optimal Hydrological Conditions for Successful Gaat Barrier Passage

Section 4.7 discusses how water temperature (T , °C) and river discharge (Q , m³ s⁻¹) influence Gaat jump success at obstruction SR3-3. The methodological workflow is summarized in Figure 4.2.

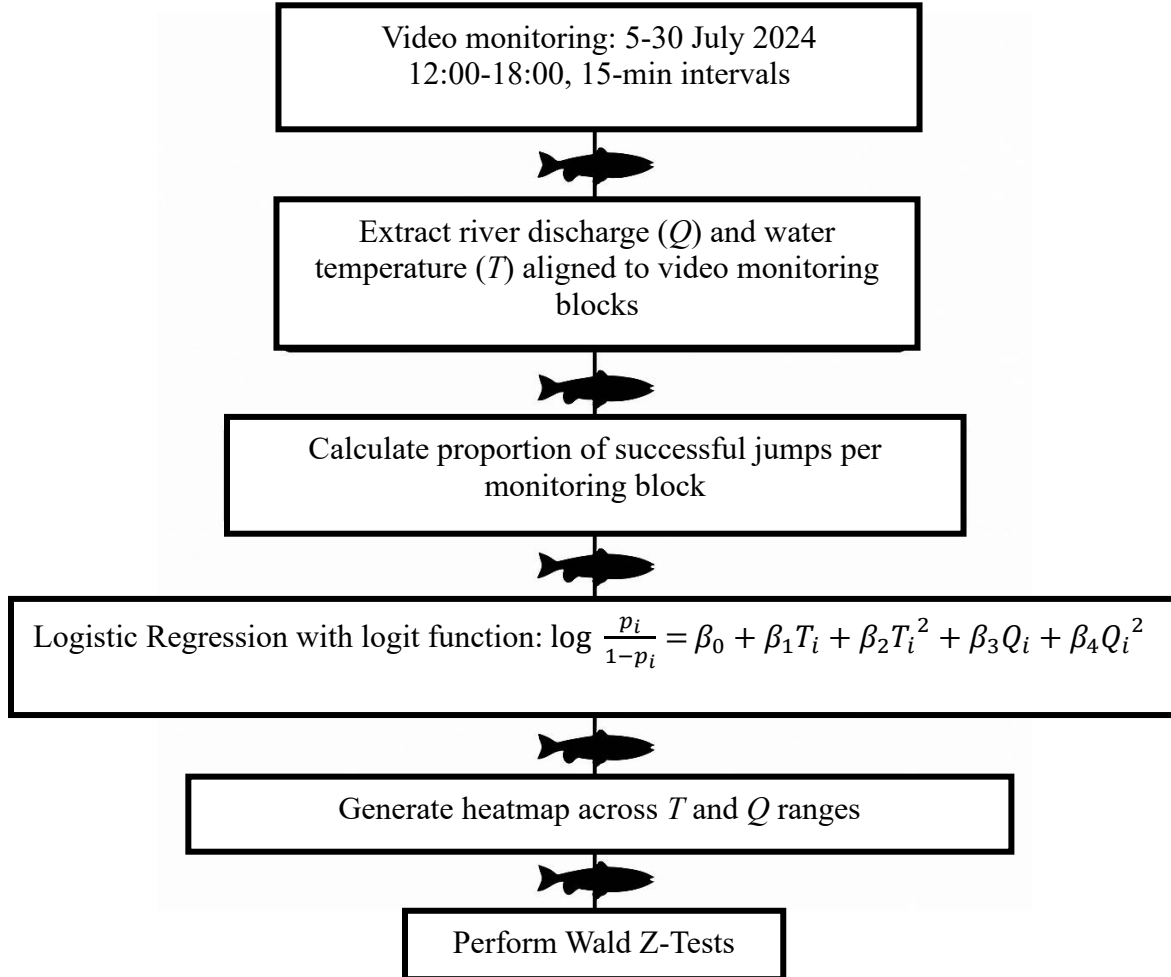


Figure 4.2: A flowchart outlining methods shown to determine optimal hydrologic conditions for the successful jump of Gaat at SR3-3.

Previous assessments by the Taku River Tlingit Fisheries Department (2017) had identified SR3-3 as a key migratory barrier (Section 1.4; Figure 4.3). Video monitoring of SR3-3 was conducted from 5 to 30 July 2024, with observations carried out from 1200-1800 local time (UTC-7) on each monitoring day. During the first 15 minutes of every hour, a Nikon Zf full-frame camera fitted with a Tamron 150-500 mm f/5-6.7 zoom lens captured 4 K UHD

(3840×2160 px) footage at 60 fps from a fixed tripod. Focal length was adjusted to 200 mm to frame the wetted jump face. Although daily filming was planned, field constraints limited data collection to 110 15-minute observation blocks distributed over 19 monitoring days (six blocks on each of 17 days and two blocks on 23 July). During this period, a total of 92,687 jump attempts was recorded. No footage was obtained on 15 July, 18 July, or 24-27 July owing to crew fatigue and hazardous river conditions. Each jump attempt recorded on video was scored as a binary outcome: 1 for a successful jump or 0 for a failure. A successful jump was defined as Gaat landing with forward momentum (Lauritzen et al., 2005) in a laminar flow region (Mueller et al., 2008).

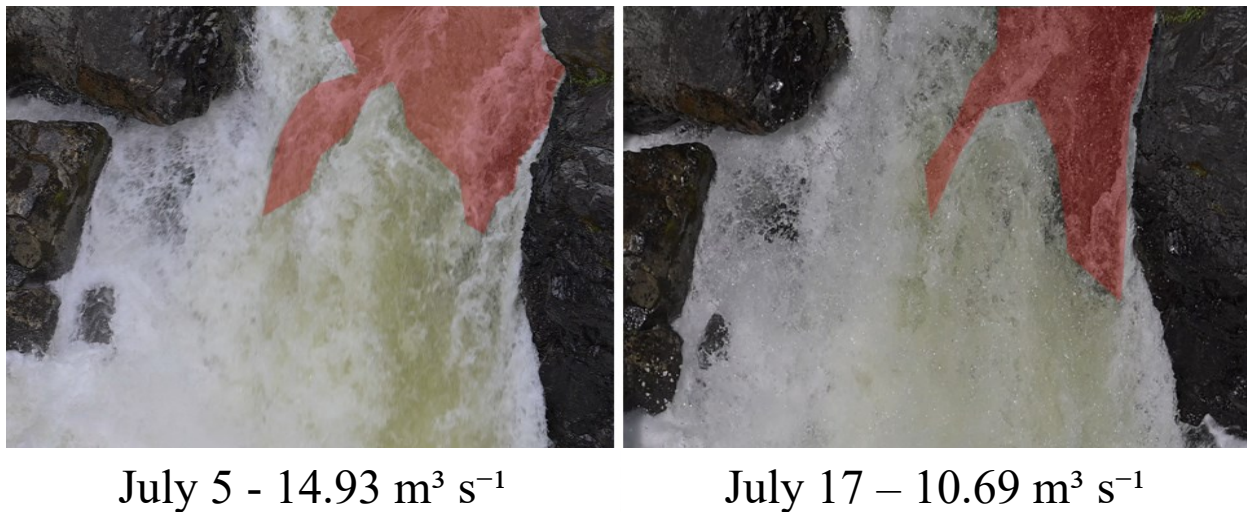


Figure 4.3: Photographs on 5 and 17 July 2024 comparing discharge conditions at SR3-3, a canyon constriction that is a migration barrier for Gaat (Sockeye Salmon; *Oncorhynchus nerka*). Discharge at 1200 hours on 5 July 2024 was $14.93 \text{ m}^3 \text{ s}^{-1}$, while discharge decreased to $10.69 \text{ m}^3 \text{ s}^{-1}$ by 1500 hours on 17 July 2024. Red polygons in each image delineate areas of laminar surface flow.

To analyze water temperature and discharge trends, I extracted averaged hourly discharge (Q , $\text{m}^3 \text{ s}^{-1}$) data from the Gaat Héeni hydrometric station and utilized hourly water temperature (T , $^{\circ}\text{C}$) data from the lower Gaat Héeni (C. Sergeant, personal communication, 2024). Data were extracted between 5 and 30 July 2024 to align with the video monitoring periods. A composite figure was produced in which the daily jump-attempt count is shown as a vertical bar chart, and

the daily mean river discharge ($\text{m}^3 \text{s}^{-1}$) and daily mean water temperature ($^{\circ}\text{C}$) are each overlaid as a point joined by a continuous line. Hourly discharge and water temperature measurements recorded during each day's observation window were first averaged to yield a single mean value per day.

To assess how hydrologic conditions affected Gaat jump success, a logistic-regression model (Dockery et al., 2017) with a logit link was fitted to the jump data. The logit link function transforms the probability of a binary outcome into log-odds, allowing for a linear relationship between predictors and the transformed response, while constraining predicted probabilities to values between 0 and 1 (Hosmer et al., 2013; Peng et al., 2002). In this model, p represents the probability of a successful jump (Hosmer et al., 2013). The probability of jump success was modelled as a function of water temperature (T , $^{\circ}\text{C}$) and river discharge (Q , $\text{m}^3 \text{s}^{-1}$), including both linear and quadratic terms for each predictor (Maynard et al., 2017). Quadratic terms were retained because passage success typically peaks at intermediate flows and water temperatures and declines at extremes (Cruz-Jesus et al., 2017; Haro & Castro-Santos, 2012). To mitigate observer bias and pseudo-replication arising from repeated jump attempts within 15-minute monitoring blocks (Bolker et al., 2009; Harrison et al., 2018), all jump attempts recorded in each 15-minute monitoring interval were aggregated into a single binomial observation (Lazic et al., 2020). Each aggregated data point thus represents the proportion of successful jumps (S_i) relative to total jump attempts (N_i) observed in that interval, explicitly defining the probability (p_i) used in the logistic regression model (Equation 8);

$$p_i = \frac{S_i}{N_i} \quad (8)$$

Equation 9 is a logistic regression with a logit function and incorporates four hydrologic

predictors: water temperature (T , °C), river discharge (Q , m³ s⁻¹), and their respective quadratic terms (T^2 and Q^2). In this formula, the logit of the jump-success probability is expressed as a linear combination of five regression coefficients: the intercept β_0 , which provides the baseline log-odds of success when all predictors equal zero, the linear terms β_1 (water temperature) and β_3 (discharge), which quantify first-order effects, and the quadratic terms β_2 (water temperature curvature) and β_4 (discharge curvature).

$$\log \frac{p_i}{1-p_i} = \beta_0 + \beta_1(T_i) + \beta_2(T_i^2) + \beta_3(Q_i) + \beta_4(Q_i^2) \quad (9)$$

To visualize the model's behaviour over the range of observed temperature (T) and discharge (Q) conditions, I generated a two-dimensional prediction grid using the `ggplot2` package in R (R Core Team, 2024; Wickham, 2016). Water temperature (T , °C) and river discharge (Q , m³ s⁻¹) were separated into 250 equally spaced values spanning their empirical minima and maxima. For each node on this grid, the linear (T , Q) and quadratic (T^2 , Q^2) predictors described in Equation 8 were computed. These values were combined with the predicted probabilities (p_i) to predict jump success. The resulting heatmap illustrates the relationship between environmental variables and jump success probability and utilises a uniform and colourblind friendly palette.

In R (R Core Team, 2024), the maximum and minimum predicted probabilities on the prediction grid were identified using `which.max()` and `which.min()`, extracting the corresponding water temperature and discharge values (Bolker et al., 2009; Harrison et al., 2018). The 110 fitted block-level probabilities were then summarized with the `summary()` function to obtain the minimum, first quartile, median, mean, third quartile, and maximum.

Wald z-tests were used to evaluate the statistical significance of each coefficient β_j in the model

(McArdle, 1988). The Wald z-test is defined in equation 10 where β_j is the maximum likelihood estimate of the coefficient and $SE(\beta_j)$ is its standard error (Hosmer et al., 2013). Predictors with p-values > 0.05 are considered nonsignificant within this analysis.

$$z_j = \frac{\beta_j}{SE(\beta_j)} \quad (10)$$

4.8 Influence of Jump Success on Gaat Arrival at Gaat Áayi

This section aims to determine how the daily jump success at SR3-3 influences the arrival of Gaat at Gaat Áayi. Daily jump success (p_d) was calculated by aggregating total successful jumps and jump attempts from all 15-minute observation intervals recorded each monitoring day (Equation 11). S_{di} represents successful jumps in block i on day d , N_{di} indicates total jump attempts in block i on day d .

$$p_d = \sum(S_{di}) / \sum(N_{di}) \quad (11)$$

To isolate daily variations in the arrival of Gaat at Gaat Áayi, daily arrival anomalies (ΔA) at the Gaat Áayi weir were computed as daily arrival counts (A_d) minus the mean daily arrival count (A) recorded over the observation period (Equation 12):

$$\Delta A = A_d - A \quad (12)$$

A linear regression model was fitted, which tested relationships between observed daily jump success (p_d) and arrival anomalies ΔA at lag intervals (n) of one, two, and three days (Equation 13). Equation 14 was derived by algebraically rearranging the original linear regression (Equation 13) to isolate the regression coefficient (β). Due to the absence of empirical migration time data, it was assumed that Gaat would take one, two, or three days (n) to swim 22.5 km from SR3-3 to Gaat Áayi. This assumption aligns with previously discussed Gaat migration speeds (Hinch & Bratty, 2000; Quinn, 1988), but introduces inherent uncertainty, as actual swim speeds

may vary considerably due to hydrological conditions or individual fish physiology. The error term (ε) accounts for residual variation that the model does not explain.

$$\Delta A_n = \beta \times p_d + \varepsilon \quad (13)$$

$$\beta = \frac{\Delta A_n}{p_d} + \frac{\varepsilon}{p_d} \quad (14)$$

R^2 and statistical significance (p-values) of the regression coefficient β were examined at lag intervals of one, two, and three days to determine the lag at which jump success most strongly and significantly predicted upstream arrival anomalies.

Chapter 5: RESULTS

The results presented in this chapter synthesize the meteorological, hydrological, and climatic factors shaping the Gaat Héeni Watershed from 1991 to 2023. Particular emphasis is placed on precipitation, air temperature, river discharge, and ARs. Section 5.1 initiates the analysis by presenting data collected from the meteorological station located in the upper Gaat Héeni Watershed during the period of 17 June to 10 October 2024. Section 5.2 validates ERA5-Land reanalysis data through comparison with in-situ measurements, providing a foundation for subsequent analyses. Building upon this, Section 5.3 explores the climatological characteristics of the region, elucidating long-term trends and seasonal variations. Section 5.4 delves into the patterns and dynamics of ARs, highlighting their frequency, intensity, and seasonal distribution in the Gaat Héeni Watershed. In Section 5.5, the influence of ARs on key meteorological variables is quantified, revealing their significant role in modulating regional precipitation. Section 5.6 analyzes daily precipitation and discharge during the 2024 monitoring period to quantify the short-term hydrological response of the Gaat Héeni Watershed to AR and non-AR events. Section 5.7 applies the aforementioned findings to assess the optimal hydrometric conditions for Gaat, identifying key thresholds and environmental factors influencing migration success. Finally, Section 5.8 quantifies the relationship between daily jump success at SR3-3 and daily arrival anomalies at Gaat Áayi, determining the lag intervals at which jump success most significantly predicts arrival variability.

5.1 Meteorological Data

To illustrate the short-term dynamics of meteorological and hydrological conditions in the Gaat Héeni Watershed, Figure 5.1 presents hourly observations recorded at the Gaat Héeni station from 18 June to 10 October 2024. It shows temporal variations across meteorological and

hydrological parameters including air temperature ($^{\circ}\text{C}$), atmospheric pressure (hPa), wind speed (m s^{-1}), total precipitation (mm), relative humidity (%), discharge ($\text{m}^3 \text{s}^{-1}$), river level (m) and river velocity (m s^{-1}). Recorded air temperatures ranged from -5.6°C to 27.4°C , with atmospheric pressure values between 912.4 hPa and 945.3 hPa.

Hydrological variability was evident in both precipitation and discharge data. A pronounced precipitation event occurred between 22 and 24 July 2024, during which 47 mm of rainfall was recorded. This precipitation event resulted in a rapid hydrological response, with river discharge increasing from $8.7 \text{ m}^3 \text{s}^{-1}$ to $30.0 \text{ m}^3 \text{s}^{-1}$ over the same period and river level and velocity showing similar increases.

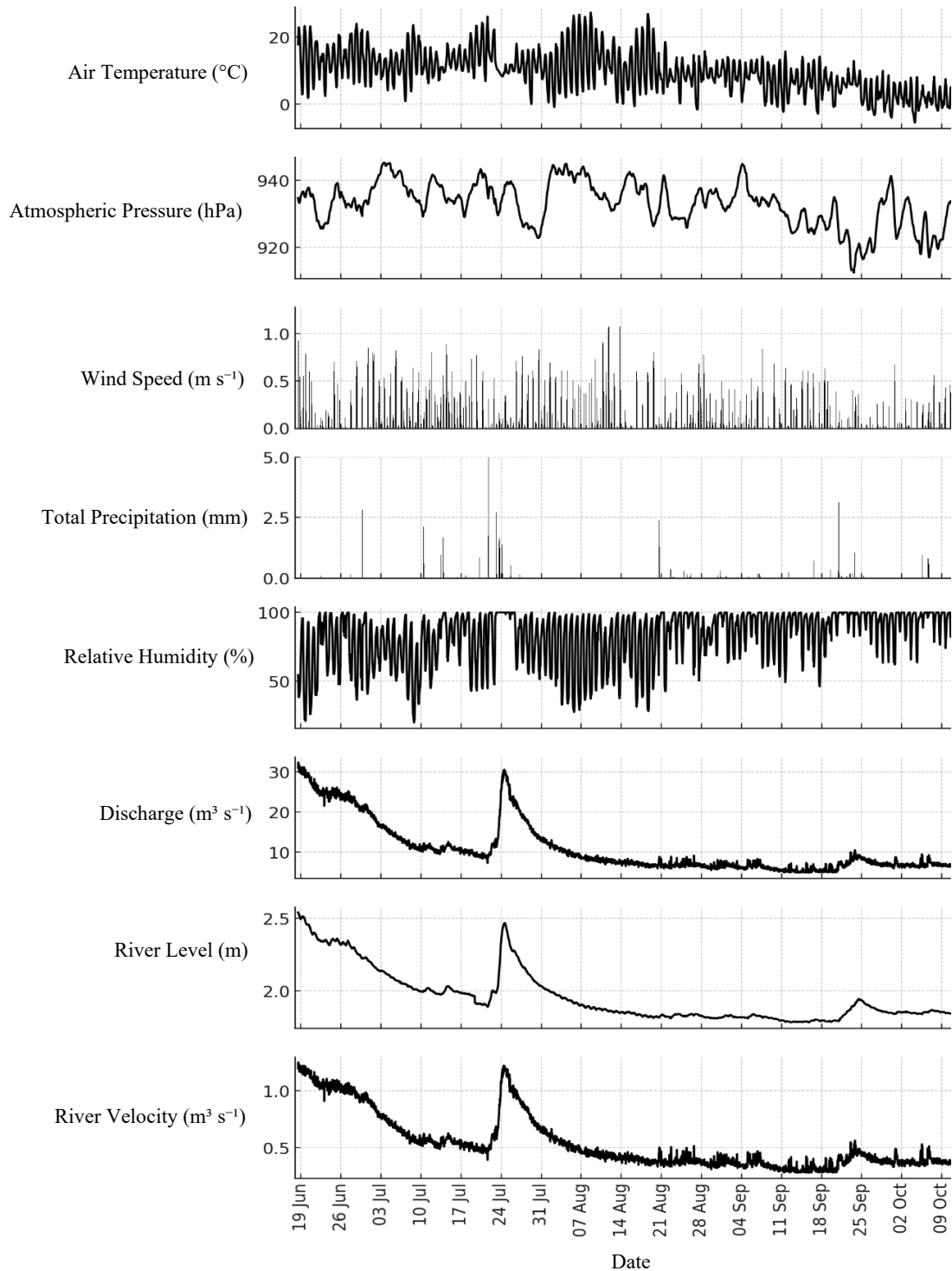


Figure 5.1: Hourly meteorological and hydrometric data from the Gaat Héeni Station, collected between 18 June and 10 October 2024, provide a detailed record of summer hydroclimatic conditions. The figure presents air temperature ($^{\circ}\text{C}$), atmospheric pressure (hPa), wind speed (m s^{-1}), total precipitation (mm), relative humidity (%), discharge ($\text{m}^3 \text{s}^{-1}$), river level (m) and river velocity (m s^{-1}).

5.2 Extraction and Validation of Reanalysis Data

The validation of ERA5-Land reanalysis data for air temperature, SWE, and snow depth was conducted using in-situ data from Atlin (1991-2021; ECCC Station 1200560) and Atlin Lake (2004-2023; Government of British Columbia Station 4E02B).

At Atlin (1991-2021; ECCC Station 1200560), daily ERA5-Land air temperature exhibits a bias of $-2.1\text{ }^{\circ}\text{C}$ relative to observed values, with a root mean square error (RMSE) of $3.5\text{ }^{\circ}\text{C}$, an R^2 of 0.9, and a p-value of 0.039 (Figure 5.2). After adjusting for elevation at the same daily scale, the bias is reduced to $-1.9\text{ }^{\circ}\text{C}$, RMSE improves to $3.4\text{ }^{\circ}\text{C}$, and the R^2 remains at 0.9, with a p-value of 0.035.

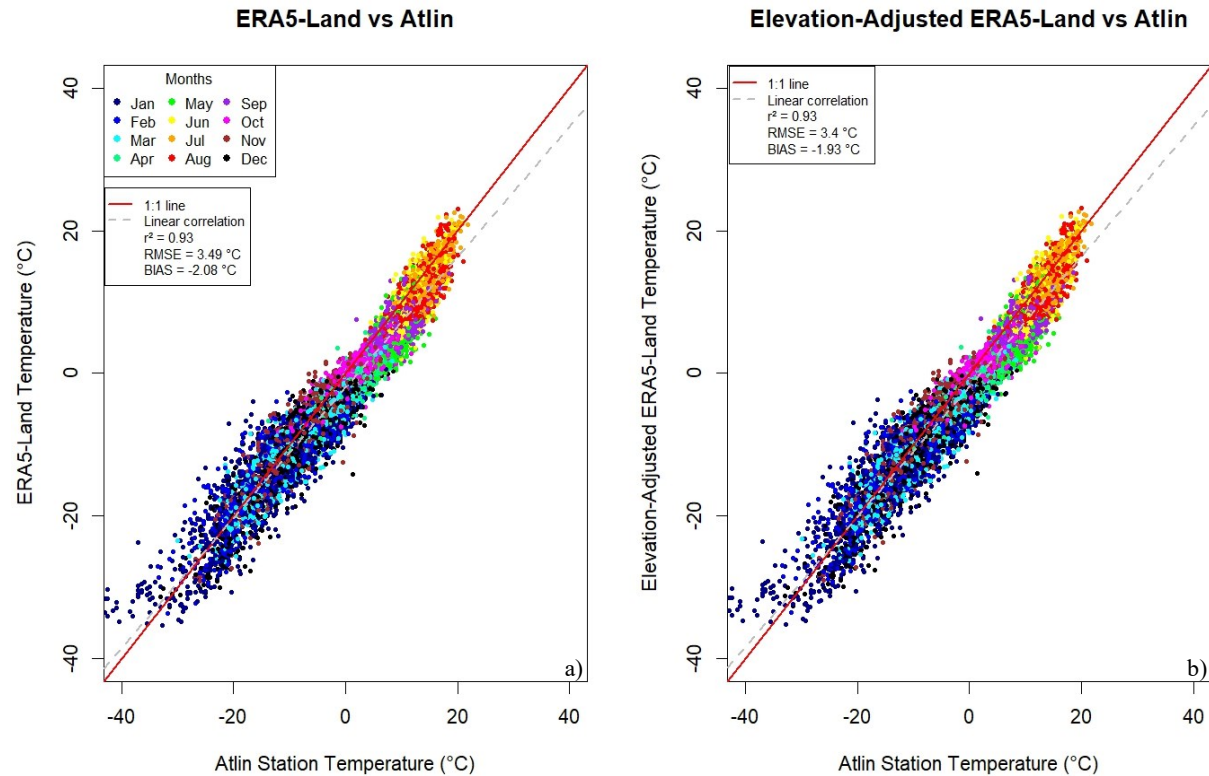


Figure 5.2: Hourly ERA5-Land reanalysis air temperatures are compared with air temperatures from the Atlin station (ECCC Station 1200560) from 1991–2001. Panel a) shows unadjusted ERA5-Land values, while panel b) displays air temperatures corrected for elevation using a standard lapse rate of $-6.5\text{ }^{\circ}\text{C km}^{-1}$. Elevation correction reduced the mean bias from $-2.1\text{ }^{\circ}\text{C}$ to $-1.9\text{ }^{\circ}\text{C}$ and decreased the RMSE from $3.5\text{ }^{\circ}\text{C}$ to $3.4\text{ }^{\circ}\text{C}$. In both cases, the strength of the linear relationship remained high ($R^2 = 0.9$) with a p-value of 0.035.

The validation of SWE extracted from ERA5-Land highlights underestimation in the ERA5-Land dataset (Figure 5.3). At Atlin Lake (2004-2023; Government of British Columbia Station 4E02B), ERA5-Land has a bias of 283.1 mm, RMSE of 290.9 mm, and an R^2 of 0.33 with a p-value of 0.52. After bias correction (Equations 3a and 3b), the bias diminishes to 0.0 mm, and RMSE improves to 67.0 mm. R^2 remains at 0.331 with a p-value of 0.52.

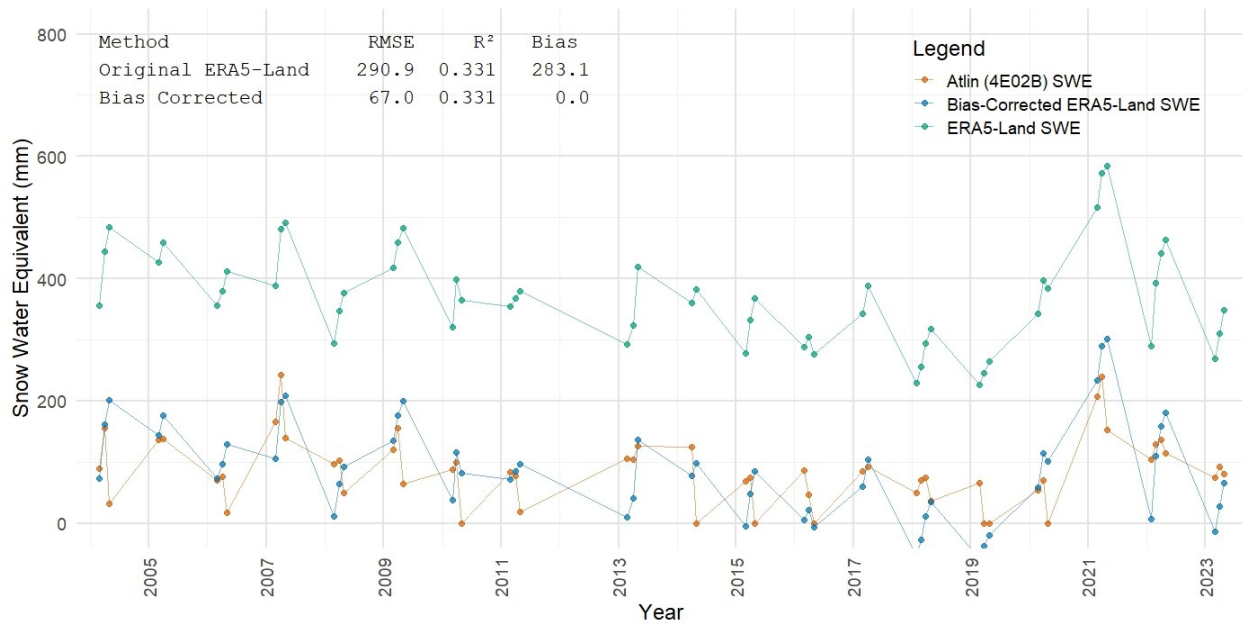


Figure 5.3: Comparison of the observed SWE measurements from the Atlin Lake Snow Survey Station (Government of British Columbia Station 4E02B) with ERA5-Land reanalysis data for the exact dates. Three datasets are shown: observed SWE (orange), original ERA5-Land SWE (green), and bias-corrected ERA5-Land SWE (blue). The original ERA5-Land product substantially overestimated SWE, with a mean bias of 283.1 mm and a root mean square error (RMSE) of 290.9 mm. Following bias correction, the mean bias was eliminated and the RMSE was reduced to 67.0 mm, while the coefficient of determination ($R^2 = 0.33$) remained unchanged.

The snow depth data from ERA5-Land demonstrate a consistent overestimation at Atlin Lake (2004-2023; Government of British Columbia Station 4E02B), as illustrated in Figure 5.4.

Initially, the ERA5-Land dataset shows a bias of 82.5 cm, an RMSE of 83.6 cm, and an R^2 of 0.70 with a p-value of 0.34. After applying bias correction (Equations 3a and 3b), the bias is reduced to 0.0 cm, and the RMSE improves to 13.5 cm. The R^2 remains unchanged at 0.70, with

a p-value of 0.34.

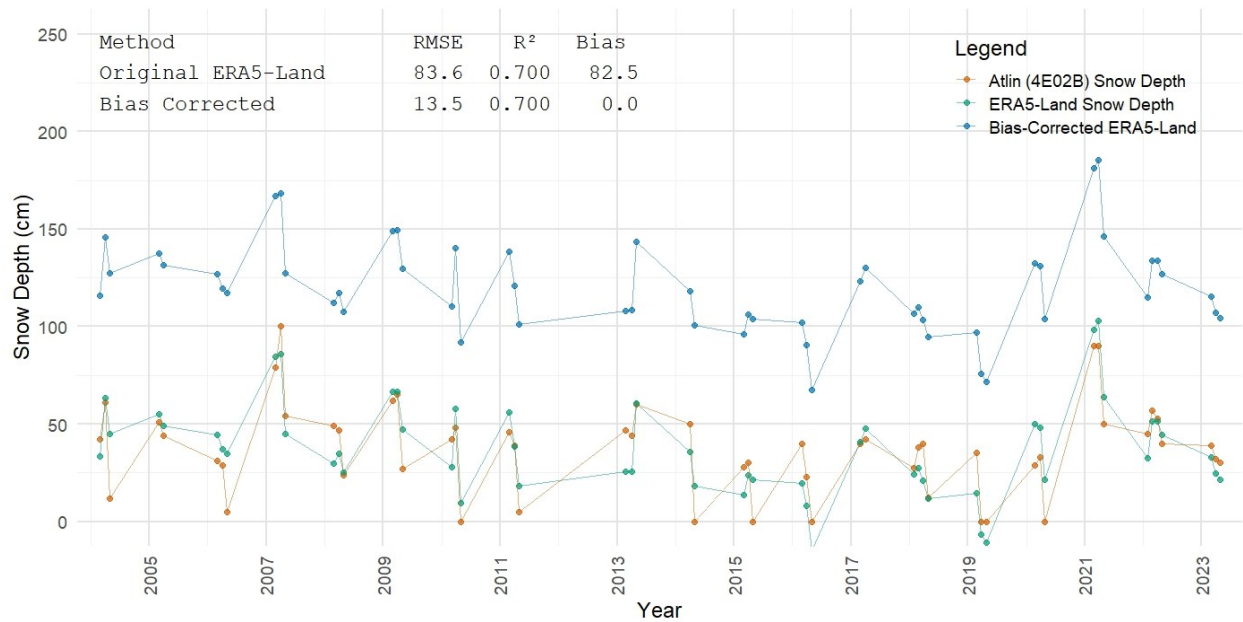


Figure 5.4: Comparison of ERA5-Land reanalysis snow depth with manually collected in-situ observations from the Atlin Lake Snow Survey Station (Government of British Columbia Station 4E02B) from 2004–2023. Before bias correction, ERA5-Land exhibits a mean bias of 82.5 cm and a root mean square error (RMSE) of 83.6 cm. The coefficient of determination (R^2) was 0.70, with a p-value of 0.34, reflecting moderate agreement. After applying bias correction, the mean bias became 0 and RMSE improved significantly to 13.5 cm, while R^2 remained unchanged.

Figure 5.5 compares daily precipitation from Atlin (1991–2021; ECCC Station 1200560) and ERA5-Land. The analysis shows a poor correlation: R^2 of 0.002, p-value of 0.92, and an RMSE of 4.58 mm. This relationship suggests that ERA5-Land poorly captures daily precipitation at Atlin, consistent with previous work (Goswami et al., 2024; Wu et al., 2023).

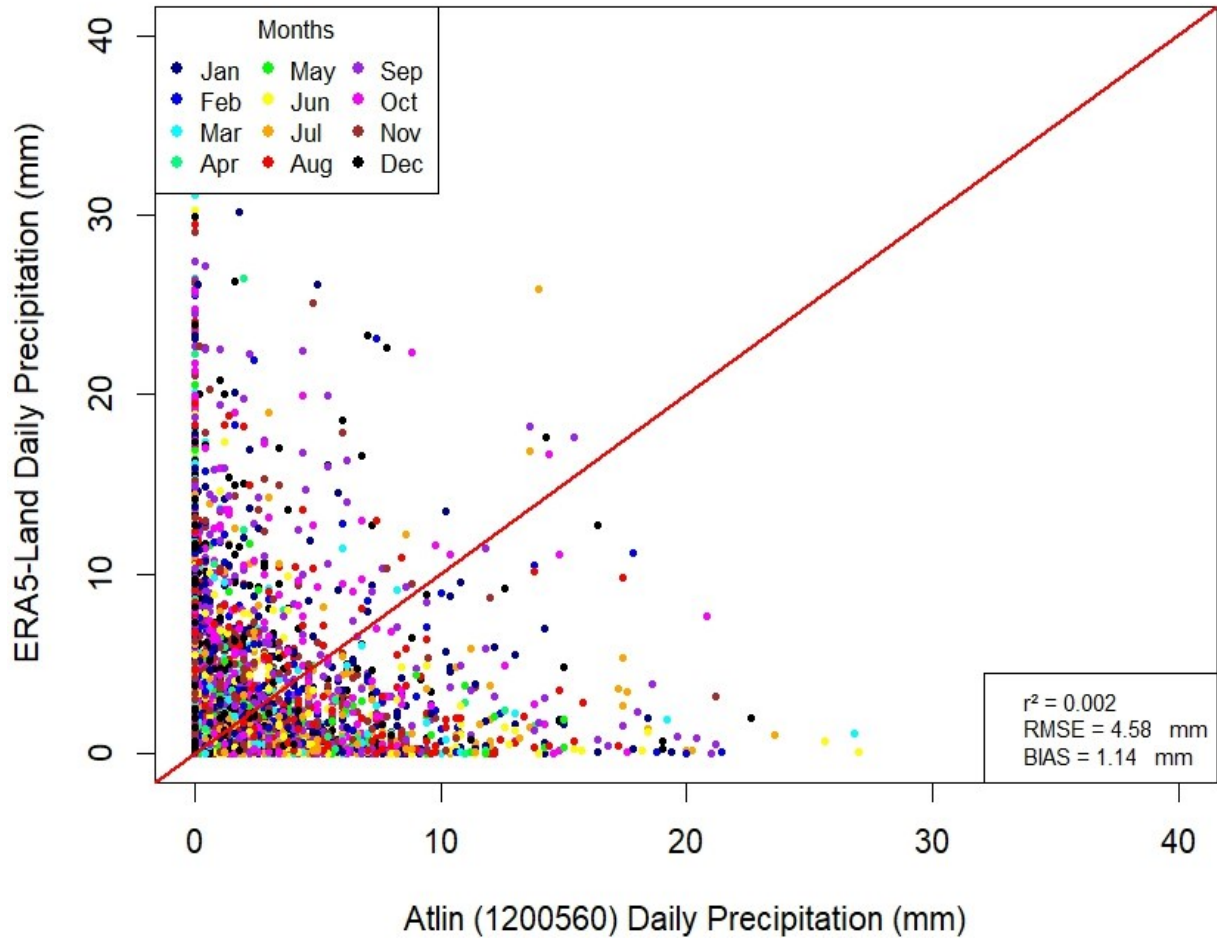


Figure 5.5: Total daily precipitation from ERA5-Land reanalysis and in-situ measurements at the Atlin meteorological station (ECCC Station 1200560) from 1991–2020. ERA5-Land data were extracted for the grid cell overlapping the station and temporally aligned with the in-situ observations. ERA5-Land demonstrates limited skill in capturing daily precipitation variability, with a weak correlation ($R^2 = 0.002$, $p = 0.92$), a root mean square error (RMSE) of 4.58 mm, and a mean bias of 1.14 mm.

Despite the poor agreement at a daily scale, at a monthly scale, Atlin (1991-2021; ECCC Station 1200560) and ERA5-Land at a monthly scale (Figure 5.6) show a moderate correlation with an R^2 of 0.42 and a p-value of 0.04. This suggests that while ERA5-Land does not capture daily precipitation, it represents long-term variability when daily errors are aggregated over time (Wu et al., 2023).

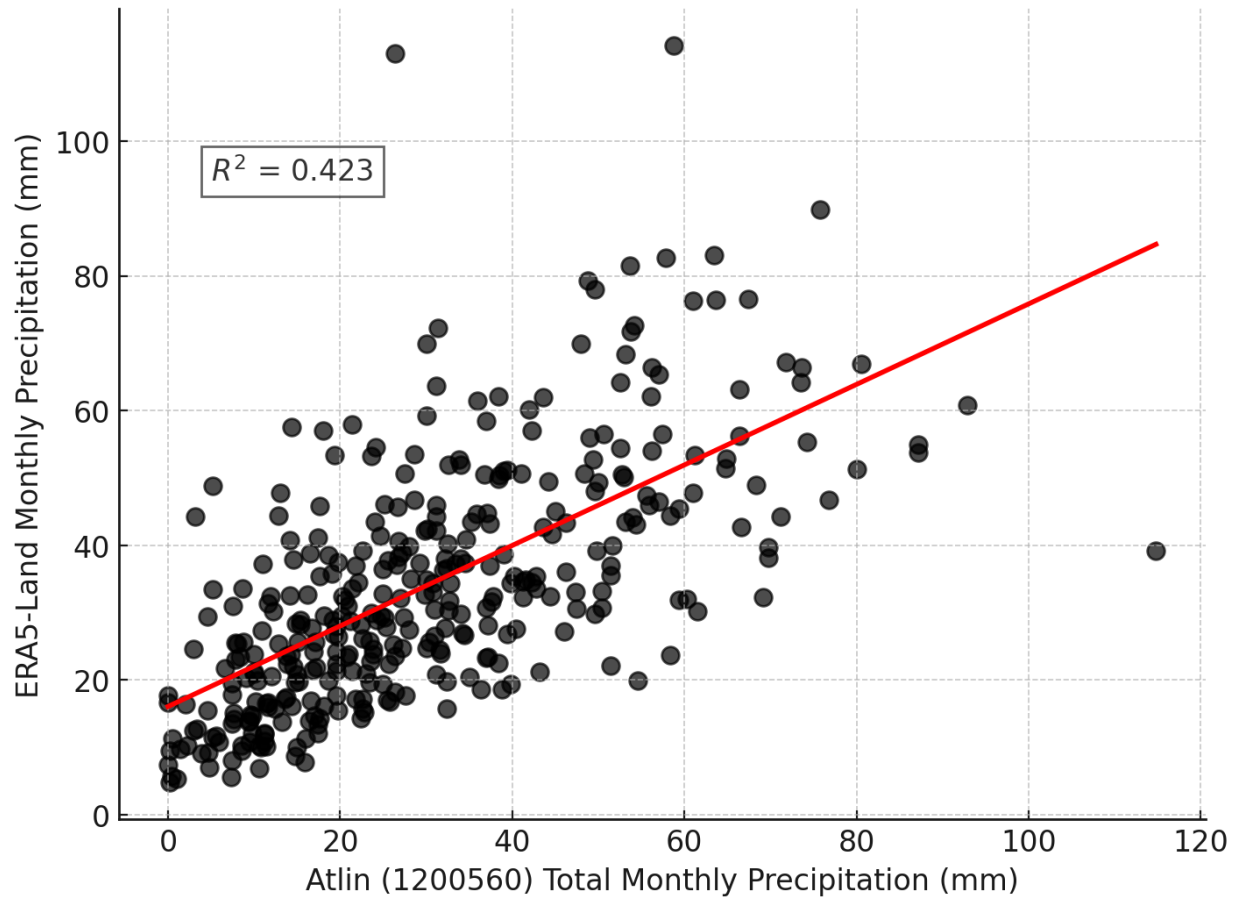


Figure 5.6: Comparison of total monthly precipitation from ERA5-Land reanalysis with monthly aggregated in-situ observations at the Atlin meteorological station (ECCC Station 1200560) for 1991–2020. ERA5-Land data were spatially and temporally aligned with station records. Monthly aggregation improves agreement compared to the daily scale, with a stronger correlation ($R^2 = 0.42$, $p < 0.05$), a reduced RMSE of 22.3 mm, and a mean bias of 9.7 mm. These results indicate that ERA5-Land is more reliable for capturing precipitation variability at coarser temporal resolutions.

5.3 Climatology of the Study Region

Section 5.3 analyzes the climatological conditions in the Gaat Héeni Watershed from 1991 to 2023. During this period, the mean annual air temperature averaged -2.3 °C, with the coldest year (1993) reaching -3.5 °C and the mildest year (2022) reaching -1.2 °C. Total mean annual precipitation was 481.9 mm, varying from a minimum of 335.9 mm in 1995 to a maximum of 606.1 mm in 2004. The mean annual rainfall was 165.3 mm, with yearly totals ranging from 93.2 mm in 1992 to 235.6 mm in 2017.

For air temperature (°C), an elevation correction was applied using Equation 2 to account for the

40 m elevation difference between the extracted ERA5-Land grid cells (915 m) and the Gaat Héeni Watershed mean elevation (955 m). This resulted in a 0.26 °C decrease in the extracted ERA5-Land air temperature. The temperature cycle in the Gaat Héeni Watershed follows a seasonal pattern (Figure 5.7) with cold winters, rapid spring warming, warm summers, and a cooling autumn transition. Looking at monthly air temperature distributions, winter (December–February) remains the coldest period, with January recording the lowest mean temperature (-14.8 °C), reaching a minimum of -26.8 °C. February remains cold (-12.1 °C avg.), with lows of -21.7 °C, while March (-8.5 °C avg.) signals the beginning of seasonal warming. Spring (April–May) sees a sharp increase in temperatures, with April averaging -1.9 °C and May transitioning to positive temperatures (3.3 °C avg.), reaching highs of 7.4 °C. Summer (June–August) reaches peak warmth, with July recording the highest mean temperature (10.9 °C) and maximum highs of 14.3 °C.

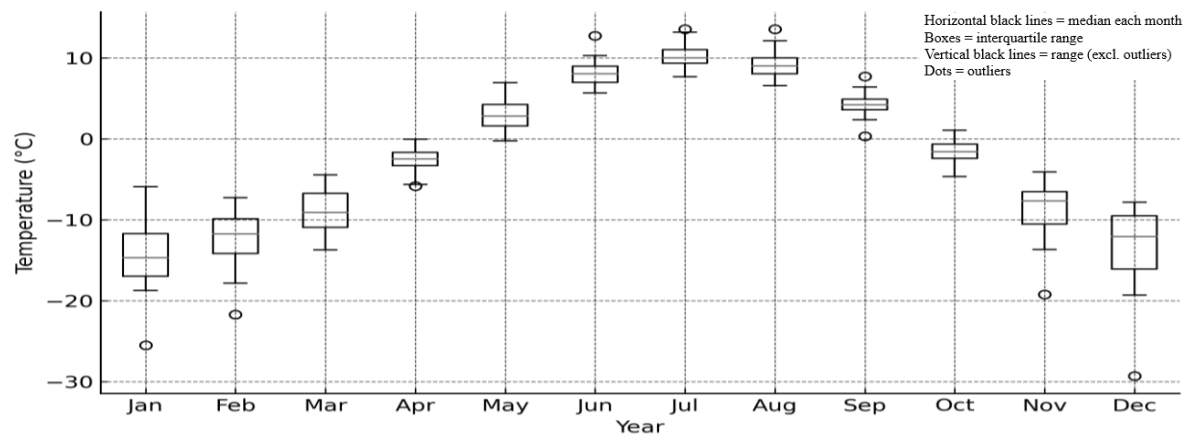


Figure 5.7: Distribution of monthly air temperatures extracted from ERA5-Land in the Gaat Héeni Watershed (1991 to 2023). Box and whisker plots capture each month's interquartile range, minimum/maximum values, median, and outliers, highlighting the seasonal variability and spread of daily air temperatures.

The seasonal SWE (mm) and snow depth (cm) extracted from ERA5-Land (Figures 5.8 and 5.9) is characterized by a consistent cycle of accumulation and ablation. Peak SWE occurs in February to March, with an annual mean of 416.0 mm and observed annual peaks ranging from

300.7 mm to 606.1 mm. Similarly, the mean annual snow depth is 175.3 cm with a maximum snow depth of 260.2 cm in 2005 and a minimum snow depth of 100.1 cm in 1995. Complete ablation typically occurs by May– June.

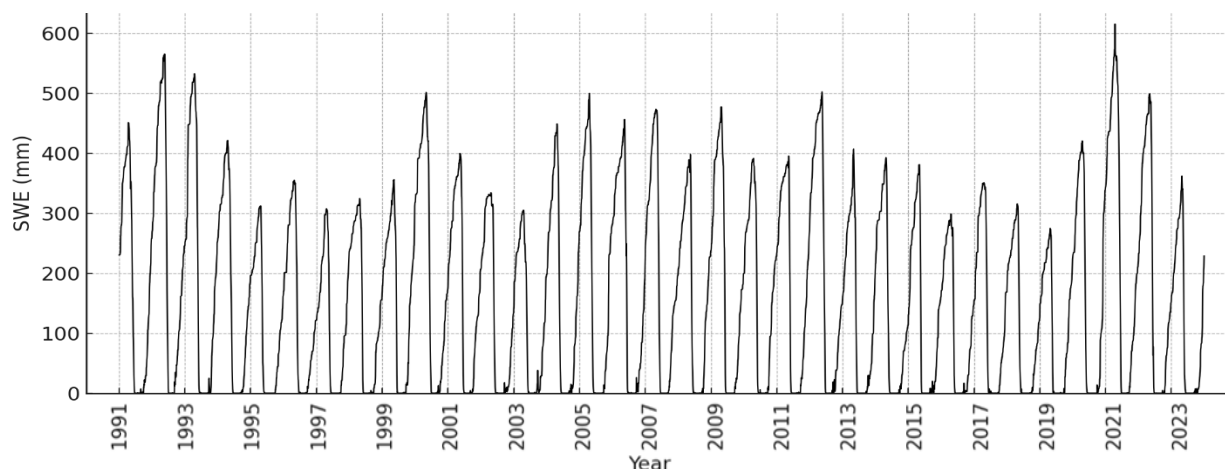


Figure 5.8: Monthly Mean Snow Water Equivalent (SWE) in the Gaat Héeni Watershed (1991–2023) extracted from ERA5-Land. SWE accumulation begins in October and steadily increases through winter, peaking in March at a mean value of 416.0 mm. The maximum SWE recorded was 606.1 mm in 2006, while the minimum was 300.7 mm in 1997.

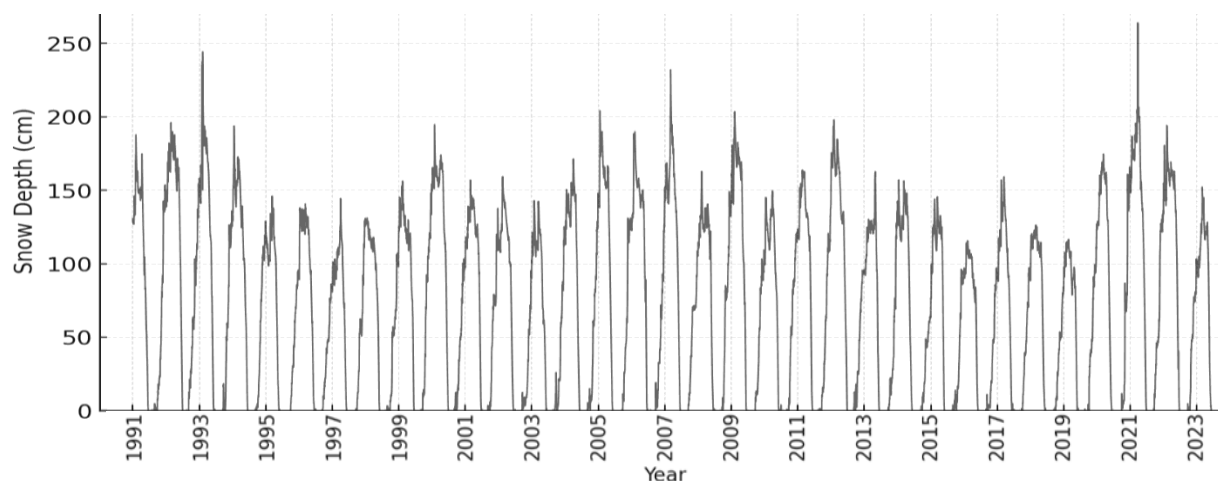


Figure 5.9: Monthly Mean Snow Depth across the Gaat Héeni Watershed (1991–2023). Extracted from ERA5-Land reanalysis data, the mean annual snow depth is 175.3 cm, with a maximum of 260.2 cm in 2005 and a minimum of 100.1 cm in 1995.

The seasonal precipitation distribution follows a well-defined pattern. Snowfall dominates winter months, and rainfall becomes the primary precipitation phase during the warmer seasons (Figure 5.10 and Figure 5.11). Winter (November–March) is characterized by high snowfall

accumulation, with December (52.7 mm), January (50.1 mm), and February (35.2 mm) recording the highest monthly mean snowfall totals. Spring (April–May) marks a transition from snowfall to rainfall, with April reporting 25.1 mm of mean monthly precipitation, predominantly as snow (0.6 mm rainfall), while May sees an increased rainfall fraction (13.8 mm) out of a mean total precipitation of 26.4 mm. Summer (June–August) is entirely rainfall-driven, with mean monthly precipitation increasing progressively from June (34.4 mm) to August (39.4 mm), reflecting enhanced convective activity and storm-driven precipitation variability. Autumn (September–October) represents a secondary wet season, with September (58.3 mm) and October (58.6 mm) recording the highest mean monthly precipitation.

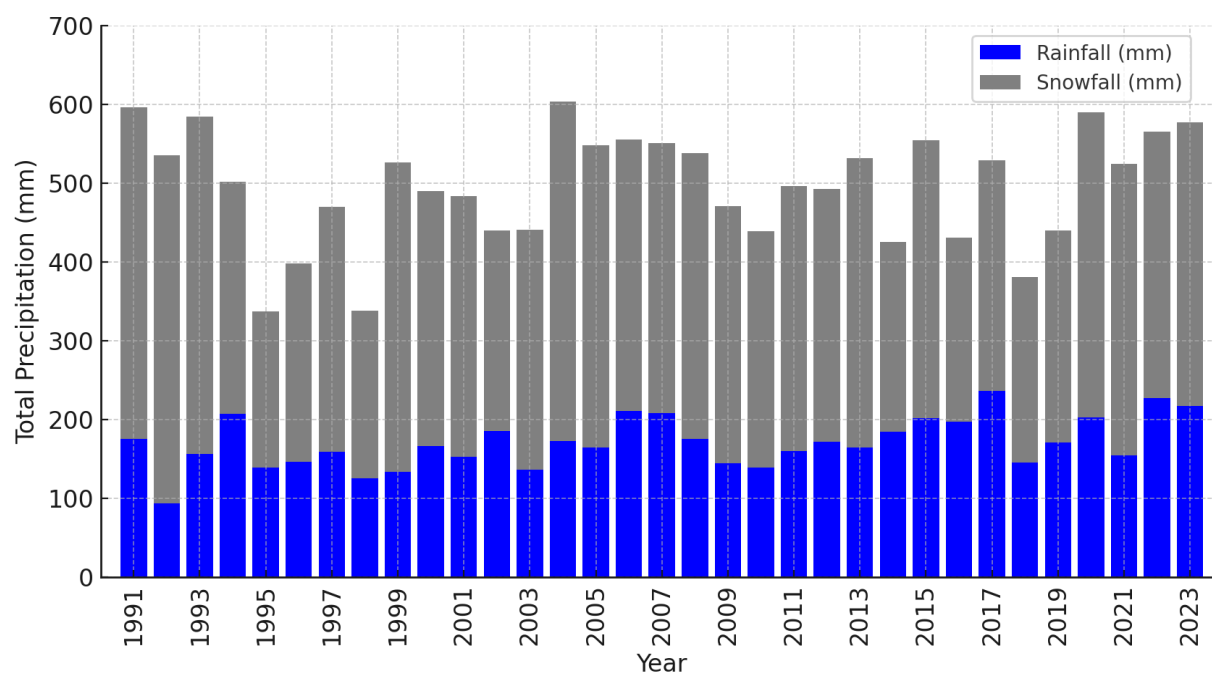


Figure 5.10: Total annual precipitation is partitioned into rainfall and snowfall within the Gaat Héeni Watershed. Data are extracted from ERA5-Land reanalysis data (1991-2023) and are spatially averaged across grid cells. Precipitation shows interannual variability, with snowfall consistently contributing the majority of total precipitation.

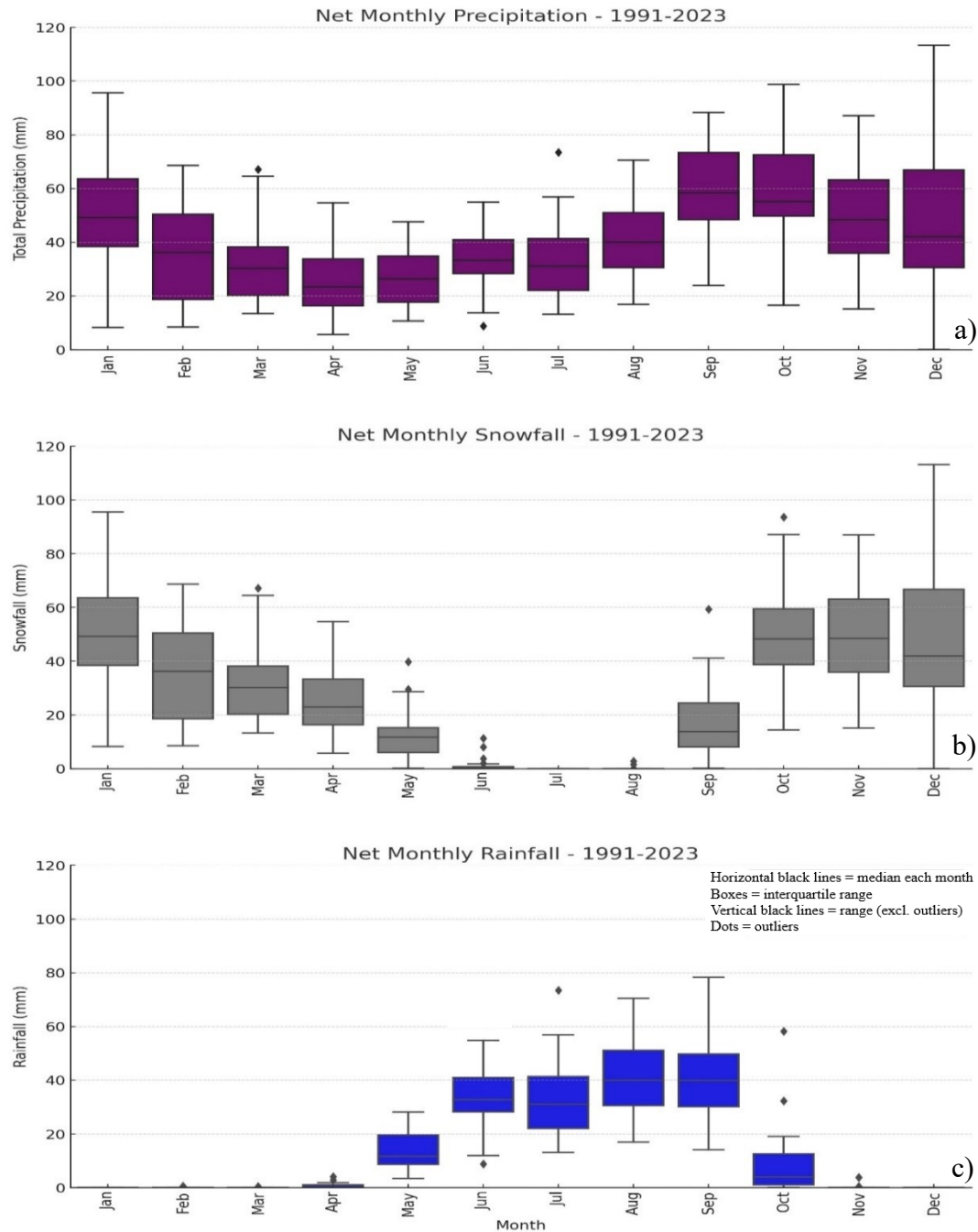


Figure 5.11: Monthly distribution of total precipitation (top), snowfall (middle), and rainfall (bottom) in the Gaat Héeni Watershed from 1991 to 2023. Total precipitation and snowfall are extracted from ERA5-Land, while rainfall is the difference between total precipitation and snowfall. Total precipitation shows peaks during autumn and early winter (October–January) and a secondary rise in late summer (September–October). Snowfall dominates from October to April, peaking in January, and is nearly absent by summer. In contrast, rainfall is minimal in winter but increases sharply from May to September, peaking in late summer.

5.4 Atmospheric River Climatology

ARs exhibit a distinct seasonal cycle across the study region with the highest frequency of ARs occurring in summer and fall, specifically August, September, and October (Figure 5.12).

September recorded the highest frequency, averaging approximately four ARs per month, followed closely by August. In contrast, the lowest AR activity was observed in March and April, where the average number of AR landfalls remained below one event per month.

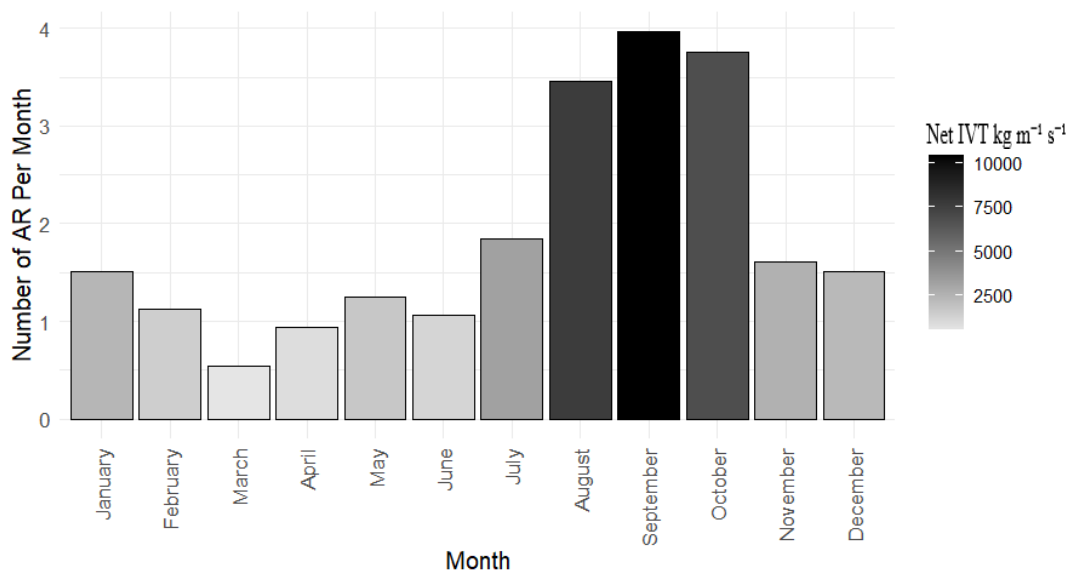


Figure 5.12: Average number of atmospheric river (AR) landfalls per month between 55°N and 60°N from 1991 to 2023, based on the SIO-R1 AR Catalog. Bar height represents the monthly AR frequency, while shading reflects the total monthly net IVT ($\text{kg m}^{-1} \text{s}^{-1}$), with darker bars indicating higher cumulative vapour transport. AR activity peaks in late summer and early fall, with September and August exhibiting the highest frequency of ARs.

IVT followed a similar seasonal pattern, with the highest values occurring in late summer and early autumn. The net IVT peaked in September, exceeding $10,000 \text{ kg m}^{-1} \text{s}^{-1}$, with August and October also exhibiting elevated values (Figure 5.13).

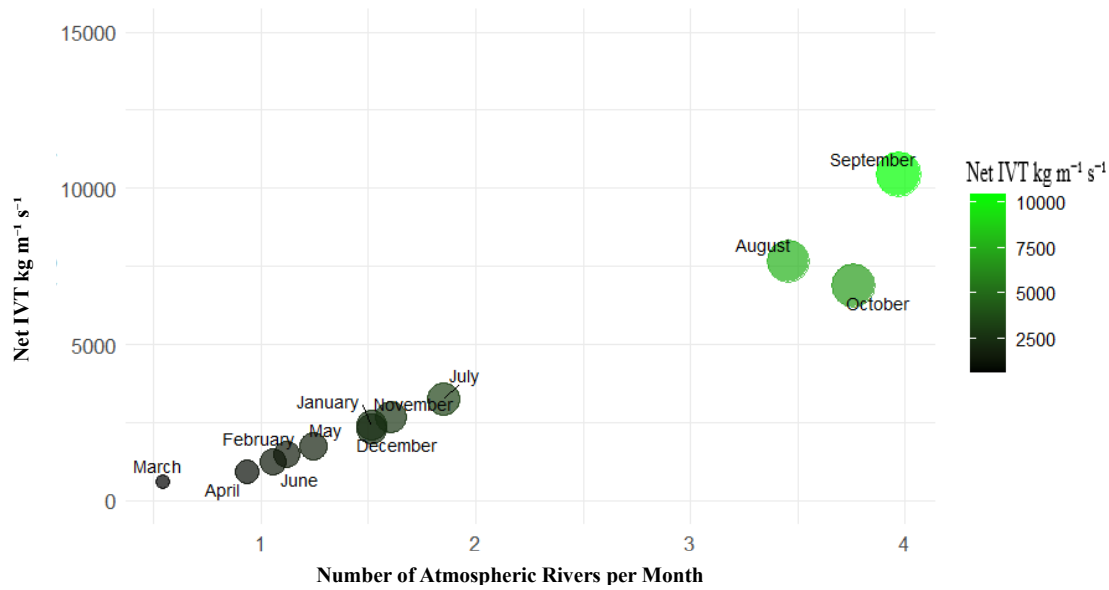


Figure 5.13: Climatological relationship between the mean monthly frequency of atmospheric river (AR) landfalls and the corresponding net integrated water vapour transport (IVT, $\text{kg m}^{-1} \text{s}^{-1}$) for the 55°N–60°N coastal sector from 1991 to 2023, using data from the SIO-R1 AR Catalog. Each point represents a month, with its position indicating the mean number of AR events and cumulative IVT, while colour denotes IVT magnitude.

The distribution of AR landfalls exhibited distinct seasonal and interannual variability, with notable increases in frequency and dispersion occurring in late summer and early fall (August, September, and October; Figure 5.14). The four-panel box and whisker plot illustrates the interquartile range (IQR), median, and occurrence of outliers for ARs across four distinct periods: 1991–2001, 2002–2012, 2013–2023, and 1991–2023.

Across all periods, the median number of ARs remained low from January through June before increasing sharply in July and peaking between August and October. The highest median values were recorded in September and October, consistent with climatological expectations of heightened AR activity during late summer and early fall (Radić et al., 2015). Outliers during these months highlight the episodic nature of high-activity years, contributing to overall interannual variability.

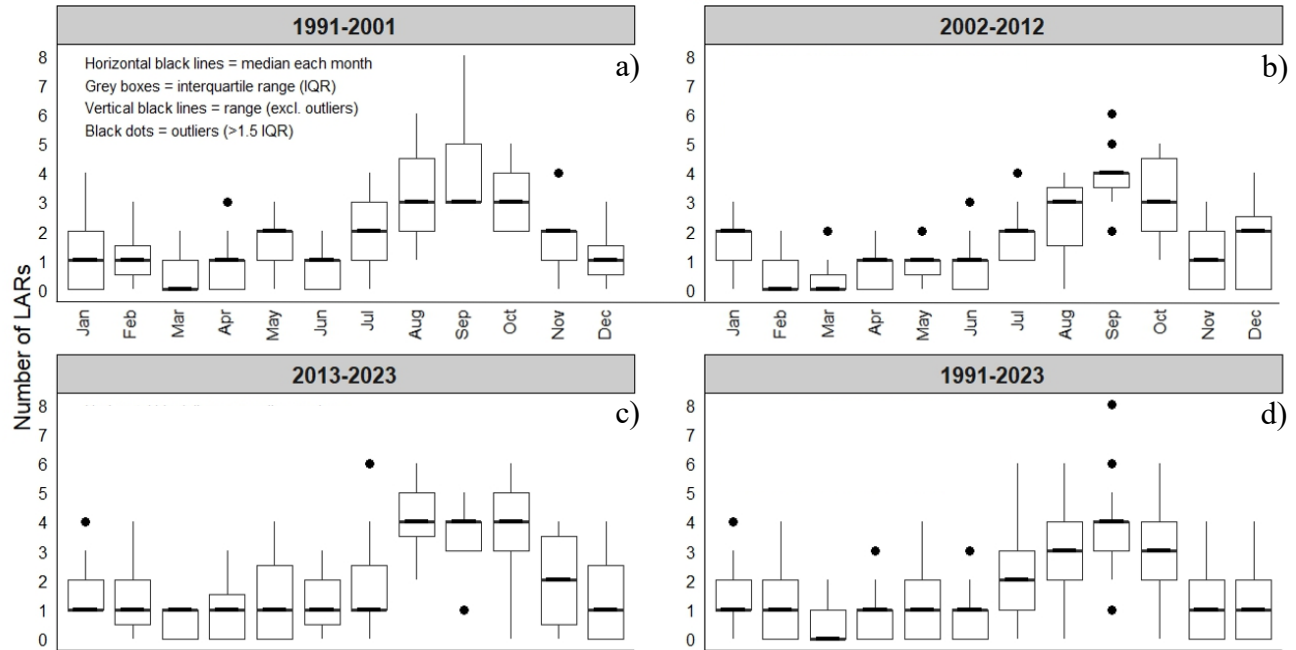


Figure 5.14: Monthly distribution of atmospheric river (AR) landfalls for (a) 1991–2001, (b) 2002–2012, (c) 2013–2023, and (d) 1991–2023. Box and whisker plots show AR counts with medians (black lines), interquartile range (grey boxes), and outliers ($>1.5 \times \text{IQR}$, black dots). A consistent late-summer to early-autumn (August–October) peak is evident, with higher medians and greater variability in recent periods (2002–2023) compared to 1991–2001.

5.5 Impact of ARs on the Study Region

The contribution of ARs to total precipitation within the study region from 1991 to 2023 exhibits seasonal and interannual variability (Figure 5.15). On average, ARs account for 15.9% to 39.1% of seasonal precipitation, with the most significant contributions occurring in fall and winter. Fall experiences the highest AR-driven precipitation fraction, with 37.9% of total seasonal precipitation attributed to ARs from 1991 to 2023. This proportion has varied over the past three decades, with the most recent period (2013–2023) showing an AR contribution of 39.1% in fall, compared to 36.3% (2002–2012) and 38.3% (1991–2001). Seasonality is further evident by ARs delivering 24.1 % of winter precipitation (1991–2023), 15.9 % in spring (1991–2023) and 22.9 % in summer (1991–2012). These seasonal contrasts reflect the synoptic conditions governing AR

occurrence and landfall intensity.

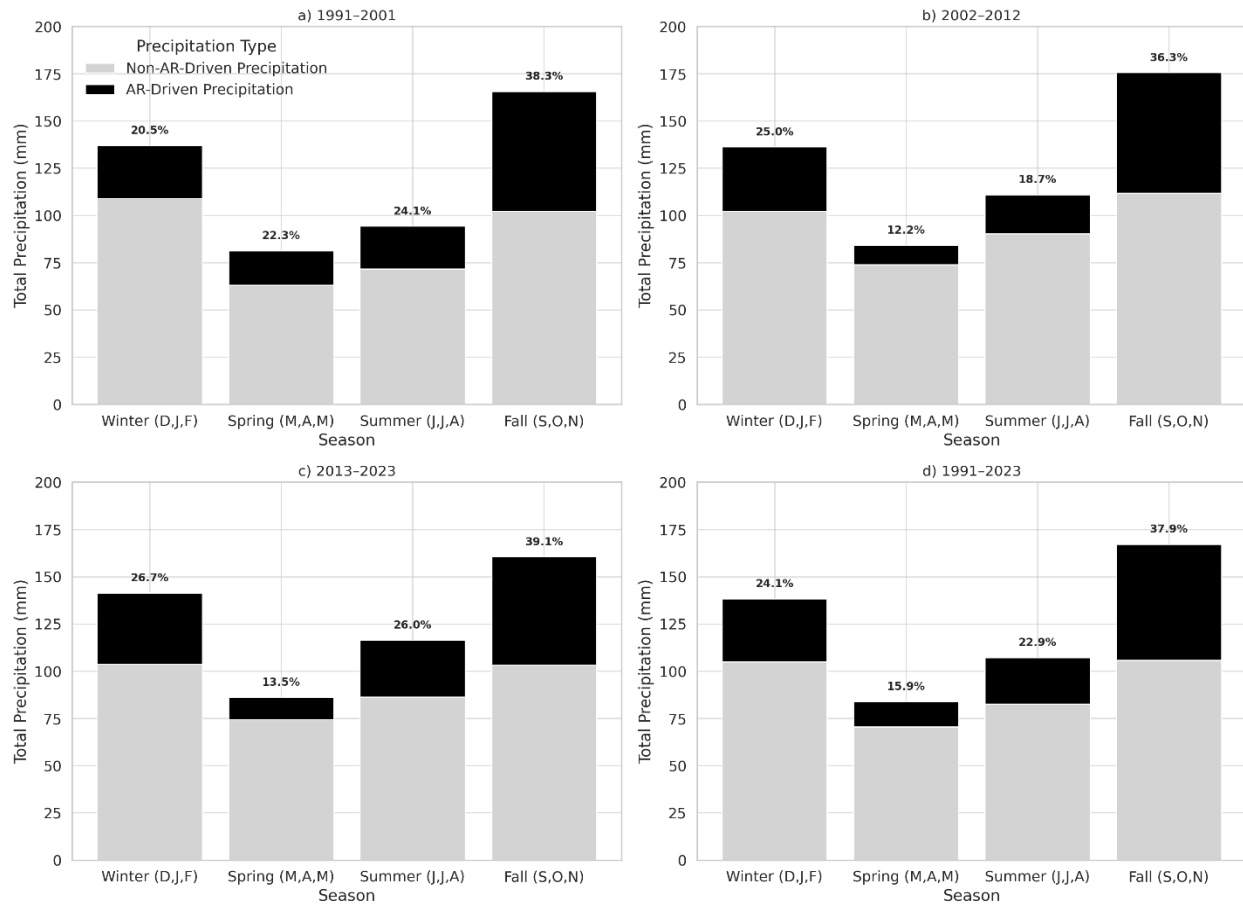


Figure 5.15: Seasonal contribution of atmospheric rivers (ARs) to total precipitation across the Gaat Héeni Watershed, aggregated by decade and over the whole study period using bias-corrected ERA5-Land precipitation and the SIO-R1 AR Catalog. Panel a) (top left) displays data for 1991–2001, with ARs contributing 20.5% of winter, 22.3% of spring, 24.1% of summer, and 38.3% of fall precipitation. Panel b) (top right) represents 2002–2012, showing increased winter AR influence (25.0%) but reduced spring and summer contributions (12.2% and 18.7%, respectively). Panel c) (bottom left) illustrates the most recent period, 2013–2023, where ARs account for 26.7% of winter, 13.5% of spring, 26.0% of summer, and 39.1% of fall precipitation. Panel d) (bottom right) shows the overall climatology for 1991–2023, highlighting that ARs contribute the largest share in fall (37.9%), followed by winter (24.1%), summer (22.9%), and spring (15.9%).

On an annual scale, AR events contributed between 16.4% and 37.8% of total annual precipitation in the Gaat Héeni Watershed from 1991 to 2023 (Figure 5.16). Annual AR-driven precipitation ranged from a minimum of 55.0 mm in 1995 to a maximum of 230.0 mm in 2004, while total annual precipitation varied from 330.0 mm (1996) to 610.0 mm (2004). When considering decadal means, AR-driven precipitation remains stable: 132 mm yr⁻¹ (27 %) in 1991–2001, 129 mm yr⁻¹ (25 %) in 2002–2012, and 137 mm yr⁻¹ (27 %) in 2013–2023. Combined,

these yield a mean of 133 mm yr⁻¹, representing 26.4 % of total precipitation for 1991–2023.

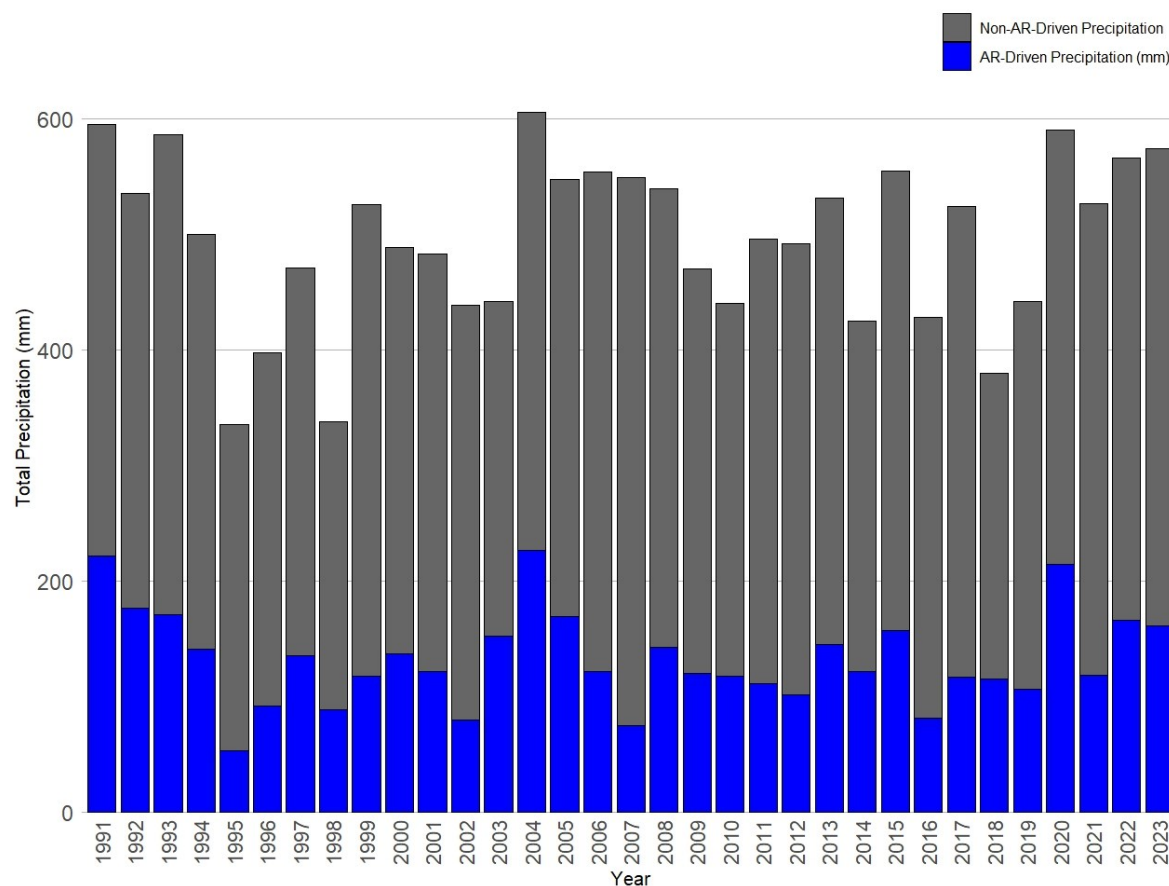


Figure 5.16: Annual total precipitation partitioned into AR-driven and non-AR-driven components for the Gaat Héeni Watershed from 1991 to 2023. Blue bars represent precipitation totals (mm) attributed to atmospheric river (AR) landfall events.

Heatmaps of monthly AR contributions over the 1991–2023 period illustrate the variability in AR-driven precipitation (Figure 5.17). Consistent with seasonal trends, AR activity is concentrated in the late summer to fall (August–November).

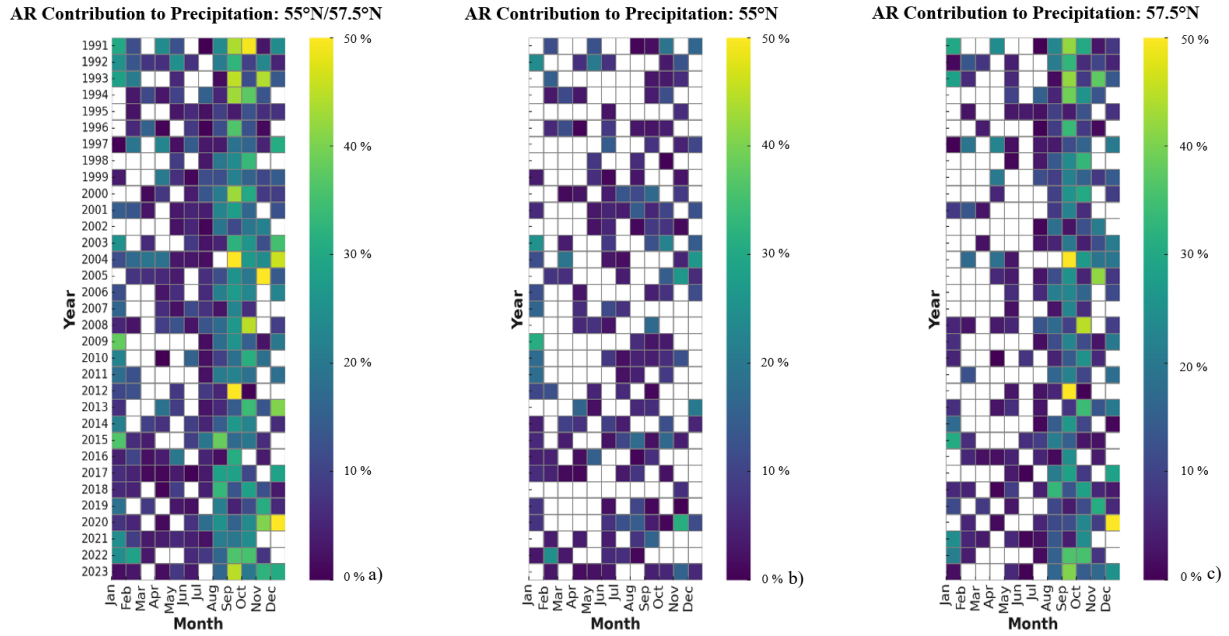


Figure 5.17: Monthly percentage contribution of atmospheric rivers (ARs) to total precipitation across three latitudinal bands within the study region, from 1991 to 2023. Panel a) (left) corresponds to the 55°–57.5°N band, panel b) (centre) to 55.0°N, and panel c) (right) to 57.5°N. Each heatmap cell represents a month's AR contribution as a percentage of total monthly precipitation, with colour intensity ranging from 0% (purple) to 50% (yellow). Clear seasonal patterns emerge in all panels, with the highest AR contributions typically occurring in fall and early winter (September–December).

To assess long-term trends, a Mann-Kendall (MK) test was applied to annual and seasonal AR-driven precipitation (Figure 5.18). No significant trends were found at the annual scale ($p = 0.765$), suggesting that while AR contributions fluctuate, they do not exhibit a statistically significant increase or decrease over the entire period.

At the seasonal scale, while winter ($p = 0.202$), summer ($p = 0.126$), and fall ($p = 0.415$) show trends of increasing precipitation, none approach significance. In contrast, spring precipitation exhibits a decreasing trend ($p = 0.158$), though it remains statistically insignificant. Collectively, these non-significant trends imply that interannual variability governs AR precipitation, precluding the emergence of a coherent long-term trend.





















Scale	Annual	Winter	Spring	Summer	Fall
1991-2001	 0.087	 0.283	 0.359	 0.060	 0.165
2002-2012	 0.121	 0.879	 0.274	 0.761	 0.359
2013-2023	 0.542	 0.879	 0.165	 1.000	 0.218
1991-2023	 0.765	 0.202	 0.158	 0.126	 0.415

Figure 5.18: Mann-Kendall trend test results for atmospheric river (AR) related precipitation across four time intervals (1991–2001, 2002–2012, 2013–2023, and 1991–2023), disaggregated by season and annually. Each cell displays the p-value of the test, with triangle markers indicating the direction of the trend: blue upward-facing triangles denote increasing trends, and red downward-facing triangles indicate decreasing trends. No trends across any time scale or season reach the conventional threshold for statistical significance ($p < 0.05$).

5.6 Discharge Sensitivity to Daily Precipitation and AR Events

To investigate the short-term hydrological impacts of ARs, daily precipitation and discharge data were analyzed for the 2024 monitoring season (17 June–10 October). This approach enabled evaluation of discharge sensitivity to AR-induced precipitation events.

Figure 5.19 presents the net precipitation (mm) for five temporal periods separated into AR-driven and non-AR-driven precipitation. AR events contributed to total precipitation in July (87.7%), early October (75.5%), and September (40.3%), indicating that a minority of days accounted for a substantial proportion of rainfall. In contrast, the late June period (17–30 June) showed minimal AR influence (19.3%).

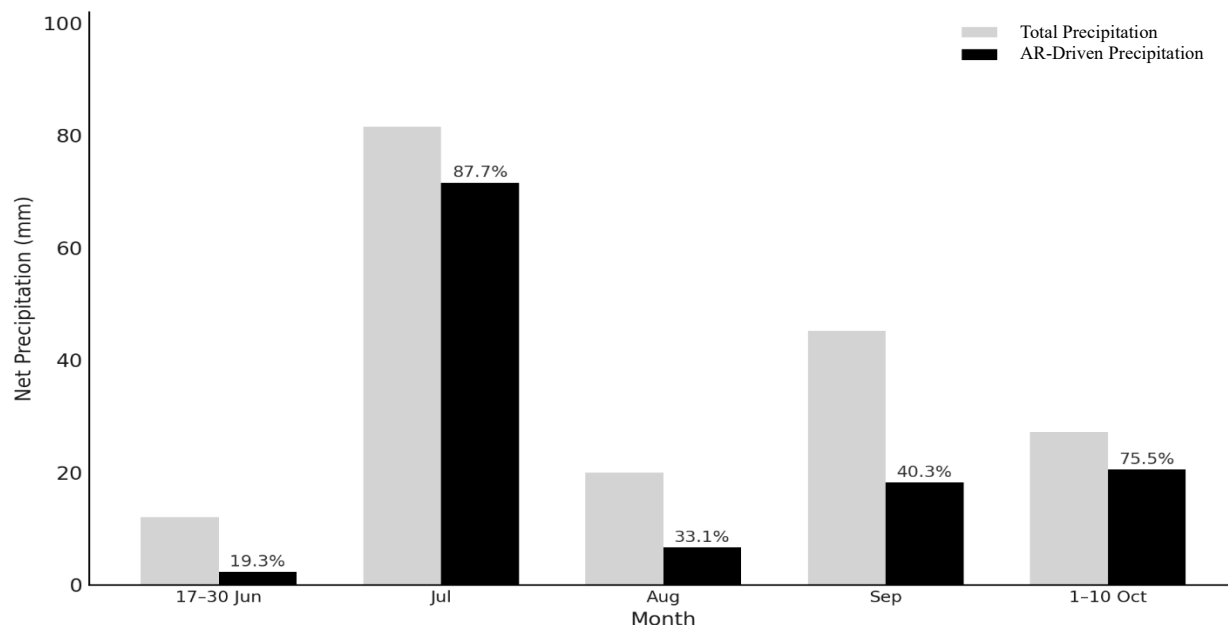


Figure 5.19: Monthly partitioning of precipitation into total precipitation and atmospheric river (AR) driven precipitation at the Gaat Héeni meteorological station for the 2024 observation period. Light gray bars represent total precipitation and black bars show the AR-driven subset, defined as precipitation occurring on the day of AR landfall and the subsequent day. Percentages indicate the proportion of monthly precipitation attributable to AR activity. The June and October labels reflect partial months of data coverage (17–30 June and 1–10 October).

Figure 5.20 illustrates daily discharge ($\text{m}^3 \text{s}^{-1}$) overlain with AR-driven and non-AR-driven precipitation. Distinct discharge responses were observed following high-intensity AR events, such as the 22–24 July event, when AR-driven precipitation triggered a sharp increase in discharge from $8.7 \text{ m}^3 \text{s}^{-1}$ to $30.0 \text{ m}^3 \text{s}^{-1}$.

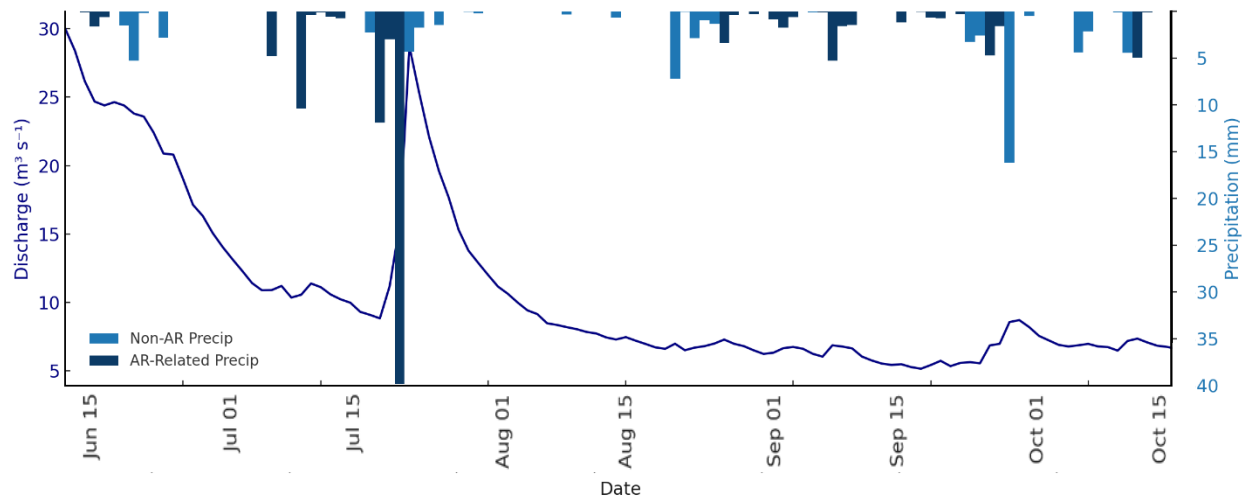


Figure 5.20: Daily discharge ($\text{m}^3 \text{s}^{-1}$; navy line) and precipitation (mm; inverted bars) at the Gaat Héeni meteorological station from 17 June to 10 October 2024. Precipitation is partitioned into AR-driven (dark blue) and non-AR-driven (blue) totals, with each bar representing cumulative daily rainfall. Discharge reflects mean daily values derived from continuous measurements. Following snowmelt-driven attenuation in June, baseflows stabilize at low levels throughout late summer and early autumn, punctuated by a major AR event in mid-July and more minor rainfall-driven fluctuations in late September and early October.

Centroid lag to peak discharge was calculated for precipitation events across the 2024

observation period to characterize the timing between precipitation inputs and resultant river discharge response. Time between the centroid of precipitation and resulting discharge peak ranged from 0.2 to 5.7 days, with a mean of 2.1 days and a median of 1.6 days. These values highlight the rapid and variable response of the Gaat Héeni Watershed to precipitation inputs.

5.7 Quantifying Optimal Hydrological Conditions for Successful Gaat Barrier Passage

Between 5 and 30 July 2024, I conducted daily video monitoring at obstruction SR3-3 on the Gaat Héeni to quantify jump success (Figure 5.21). Hourly discharge and water temperature measurements recorded during each day's observation window were averaged to yield daily means, ranging from 10.57°C to 14.11°C and $8.85 \text{ m}^3 \text{s}^{-1}$ to $28.02 \text{ m}^3 \text{s}^{-1}$. These hydrological conditions provide the framework for interpreting temporal patterns in passage behaviour under baseline and elevated discharge events. Observational coverage was curtailed during the peak discharge interval (24–27 July) owing to safety constraints imposed by an AR event (Figure

5.21), resulting in data gaps precisely when discharge and temperature reached their maximum values.

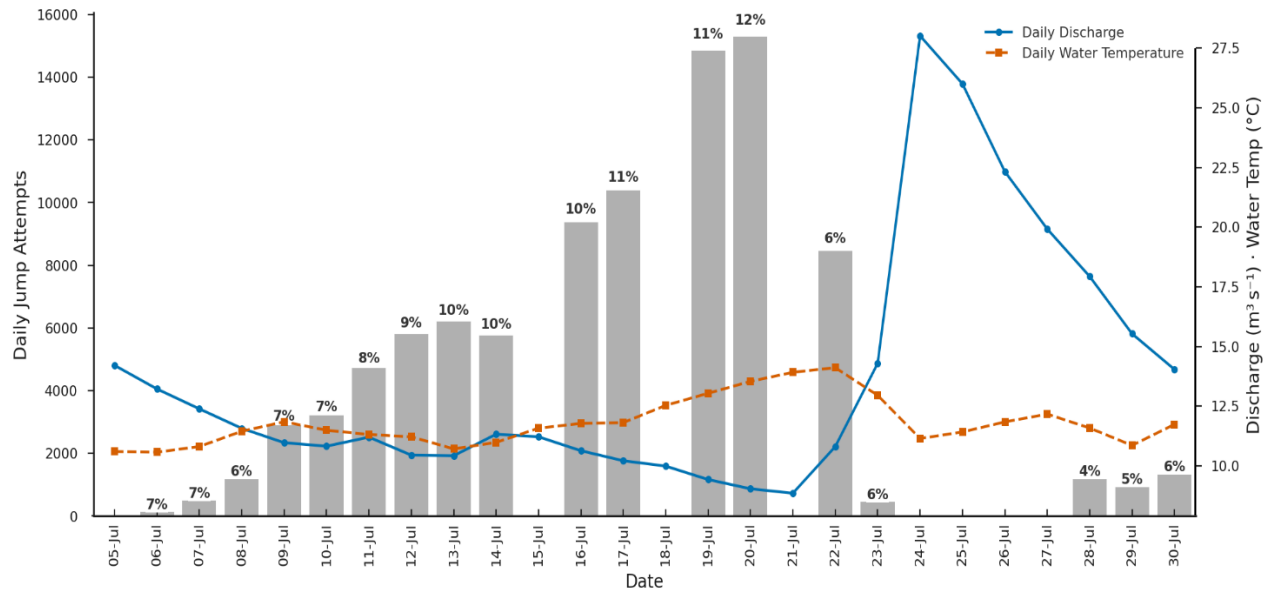


Figure 5.21: Composite daily time series of Gaat passage success at obstruction SR3-3 on the Gaat Héeni (5–30 July 2024). Vertical grey bars show total daily jump attempt counts recorded by video monitoring, over which daily mean river discharge (blue circles and solid line) and daily mean water temperature (orange square and dashed line) are overlaid. Six 15-minute monitoring blocks were conducted each day except on 23 July, when only two blocks were run. The percentages above each bar indicate the daily percentage of successful jumps rounded to the nearest percent. Monitoring was suspended on 15 and 18 July due to crew fatigue and on 24–27 July under unsafe river conditions. The 22–24 July interval corresponds to an atmospheric river event during which both discharge and temperature peaked.

To quantify how water temperature and river discharge jointly influence Gaat jump-success probability, I fitted a logistic-regression model that includes linear and quadratic terms for temperature (T , $^{\circ}\text{C}$) and discharge (Q , $\text{m}^3 \text{s}^{-1}$), as detailed in Section 4.7. Figure 5.22 presents the model's predicted probability surface as a two-dimensional heatmap. The colour gradient, from deep purple through magenta to yellow, indicates the probability of successful jumps. On the prediction grid, the model yields a maximum probability of 0.157 at a water temperature of 15.22 $^{\circ}\text{C}$ and river discharge of 12.15 $\text{m}^3 \text{s}^{-1}$. Across the 110 observed 15-minute blocks, fitted probabilities range from 0.016 (minimum) to 0.15 (maximum), with a mean of 0.06, a median of 0.06, and interquartile values of 0.04 (1st quartile) and 0.07 (3rd quartile).

Predicted success peaks (~ 0.13 – 0.16) at temperatures of 14–15 $^{\circ}\text{C}$ combined with moderate

discharges of 10–12 m³ s⁻¹, whereas probabilities fall below 0.05 under extremes of high discharge (≥ 16 m³ s⁻¹) or low temperature (≤ 11 °C).

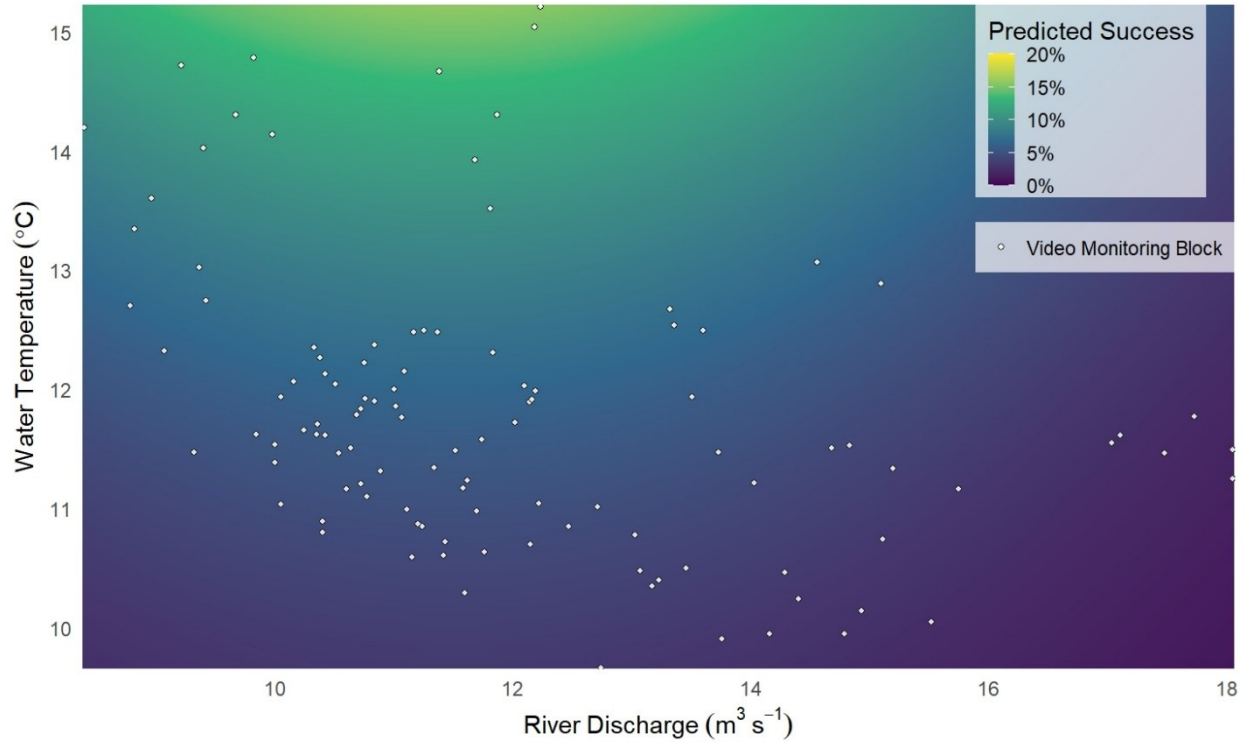


Figure 5.22: Heatmap of predicted jump success probability from a logistic-regression model (with linear and quadratic terms for water temperature T and discharge Q) fitted to 15-minute block observations collected at obstruction SR3-3 (5–30 July 2024). Colour intensity (deep purple to yellow) reflects the modelled values, which range from a minimum of 0.01 at $T = 9.66$ °C and $Q = 12.85$ m³ s⁻¹ to a maximum of 0.16 at $T = 15.22$ °C and $Q = 12.15$ m³ s⁻¹. White circles represent the water temperature and discharge conditions observed during each video monitoring block.

To assess the individual contributions of each predictor within the fitted logistic regression model, I evaluated coefficient estimates using Wald z-tests (Table 5.1).

Table 5.1: Wald Z-Test Results for Hydrologic Predictors of Gaat Jump Success at SR3-3

<i>Predictor</i>	<i>Estimate (β)</i>	<i>Std. Error</i>	<i>z value</i>	<i>p-value</i>
(Intercept)	-10.61	2.09	-5.07	< 0.001
T	+0.38	0.28	+1.33	0.182
T^2	-0.0028	0.011	-0.26	0.796
Q	+0.66	0.099	+6.69	< 0.001
Q^2	-0.029	0.0043	-6.71	< 0.001

Among the predictor variables, discharge (Q) showed a significant positive linear effect on jump success ($\beta = 0.66$, $p < 0.001$). This suggests that increasing discharge increases the likelihood of a successful jump, likely by improving hydraulic depth and discharge. Furthermore, the quadratic term for discharge (Q^2) was also significant and negative ($\beta = -0.029$, $p < 0.001$), confirming the presence of a non-linear discharge relationship. Together, these terms indicate that passage success increases with discharge up to a peak, after which excessive discharge reduces success.

In contrast, temperature (T) and temperature squared (T^2) were not statistically significant ($p = 0.182$ and $p = 0.796$, respectively). This suggests that within the observed summer water temperature range, water temperature had no strong linear or curvilinear effect on jump success.

5.8 Influence of Jump Success on Gaat Arrival at Gaat Áayi

The relationship between daily jump success (p_d) at SR3-3 and arrival anomalies (ΔA) at Gaat Áayi was investigated using linear regression models with lag intervals of one, two, and three days.

The regression results revealed a significant, positive relationship between daily jump success and Gaat arrival anomalies at all lag intervals. The model with a 1-day lag exhibited an R^2 value

of 0.640 and a p-value of < 0.01 , indicating that daily jump success accounted for approximately 64% of the variation in arrival anomalies at the 1-day lag. The model with a 2-day lag showed an even stronger relationship, with an R^2 of 0.709 and a p-value of < 0.01 , suggesting that jump success was a more reliable predictor of arrival anomalies after a 2-day delay. Finally, the 3-day lag model had an R^2 of 0.431 and a p-value of < 0.01 , which, although weaker than the 2-day model, still demonstrated a statistically significant association between jump success and arrival anomalies at longer lags.

Chapter 6: DISCUSSION

AR-driven precipitation influences hydrological variability in the Gaat Héeni Watershed, shaping seasonal and annual precipitation patterns and influencing river discharge (Section 6.1). As AR frequency, intensity, and seasonal distribution shift, these changes influence Gaat migration (Section 6.2). High and low AR-driven discharge have been linked to run collapses, underscoring the need to establish hydrological thresholds for successful arrival of Gaat at Gaat Áayi (Section 6.3). Fluctuations in river discharge, partly driven by ARs, together with variations in water temperature, determine the feasibility of passage through critical geomorphic barriers. To better understand these impacts, video monitoring was employed at SR3-3 to assess Gaat passage success (Section 6.4).

6.1 Contribution of ARs to Seasonal and Annual Precipitation

ARs contribute to seasonal and annual precipitation variability, particularly in coastal and mountainous regions (Ralph et al., 2019; Sharma & Déry, 2020). In the Gaat Héeni Watershed, ARs account for 15.9% to 37.9% of seasonal precipitation from 1991-2023 (Figure 5.15), with the highest contributions occurring in fall (37.9%) and winter (24.1%). Notably, the fraction of fall precipitation attributed to ARs (Figure 5.15) has varied only slightly across decades with no statistically significant trend. On an annual scale, AR-driven precipitation in the Gaat Héeni Watershed ranged from 55.0 mm in 1995 to 230.0 mm in 2004, with a mean annual contribution of 139.6 mm over the 1991–2023 period (Figure 5.16). These events accounted for 16.4% to 37.8% of total annual precipitation, highlighting their influence on the hydrology of the Gaat Héeni Watershed. If fall AR precipitation increases (Radić et al., 2015), it could enhance SWE accumulation (Figure 5.11), elevating spring discharge volumes. Additionally, elevated AR activity during summer can generate abrupt river discharge and water temperature increases

during the Gaat migration period. For example, during the 2024 observation period, an AR made landfall from 22 to 24 July, accounting for 88% of that month's precipitation (Figure 5.19) and increasing discharge from 8.7 to 30.0 m³ s⁻¹ (Figures 5.20 and 5.21).

Interannual variability in AR frequency and intensity further influences precipitation patterns. Although no statistically significant trend ($p = 0.765$) in total AR-driven precipitation is present at an annual scale (Figure 5.18), seasonal shifts are evident. The Mann-Kendall test (Figure 5.18) suggests a possible increase in summer ($p = 0.126$) and fall ($p = 0.415$) AR contributions, though neither trend is statistically significant. These findings align with research showing enhanced AR activity in late summer and fall along the North Pacific Coast (Gershunov et al., 2019; Sobral & Déry, 2023).

6.2 The Impact of Changing Atmospheric River Patterns on Gaat

Changes in the distribution and intensity of ARs shape the hydrological conditions of the Gaat Héeni Watershed, with potential consequences for the daily arrival of Gaat at Gaat Áayi and annual escapement. The frequency, duration, and intensity of ARs modulate precipitation patterns, river discharge, and water temperature. These are key variables governing the ability of Gaat to navigate critical migration barriers (Cannon et al., 2017; Ralph et al., 2019). Section 6.2 examines how these hydrological factors may influence escapement trends by integrating escapement and hydrological records from 1991 to 2023. Notably, escapement data reveal partial run collapses in 2018 and 2021, with only 13 and 26 Gaat reaching Gaat Áayi, respectively, compared to the long-term average of 3031 Gaat (Figure 1.2).

River discharge during the Gaat migration period is influenced by snow accumulated in the fall (August to November) and precipitation from the current year. In 2017, the Gaat Héeni

Watershed received 117 mm of AR-driven precipitation, representing 22% of that year's total, and in 2018, 115 mm of AR-driven precipitation, accounting for 30% of annual precipitation (Figure 5.16). The two-year average of 116 mm yr⁻¹ (26%) falls below the decadal mean of 137 mm yr⁻¹ (27%) for the period 2012–2023 (Figure 5.16). This depressed AR-driven precipitation input occurred alongside subdued summer discharge conditions (Taku River Tlingit Fisheries Department, 2019), which were associated with higher jump heights at key barriers and reduced hydraulic connectivity. These conditions likely impeded upstream movement by elevating fallback rates and prolonging migration durations, consistent with observations from other watersheds (Padilla et al., 2015; Mathes et al., 2010).

In 2020, the Gaat Héeni Watershed recorded 214.8 mm of AR-driven precipitation, representing 36.4% of annual precipitation, while in 2021, AR-driven precipitation totaled 118.6 mm, accounting for 22.5% of annual precipitation (Figure 5.16). The two-year average of 166.7 mm yr⁻¹ (29.4%) exceeds the decadal mean of 137 mm yr⁻¹ (27%) for the period 2013–2023 (Figure 5.16). This elevated AR-driven precipitation contributed to elevated snowpack accumulation during the 2020–2021 winter (Kolot et al., 2021), leading to elevated summer discharge (Taku River Tlingit Fisheries Department, 2022). These high discharge conditions disrupted migration success and resulted in higher-than-normal numbers of Gaat holding below SR3-3 (Taku River Tlingit Fisheries Department, 2022). Similar to findings in other watersheds, elevated discharge and turbulence reduce passage success, particularly at steep-gradient canyon sites where hydraulic complexity is elevated (MacNutt et al., 2006).

Analysis from Section 5.8 demonstrates a temporal linkage between jump success at SR3-3 and the arrival of Gaat at Gaat Áayi, with the strongest correlation ($R^2 = 0.709$; $p < 0.001$) observed

at a two-day lag interval. During the 2024 monitoring season, a prominent AR event (22-24 July) increased river discharge from $8.7 \text{ m}^3 \text{ s}^{-1}$ to $30.0 \text{ m}^3 \text{ s}^{-1}$ (Figure 5.20), surpassing optimal discharge thresholds ($10\text{--}12 \text{ m}^3 \text{ s}^{-1}$) identified in Section 5.7. Before this AR event, holding pools immediately downstream of SR3-3 were already observed to be at high capacity, indicating significant Gaat accumulation and emphasizing the potential impact of rapidly increased discharge in delaying migration. Given the identified two-day lag from passage success at SR3-3 to the arrival of Gaat at Gaat Áayi, it is likely that the AR-driven discharge increase on 22-24 July significantly influenced short-term outcomes. However, I cannot make a clear statistical linkage as observations at SR3-3 did not begin until 28 July 2024, four days after the AR event.

While the timing of these escapement events aligns with notable hydrologic variation, this thesis acknowledges the absence of a comprehensive statistical linkage between AR-driven hydrologic extremes and longer-term escapement trends. The observational nature of these findings means that explicit attribution of escapement solely to AR activity remains speculative and requires further analysis.

These findings suggest high and low AR-driven precipitation extremes are associated with escapement variation at Gaat Áayi. Given projections of increasing AR frequency and intensity (Arora et al., 2025; Radić et al., 2015), understanding the hydrological mechanisms regulating Gaat escapement success will be essential for sustaining populations.

6.3 Hydrological thresholds for Gaat Arrival at Gaat Áayi

The Gaat Héeni Watershed exhibits a rapid and variable hydrological response to precipitation, reflecting the steep gradients and confined channels. Discharge sensitivity analysis from Section 5.6 found that the lag between the centroid of precipitation and the corresponding discharge peak

ranged from 0.2 to 5.7 days, with a mean of 2.1 days and a median of 1.6 days. This underscores the watershed's quick runoff response, meaning shifts in precipitation timing, particularly those driven by ARs, can have rapid implications on river discharge.

Gaat escapement in the Gaat Héeni Watershed is influenced by the hydrological constraints of water temperature and river discharge, which determine the feasibility of passage through geomorphic barriers, including SR3-3 (Taku River Tlingit First Nation Fisheries Department, 2017). However, escapement is also shaped by extrinsic factors, including ocean survival (Beamish et al., 2016; Crossin et al., 2008), pre-spawn mortality (Jeffries et al., 2012), and interannual variability in run strength. Data collected from 5-30 July 2024, not including 15, 18, 24, 25, 26, and 27 July, indicate optimal jump success was seen with discharge levels between 10–12 m³ s⁻¹ (Figure 5.22). Notably, an increase in river discharge during video monitoring from 8.7 m³ s⁻¹ to a peak of 18.05 m³ s⁻¹ from 22-24 July coincided with an AR event on 22 July (Figure 5.20). Although river discharge rose to 30 m³ s⁻¹, jump behaviour was not recorded during this interval due to safety constraints. These observations illustrate how AR events can rapidly alter hydrological conditions, potentially constraining passage success.

Water temperature is a critical factor influencing the arrival of Gaat at Gaat Áayi (Atlas et al., 2021; Hague et al., 2011). Within the range observed in July 2024, no water temperatures exceeded 15.28 °C, and jump success was highest between 13–15 °C (Figure 5.22). However, statistical analysis (Table 5.1) shows that water temperature was not a statistically significant predictor of jump success at SR3-3 (linear term $p = 0.182$; quadratic term $p = 0.796$), reducing confidence in conclusions drawn from temperature data alone. While laboratory studies and migration data suggest that performance declines above 19 °C (Keefer et al., 2008; Quinn et al.,

1997), this study did not observe or model behaviour at higher temperatures. Projected warming trends (Arora et al., 2025; Reid et al., 2022; SNAP-EWHALE, 2012) suggest that rising summer temperatures may further constrain the thermal window required for the successful arrival of Gaat at Gaat Áayi.

In contrast to water temperature data, river discharge was a statistically significant predictor of jump success at SR3-3 (Table 5.1; linear term $p < 0.001$; quadratic term $p < 0.001$). Discharge fluctuations strongly determine whether Gaat can successfully overcome migration barriers. During the 2021 partial run collapse, high discharge may have increased the hydraulic complexity of SR3-3, contributing to the low escapement observed that year (26 fish). Gaat are forced to expend greater energy at high discharge to maintain their position and overcome obstacles (Hinch & Rand, 1998). This effect is particularly pronounced at SR3-3 (Taku River Tlingit Fisheries Department, 2022), where the absence of alternative migration routes prevents bypassing turbulent flow zones and reduces passage success (Caudill et al., 2007; Enders et al., 2009; Rand et al., 2006).

Conversely, when discharge falls below $9 \text{ m}^3 \text{ s}^{-1}$, hydraulic connectivity between pools and passage corridors is disrupted. This increases the vertical height of obstacles such as the SR3-3 waterfall feature, making passage more challenging. The precise threshold at which connectivity breaks down may vary depending on site-specific conditions. For example, in 2018, escapement decreased to 13 individuals during a low-discharge year, but in 2019, 605 individuals passed under similar discharge conditions. This suggests that other factors, including channel modifications at SR3-3 (Taku River Tlingit Fisheries Department, 2019) or interannual differences in run size, may influence passage outcomes.

6.4 Evaluating the Effectiveness of Video Monitoring for Assessing Fish Passage Success

Video monitoring at SR3-3 during the 2024 migration season yielded detailed insights into Gaat jump success by capturing fish behaviour under varying discharge and temperature regimes.

Using a fixed camera at a consistent vantage point, this non-invasive approach recorded individual jump attempts and, when paired with concurrent measurements of river discharge and water temperature, allowed us to identify specific hydrological thresholds linked to successful passage. This method helped characterize the hydrological thresholds associated with observed jump success by integrating video observation with river discharge and water temperature.

Although beneficial, video monitoring at SR3-3 had several limitations. Waterfall spray and turbulence from SR3-3 obscured portions of the video footage, particularly at higher discharges. This reduced the number of fully observable jump attempts and likely led to underestimating total passage attempts and success rates. Additionally, Gaat probably ascended via routes hidden behind SR3-3, making it challenging to quantify total passage accurately. Turbidity following AR-driven precipitation events further reduced video clarity. Finally, the labour-intensive manual review of footage required frame-by-frame analysis to assess passage attempts, introducing potential observer bias and misclassification errors.

Chapter 7: CONCLUSION

7.1 Summary

This study examines the influence of ARs on hydrologic variability and its subsequent effects on Gaat migration in the Gaat Héeni Watershed. The research quantifies AR-driven precipitation's seasonal and interannual variability by integrating ERA5-Land reanalysis data, SIO-R1 Atmospheric River Catalog outputs, in-situ hydrometric observations, and escapement monitoring records. It defines the hydrometric thresholds governing Gaat migration success. Where appropriate, hydrologic and biological responses are presented as observational rather than causal. These findings provide critical information for fisheries management in a region increasingly impacted by hydrologic extremes.

Sections 5.2 to 5.3 establish the long-term climatological and hydrometeorological conditions of the Gaat Héeni Watershed (1991–2023), revealing trends in precipitation, air temperature, and seasonal hydrologic responses. Annual precipitation has increased at a rate of 0.93 mm per year, with a distinct shift toward higher rainfall fractions after 2010. Before 2010, the mean annual rainfall was 160.6 mm, whereas post-2010, it increased to 183.8 mm, marking a net gain of 23.2 mm per year.

The seasonal distribution of precipitation follows a predictable snowfall-to-rainfall transition, with snowfall dominating winter months (December–February) and rainfall peaking during late summer and early fall (August–October). The highest precipitation volumes occur between September and November, with ARs accounting for up to 39.1% of fall precipitation (2013–2023). The increasing late-season precipitation intensity suggests a growing influence of ARs on discharge variability, particularly during the critical migration window for Gaat.

Air temperature reanalysis records indicate a seasonal warming trend, with July exhibiting the highest mean air temperature at 10.9 °C. The interaction between increased AR-driven precipitation and rising air temperatures has resulted in more frequent high-discharge events in the fall. However, whether these trends have translated to measurable long-term changes in escapement remains uncertain.

Section 5.4 examines AR frequency, seasonal variability, and long-term trends using data from the SIO-R1 Atmospheric River Catalog (1991–2023). Results confirm that AR landfalls exhibit a distinct seasonal cycle, with peak activity occurring in late summer and early fall. The highest AR frequency occurs in September, averaging four landfalling events per month, followed closely by August and October. Net IVT values exceed 10,000 kg m⁻¹ s⁻¹ in September, making this month the most hydrologically active.

Over the past three decades, the frequency of AR landfalls has increased, particularly in late summer and fall. The most recent period (2013–2023) has shown a higher number of AR landfalls than previous decades, with increased interannual variability. This trend suggests that AR-driven hydrologic variability will continue to be a dominant force shaping precipitation patterns.

Section 5.5 applied an event-based precipitation framework to quantify AR contribution to total precipitation. Results indicate that AR-driven precipitation accounts for 15.9% to 39.1% of seasonal precipitation, with the highest fractions occurring in fall and winter. Highlighting this, fall precipitation is heavily influenced by ARs with contributions of ARs to total precipitation ranging from 38.3% (1991–2001) to 39.1% (2013–2023).

A Mann-Kendall trend analysis applied to annual and seasonal AR-driven precipitation found no statistically significant trends at the annual scale ($p = 0.765$). However, at the seasonal scale, AR contributions in fall, winter, and summer show increasing trends but do not reach statistical significance at the 0.05 level. These findings highlight the high interannual variability of AR-driven precipitation, reinforcing the need for adaptive hydrologic monitoring to anticipate extreme discharge events.

High-resolution observations during the 2024 monitoring season revealed that the Gaat Héeni Watershed exhibits a dynamic hydrologic response, with discharge reacting rapidly to AR and non-AR rainfall events. As detailed in Section 5.6, the discharge response to precipitation during the 2024 observation period was strongly modulated by AR activity. Additionally, centroid lag analysis revealed that discharge peaks typically occurred within 0.2 to 5.7 days following precipitation inputs, with a mean lag of 2.1 days and a median of 1.6 days, indicative of a generally rapid but variable hydrological response. The most pronounced discharge event occurred during the 22–24 July AR, when discharge rapidly increased from baseflow ($\sim 8.7 \text{ m}^3 \text{ s}^{-1}$) to $30.0 \text{ m}^3 \text{ s}^{-1}$, exceeding the $16 \text{ m}^3 \text{ s}^{-1}$ hydraulic threshold for upstream fish passage at SR3-3. These findings underscore the nonlinear nature of runoff generation in this steep catchment and its implications for passage timing and the arrival of Gaat at Gaat Áayi.

Observational data from Section 5.7 reveal a non-linear relationship between discharge, water temperature, and jump success rates at SR3-3. Logistic regression modelling (Table 5.1) demonstrated that river discharge influenced jump success (linear term, $p < 0.001$; quadratic term, $p < 0.001$), whereas water temperature was not a statistically significant predictor (linear term, $p = 0.182$; quadratic term, $p = 0.796$), reducing confidence in water temperature-based

conclusions. Passage at SR3-3 was most successful at discharge levels between 10–12 m³ s⁻¹ (Figure 5.22), conditions that maintain laminar flow and facilitate efficient jumping. When river discharge exceeds approximately 16 m³ s⁻¹, increased flow turbulence and velocity gradients reduce passage success. Conversely, low discharge conditions (<9 m³ s⁻¹) increase jump distance requirements, thereby reducing passage success due to insufficient water depth and disrupted hydraulic connectivity (Taku River Tlingit Fisheries Department, 2017).

Analysis in Section 5.8 clarified the temporal relationship between jump success at SR3-3 and the arrival of Gaat at Gaat Áayi, identifying a significant and strong predictive relationship at a two-day lag ($R^2 = 0.709$, $p < 0.001$). Despite statistical relationships, monitoring gaps during peak discharge periods (particularly during the 22-24 July AR event) limit the robustness of these conclusions under extreme discharge conditions.

While river discharge emerged as the primary hydrological factor influencing jump success, water temperature is known to affect migration efficiency and energy expenditure (Atlas et al., 2021; Hague et al., 2011). Video monitoring at SR3-3 indicated higher passage probability between 13–15 °C, although no statistically significant relationship was detected (Table 5.1). Limited observational coverage at higher water temperatures (>15 °C) prevents robust conclusions on the upper thermal limits of successful passage, where previous work has shown impacts of elevated water temperature. Given projected regional warming trends (Reid et al., 2022; SNAP-EWHALE, 2012), future increases in water temperature could further constrain the already narrow discharge and water temperature conditions optimal for successful Gaat migration.

From a fisheries management perspective, this study provides quantitative thresholds for

discharge and water temperature that can be used to guide conservation efforts. Given the rising frequency of ARs from August through October, it is likely that Gaat migration success will be increasingly influenced by hydrologic variability. However, this study does not assess long-term escapement data through formal statistical linkage to hydrometric records. To mitigate run collapses, real-time hydrometric monitoring at SR3-3 should be prioritized. Additionally, integrating traditional Taku River Tlingit First Nation (TRTFN) knowledge with hydrologic modelling will strengthen conservation efforts and ensure management approaches align with empirical data and traditional ecological insights.

Ultimately, this work underscores the intricate relationship between ARs, river hydrology, and Gaat migration success. Defining hydrometric thresholds for successful passage provides scientific evidence to support conservation policy and fisheries management decisions in the Gaat Héeni Watershed.

7.2 Study Limitations

While this study provides insights into the influence of ARs on hydrologic variability and the arrival of Gaat at Gaat Áayi, limitations will be discussed below. These relate to hydrometric data's spatial and temporal resolution, the range of observed temperature and discharge conditions, temperature and discharge extremes, video monitoring, and climate change considerations. Many patterns observed, particularly those involving Gaat passage, should be interpreted as preliminary, given the absence of formal causal analyses. Addressing these constraints in future research will improve our ability to predict and mitigate the impacts of AR-driven hydrologic extremes on Gaat migration.

One limitation concerns the discharge measurement location in relation to the video monitoring

location. Hydrometric data were collected above the confluence of Katina Creek, meaning that the discharge conditions at SR3-3 were inferred rather than directly measured. This introduces potential discrepancies in discharge estimates at the actual migration site. While the general trends in discharge variability are captured, local discharge conditions at SR3-3 will differ due to tributary inflows such as Katina Creek. Future research should deploy sensors to measure discharge at SR3-3, allowing for real-time discharge measurements at the precise location of Gaat passage. This would improve the accuracy of jump success models and provide a clearer understanding of site-specific hydrodynamics.

Another limitation relates to the resolution and reliability of ERA5-Land reanalysis data, particularly for precipitation. While ERA5-Land provides a consistent long-term dataset, it has documented biases in complex mountainous terrain, often underestimating extreme precipitation events and misrepresenting orographic effects. As a result, some AR-driven discharge responses may be underrepresented in the dataset. This limitation is particularly relevant for Section 5.6, which showed disproportionate discharge increases under high daily precipitation. Users of these results should recognize that modelled AR contributions likely represent conservative estimates of true hydrologic extremes.

A significant constraint in this study is the lack of conclusive results for extremely high and low water temperatures and river discharges. While mid-range conditions (13–15 °C and 10–12 m³ s⁻¹) were identified as optimal for Gaat passage, data on passage success under more extreme conditions (>16 m³ s⁻¹ or <9 m³ s⁻¹ discharge, and >15 °C or <9 °C water temperature) remain insufficient. This is partly due to logistical challenges in monitoring fish passage under extreme conditions and the migration window not aligning with suboptimal periods. This results from

monitoring gaps and natural migration timing, which limited observations during the most physiologically challenging conditions. Future studies should extend video monitoring efforts across a broader range of discharge and water temperature conditions, possibly using Passive Integrated Transponder (PIT) tagging to track passage attempts over multiple years.

While valuable for quantifying passage success, the study's video monitoring approach is limited by field-of-view constraints and sampling frequency. Cameras were deployed to observe jump success at SR3-3, but Gaat behaviour outside the immediate jump zone was not fully captured. Turbidity during peak discharge occasionally reduced video clarity, leading to potential undercounting of failed passage attempts. Additionally, the inability to safely conduct observations during periods of elevated discharge (the 22-24 July AR event) further limited data collection under elevated hydrologic conditions. Future research should consider alternative monitoring techniques, such as PIT tagging (Hemeon et al., 2024) or infrared imaging (Hiebert et al., 2000), which may provide more consistent passage observations under various hydrologic conditions.

Finally, this study does not include future climate projections, which limits long-term conservation planning. While historical AR frequency and intensity trends were analyzed, the study does not predict how future warming and altered precipitation patterns may affect Gaat migration conditions. Incorporating climate scenarios would enhance the applicability of these findings for proactive fisheries management and long-term habitat planning.

7.3 Future Direction

The recognition of changing AR intensity and spatial distribution (Gershunov et al., 2019; Payne et al., 2020), alongside their demonstrated local hydrometric impacts, underscores the urgency of

acquiring high-resolution, year-round hydrometric and biological data in salmonid-bearing watersheds vulnerable to extreme events (Bellmore et al., 2023). Improved monitoring capacity is essential to anticipating, understanding, and mitigating the ecological consequences of intensifying AR regimes under climate change.

One research priority is the expansion of long-term, individual-based tracking across variable discharge conditions. PIT tagging enables continuous monitoring of fish passage across migration barriers (Hemeon et al., 2024), capturing repeat attempts, fallback events, and movement patterns with acceptable temporal resolution (Haro & Castro-Santos, 2012). When coupled with antenna arrays strategically installed at hydraulic constriction points such as SR3-3, PIT tagging serves as a complementary and non-invasive method to video monitoring, particularly under turbid, low-light, or spray-obscured conditions (Bateman et al., 2009). Future PIT-based studies should span multiple migration seasons to capture interannual variability in fish behaviour and barrier navigability, with antennas also deployed downstream of Katina Creek to resolve discharge dynamics influencing passage feasibility.

To refine visual monitoring, future work should trial multi-angle video arrays to enhance detection coverage, especially for Gaats passage events that occur behind the waterfall or under variable visibility conditions. While thermal or infrared imagery may marginally improve detectability in low-light or obscured conditions (Hiebert et al., 2000), their efficacy remains uncertain due to the ectothermic nature of Gaats. Machine learning–assisted video classification (Saberioon et al., 2017) offers significant potential to automate behavioural annotation, reduce manual processing time, and increase consistency across reviewers. These tools should be validated against PIT or sonar-based observations to evaluate detection accuracy and

classification precision under variable discharge and lighting regimes.

It is important to note that escapement reflects cumulative freshwater and marine influences, including ocean survival, predation, and pre-spawn mortality (Rand et al., 2006). As such, hydrologic factors observed here represent only one potential constraint within a broader suite of environmental pressures. While descriptive comparisons of paired hydrologic and escapement years highlight possible linkages, the current dataset does not support inferential testing. Future efforts should explicitly test these relationships with multi-decadal escapement, discharge, and water temperature datasets.

To address these limitations, future research should focus on advancing predictive, multi-scale modelling approaches, expanding long-term fish tracking technologies, and integrating climate change scenarios into Gaat migration assessments. These long-term datasets will be invaluable for understanding how Gaat populations respond to shifting AR-driven hydrology over multiple generations. To support this, a hydrometric station should be installed below the Katina Creek confluence to account for potential discharges affecting SR3-3. Existing measurements upstream of the confluence may underestimate the actual discharge conditions encountered by migrating Gaat at the SR3-3. Future studies could develop predictive models using deep learning algorithms to forecast migration success based on real-time hydrometric conditions. This would enable fisheries managers to implement adaptive conservation strategies that optimize passage success during critical migration windows.

REFERENCES

- Adam, J. C., Hamlet, A. F., & Lettenmaier, D. P. (2009). Implications of global climate change for snowmelt hydrology in the twenty-first century. *Hydrological Processes*, 23(7), 962–972. <https://doi.org/10.1002/hyp.7201>
- Aitken, J. D. (1958). *Atlin map-area* (Memoir No. 307).
- Armstrong, J. B., Ward, E. J., Schindler, D. E., & Lisi, P. J. (2016). Adaptive capacity at the northern front: Sockeye Salmon behaviourally thermoregulate during novel exposure to warm temperatures. *Conservation Physiology*, 4(1), <https://doi.org/10.1093/conphys/cow039>
- Arora, V. K., Lima, A., & Shrestha, R. (2025). The effect of climate change on the simulated streamflow of six Canadian rivers based on the CanRCM4 regional climate model. *Hydrology and Earth System Sciences*, 29(1), 291–312. <https://doi.org/10.5194/hess-29-291-2025>
- Atlas, W. I., Seitz, K. M., Jorgenson, J. W. N., Millard-Martin, B., Housty, W. G., Ramos-Espinoza, D., Burnett, N. J., Reid, M., & Moore, J. W. (2021). Thermal sensitivity and flow-mediated migratory delays drive climate risk for coastal Sockeye Salmon. *FACETS*, 6(1), Article 1. <https://doi.org/10.1139/facets-2020-0027>
- Bateman, D. S., Gresswell, R. E., & Berger, A. M. (2009). Passive integrated transponder tag retention rates in headwater populations of Coastal Cutthroat Trout. *North American Journal of Fisheries Management*, 29(3), 653–657. <https://doi.org/10.1577/M07-169.1>
- Bathurst, J. C., Birkinshaw, S. J., Cisneros Espinosa, F., & Iroumé, A. (2017). Forest impact on flood peak discharge and sediment yield in streamflow. In N. Sharma (Ed.), *River System Analysis and Management* (pp. 15–29). Springer Singapore. https://doi.org/10.1007/978-981-10-1472-7_2
- Beacham, T. D., Cox-Rogers, S., MacConnachie, C., McIntosh, B., & Wallace, C. G. (2014). Population structure and run timing of Sockeye Salmon in the Skeena River, British Columbia. *North American Journal of Fisheries Management*, 34(2), 335–348. <https://doi.org/10.1080/02755947.2014.880761>
- Beacham, T. D., McIntosh, B., & MacConnachie, C. (2004). Population structure of lake-type and river-type sockeye salmon in transboundary rivers of northern British Columbia. *Journal of Fish Biology*, 65(2), 389–402. <https://doi.org/10.1111/j.0022-1112.2004.00457.x>
- Beamish, R. J., Neville, C. M., Sweeting, R. M., Beacham, T. D., Wade, J., & Li, L. (2016). Early ocean life history of Harrison River Sockeye Salmon and their contribution to the biodiversity of Sockeye Salmon in the Fraser River, British Columbia, Canada. *Transactions of the American Fisheries Society*, 145(2). <https://doi.org/10.1080/00028487.2015.1123182>
- Bellmore, J. R., Sergeant, C. J., Bellmore, R. A., Falke, J. A., & Fellman, J. B. (2023). Modeling Coho Salmon (*Oncorhynchus kisutch*) population response to streamflow and water temperature extremes. *Canadian Journal of Fisheries and Aquatic Sciences*, 80(2), Article 2. <https://doi.org/10.1139/cjfas-2022-0129>

- Birnie-Gauvin, K., Patterson, D. A., Cooke, S. J., Hinch, S. G., & Eliason, E. J. (2023). Anaerobic exercise and recovery: roles and implications for mortality in Pacific Salmon. *Reviews in Fisheries Science & Aquaculture*, 31(4), 497–522. <https://doi.org/10.1080/23308249.2023.2224902>
- Blöschl, G. (1991). The influence of uncertainty in air temperature and albedo on snowmelt. *Hydrology Research*, 22(2), 95–108. <https://doi.org/10.2166/nh.1991.0007>
- Bolker, B. M., Brooks, M. E., Clark, C. J., Geange, S. W., Poulsen, J. R., Stevens, M. H. H., & White, J.-S. S. (2009). Generalized linear mixed models: A practical guide for ecology and evolution. *Trends in Ecology & Evolution*, 24(3), 127–135. <https://doi.org/10.1016/j.tree.2008.10.008>
- Brett, J. R. (1971). Energetic responses of Salmon to temperature: A study of some thermal relations in the physiology and freshwater ecology of Sockeye Salmon (*Oncorhynchus nerka*). *American Zoologist*, 11(1), 99–113. <https://doi.org/10.1093/icb/11.1.99>
- Burt, J. M., Hinch, S. G., & Patterson, D. A. (2012). Developmental temperature stress and parental identity shape offspring burst swimming performance in Sockeye Salmon (*Oncorhynchus nerka*). *Ecology of Freshwater Fish*, 21(2), Article 2. <https://doi.org/10.1111/j.1600-0633.2011.00535.x>
- Carey, M. P., Keith, K. D., Schelske, M., Lean, C., McCormick, S. D., Regish, A., & Zimmerman, C. E. (2019). Energy Depletion and Stress Levels in Sockeye Salmon Migrating at the Northern Edge of their Distribution. *Transactions of the American Fisheries Society*, 148(4), 785–797. <https://doi.org/10.1002/tafs.10172>
- Carey, M. P., Zimmerman, C. E., Keith, K. D., Schelske, M., Lean, C., & Douglas, D. C. (2017). Migration trends of Sockeye Salmon at the northern edge of their distribution. *Transactions of the American Fisheries Society*, 146(4), 791–802. <https://doi.org/10.1080/00028487.2017.1302992>
- Caudill, C. C., Daigle, W. R., Keefer, M. L., Boggs, C. T., Jepson, M. A., Burke, B. J., Zabel, R. W., Bjornn, T. C., & Peery, C. A. (2007). Slow dam passage in adult Columbia River salmonids associated with unsuccessful migration: delayed negative effects of passage obstacles or condition-dependent mortality? *Canadian Journal of Fisheries and Aquatic Sciences*, 64(7), 979–995. <https://doi.org/10.1139/f07-065>
- Chen, J., Brissette, F. P., Chaumont, D., & Braun, M. (2013). Finding appropriate bias correction methods in downscaling precipitation for hydrologic impact studies over North America. *Water Resources Research*, 49(7), 4187–4205. <https://doi.org/10.1002/wrcr.20331>
- Clelland, A. A., Marshall, G. J., & Baxter, R. (2024). Evaluating the performance of key ERA-Interim, ERA5 and ERA5-Land climate variables across Siberia. *International Journal of Climatology*, 44(7), 2318–2342. <https://doi.org/10.1002/joc.8456>
- Comiti, F., Lucía, A., & Rickenmann, D. (2016). Large wood recruitment and transport during large floods: A review. *Geomorphology*, 269, 23–39. <https://doi.org/10.1016/j.geomorph.2016.06.016>

- Copernicus Climate Change Service. (2019). *ERA5-Land hourly data from 1950 to present* [Dataset]. Copernicus Climate Change Service (C3S) Climate Data Store (CDS). <https://doi.org/10.24381/CDS.E2161BAC>
- Crossin, G. T., Hinch, S. G., Cooke, S. J., Cooperman, M. S., Patterson, D. A., Welch, D. W., Hanson, K. C., Olsson, I., English, K. K., & Farrell, A. P. (2009). Mechanisms influencing the timing and success of reproductive migration in a capital breeding semelparous fish species, the Sockeye Salmon. *Physiological and Biochemical Zoology*, 82(6), 635–652. <https://doi.org/10.1086/605878>
- Crossin, G. T., Hinch, S. G., Cooke, S. J., Welch, D. W., Patterson, D. A., Jones, S. R. M., Lotto, A. G., Leggatt, R. A., Mathes, M. T., Shrimpton, J. M., Van Der Kraak, G., & Farrell, A. P. (2008). Exposure to high temperature influences the behaviour, physiology, and survival of Sockeye Salmon during spawning migration. *Canadian Journal of Zoology*, 86(2), 127–140. <https://doi.org/10.1139/Z07-122>
- Crossin, G. T., Hinch, S. G., Farrell, A. P., Higgs, D. A., Lotto, A. G., Oakes, J. D., & Healey, M. C. (2004). Energetics and morphology of Sockeye Salmon: Effects of upriver migratory distance and elevation. *Journal of Fish Biology*, 65(3), 788–810. <https://doi.org/10.1111/j.0022-1112.2004.00486.x>
- Crozier, L. G., Scheuerell, M. D., & Zabel, R. W. (2011). Using time series analysis to characterize evolutionary and plastic responses to environmental change: a case study of a shift toward earlier migration date in Sockeye Salmon. *The American Naturalist*, 178(6), 755–773. <https://doi.org/10.1086/662669>
- Crozier, L. G., Siegel, J. E., Wiesebron, L. E., Trujillo, E. M., Burke, B. J., Sandford, B. P., & Widener, D. L. (2020). Snake River Sockeye and Chinook salmon in a changing climate: implications for upstream migration survival during recent extreme and future climates. *PLOS ONE*, 15(9), Article 9. <https://doi.org/10.1371/journal.pone.0238886>
- Cruz-Jesus, F., Oliveira, T., Bacao, F., & Irani, Z. (2017). Assessing the pattern between economic and digital development of countries. *Information Systems Frontiers*, 19(4), 835–854. <https://doi.org/10.1007/s10796-016-9634-1>
- Cunningham, C. J., Westley, P. A. H., & Adkison, M. D. (2018). Signals of large scale climate drivers, hatchery enhancement, and marine factors in Yukon River Chinook Salmon survival revealed with a bayesian life history model. *Global Change Biology*, 24(9), Article 9. <https://doi.org/10.1111/gcb.14315>
- Davie, T., & Quinn, N. W. (2019). *Fundamentals of Hydrology* (Third edition). Routledge, Taylor & Francis Group.
- Déry, S. J., Stadnyk, T. A., MacDonald, M. K., & Gauli-Sharma, B. (2016). Recent trends and variability in river discharge across northern Canada. *Hydrology and Earth System Sciences*, 20(12), 4801–4818. <https://doi.org/10.5194/hess-20-4801-2016>
- Dettinger, M. (2011). Climate change, atmospheric rivers, and floods in California - a multimodel analysis of storm frequency and magnitude changes. *JAWRA Journal of the American Water Resources Association*, 47(3). <https://doi.org/10.1111/j.1752-1688.2011.00546.x>

- Dickson, N. E., Carrivick, J. L., & Brown, L. E. (2012). Flow regulation alters alpine river thermal regimes. *Journal of Hydrology*, 464–465, 505–516. <https://doi.org/10.1016/j.jhydrol.2012.07.044>
- Dingman, S. L. (2015). *Physical Hydrology* (3rd ed.). Waveland Press, Long Grove, IL.
- Dockery, D. R., McMahon, T. E., Kappenman, K. M., & Blank, M. (2017). Evaluation of swimming performance for fish passage of Longnose Dace *Rhinichthys Cataractae* using an experimental flume. *Journal of Fish Biology*, 90(3), 980–1000. <https://doi.org/10.1111/jfb.13217>
- Eiler, J. H., Nelson, B. D., & Bradshaw, R. F. (1992). Riverine spawning by Sockeye Salmon in the Taku River, Alaska and British Columbia. *Transactions of the American Fisheries Society*, 121(6), 701–708. [https://doi.org/10.1577/1548-8659\(1992\)121<0701:RSBSSI>2.3.CO;2](https://doi.org/10.1577/1548-8659(1992)121<0701:RSBSSI>2.3.CO;2)
- Eiras-Barca, J., Ramos, A. M., Pinto, J. G., Trigo, R. M., Liberato, M. L. R., & Miguez-Macho, G. (2018). The concurrence of atmospheric rivers and explosive cyclogenesis in the North Atlantic and North Pacific basins. *Earth System Dynamics*, 9(1), 91–102. <https://doi.org/10.5194/esd-9-91-2018>
- Eliason, E. J., Clark, T. D., Hague, M. J., Hanson, L. M., Gallagher, Z. S., Jeffries, K. M., Gale, M. K., Patterson, D. A., Hinch, S. G., & Farrell, A. P. (2011). Differences in thermal tolerance among Sockeye Salmon populations. *Science*, 332(6025), Article 6025. <https://doi.org/10.1126/science.1199158>
- Enders, E. C., Gessel, M. H., & Williams, J. G. (2009). Development of successful fish passage structures for downstream migrants requires knowledge of their behavioural response to accelerating flow. *Canadian Journal of Fisheries and Aquatic Sciences*, 66(12), 2109–2117. <https://doi.org/10.1139/F09-141>
- English, K. K., Koski, W. R., Sliwinski, C., Blakley, A., Cass, A., & Woodey, J. C. (2005). Migration timing and river survival of late-run Fraser River Sockeye Salmon estimated using radiotelemetry techniques. *Transactions of the American Fisheries Society*, 134(5), 1342–1365. <https://doi.org/10.1577/T04-119.1>
- Environment and Climate Change Canada. (2024). *Atlin 1981-2010 Station Data* [Dataset]. https://climate.weather.gc.ca/climate_normals/results_1981_2010_e.html?stnID=1485&autofwd=1
- Espinoza, V., Waliser, D. E., Guan, B., Lavers, D. A., & Ralph, F. M. (2018). Global analysis of climate change projection effects on atmospheric rivers. *Geophysical Research Letters*, 45(9), 4299–4308. <https://doi.org/10.1029/2017GL076968>
- Fallot, J.-M., Barry, R. G., & Hoogstrate, D. (1997). Variations of mean cold season temperature, precipitation and snow depths during the last 100 years in the former Soviet Union (FSU). *Hydrological Sciences Journal*, 42(3), 301–327. <https://doi.org/10.1080/02626669709492031>
- Farley, E. V., Murphy, J. M., Adkison, M., & Eisner, L. (2007). Juvenile Sockeye Salmon distribution, size, condition and diet during years with warm and cool spring sea temperatures along the eastern Bering Sea shelf. *Journal of Fish Biology*, 71(4), 1145–1158. <https://doi.org/10.1111/j.1095-8649.2007.01587.x>

- Farrell, A. P. (2009). Environment, antecedents and climate change: Lessons from the study of temperature physiology and river migration of salmonids. *Journal of Experimental Biology*, 212(23). <https://doi.org/10.1242/jeb.023671>
- Feddern, M. L., Schoen, E. R., Shaftel, R., Cunningham, C. J., Chythlook, C., Connors, B. M., Murdoch, A. D., Von Biela, V. R., & Woods, B. (2023). Kings of the north: bridging disciplines to understand the effects of changing climate on Chinook Salmon in the Arctic-Yukon-Kuskokwim Region. *Fisheries*, 48(8). <https://doi.org/10.1002/fsh.10923>
- Fisheries, N. (2025, January 4). *Sockeye Salmon* | NOAA Fisheries. NOAA. <https://www.fisheries.noaa.gov/species/sockeye-salmon>
- Foote, C. J., Brown, G. S., & Hawryshyn, C. W. (2004). Female colour and male choice in Sockeye Salmon: Implications for the phenotypic convergence of anadromous and nonanadromous morphs. *Animal Behaviour*, 67(1), 69–83. <https://doi.org/10.1016/j.anbehav.2003.02.004>
- Foster, L. M., Bearup, L. A., Molotch, N. P., Brooks, P. D., & Maxwell, R. M.. (2016). Energy budget increases reduce mean streamflow more than snow–rain transitions: using integrated modeling to isolate climate change impacts on Rocky Mountain hydrology. *Environmental Research Letters*, 11(4). <https://doi.org/10.1088/1748-9326/11/4/044015>
- Frandsen, S. L., & Hasselbalch, J. A. (2024). Who are the green transition experts? Towards a new research agenda on climate change knowledge. *WIREs Climate Change*, 15(6), e917. <https://doi.org/10.1002/wcc.917>
- Fraser, C., & Jackson, S. (2018). Shifts in air temperature and high-magnitude winter precipitation events in coastal North America: implications for environmental assessment and management. *Integrated Environmental Assessment and Management*, 14(2). <https://doi.org/10.1002/ieam.2012>
- Gautam, S. S., & Singh, V. (2022). Adaptive discretization using golden section to aid outlier detection for software development effort estimation. *IEEE Access*, 10, 90369–90387. <https://doi.org/10.1109/ACCESS.2022.3200149>
- Gerlach, T. (2011). Volcanic versus anthropogenic carbon dioxide. *Eos, Transactions American Geophysical Union*, 92(24), 201–202. <https://doi.org/10.1029/2011EO240001>
- Gershunov, A., Shulgina, T., Clemesha, R. E. S., Guirguis, K., Pierce, D. W., Dettinger, M. D., Lavers, D. A., Cayan, D. R., Polade, S. D., Kalansky, J., & Ralph, F. M. (2019). Precipitation regime change in Western North America: the role of atmospheric rivers. *Scientific Reports*, 9(1), 9944. <https://doi.org/10.1038/s41598-019-46169-w>
- Gershunov, A., Shulgina, T., Ralph, F. M., Lavers, D. A., & Rutz, J. J. (2017). Assessing the climate-scale variability of atmospheric rivers affecting western North America. *Geophysical Research Letters*, 44(15). <https://doi.org/10.1002/2017GL074175>
- Gimeno, L., Stohl, A., Trigo, R. M., Dominguez, F., Yoshimura, K., Yu, L., Drumond, A., Durán-Quesada, A. M., & Nieto, R. (2012). Oceanic and terrestrial sources of continental precipitation. *Reviews of Geophysics*, 50(4), Article 4. <https://doi.org/10.1029/2012RG000389>
- Glossary of Meteorology*. (2022). American Meteorological Society.

- Gomis-Cebolla, J., Rattayova, V., Salazar-Galán, S., & Francés, F. (2023). Evaluation of ERA5 and ERA5-Land reanalysis precipitation datasets over Spain (1951–2020). *Atmospheric Research*, 284, 106606. <https://doi.org/10.1016/j.atmosres.2023.106606>
- Gonia, T. M., Keefer, M. L., Bjornn, T. C., Peery, C. A., Bennett, D. H., & Stuehrenberg, L. C. (2006). Behavioral thermoregulation and slowed migration by adult fall Chinook Salmon in response to high Columbia River water temperatures. *Transactions of the American Fisheries Society*, 135(2). <https://doi.org/10.1577/T04-113.1>
- Government of British Columbia. (2024). *Atlin Lake (4E02B)*. <https://bcmoe-prod.aquaticinformatics.net/Report/Show/SnowMSS.4E02B.MSS%20Report/>
- Graf, W. L. (2006). Downstream hydrologic and geomorphic effects of large dams on American rivers. *Geomorphology*, 79(3–4), 336–360. <https://doi.org/10.1016/j.geomorph.2006.06.022>
- Grantham, T. E. (2013). Use of hydraulic modelling to assess passage flow connectivity for Salmon in streams. *River Research and Applications*, 29(2), 250–267. <https://doi.org/10.1002/rra.1591>
- Guan, B., & Waliser, D. E. (2019). Tracking atmospheric rivers globally: spatial distributions and temporal evolution of life cycle characteristics. *Journal of Geophysical Research: Atmospheres*, 124(23), 12523–12552. <https://doi.org/10.1029/2019JD031205>
- Guo, Y., Shinoda, T., Guan, B., Waliser, D. E., & Chang, E. K. M. (2020). Statistical relationship between atmospheric rivers and extratropical cyclones and anticyclones. *Journal of Climate*, 33(18), 7817–7834. <https://doi.org/10.1175/JCLI-D-19-0126.1>
- Hague, M. J., Ferrari, M. R., Miller, J. R., Patterson, D. A., Russell, G. L., Farrell, A. P., & Hinch, S. G. (2011). Modelling the future hydroclimatology of the lower Fraser River and its impacts on the spawning migration survival of sockeye salmon: Sockeye Salmon migratory survival. *Global Change Biology*, 17(1), 87–98. <https://doi.org/10.1111/j.1365-2486.2010.02225.x>
- Hall, B. D., Saunders, P., & White, D. R. (2024). *Digital representation of scales and units for temperature and related quantities*. 020005. <https://doi.org/10.1063/5.0235453>
- Hanson, A. J., & Smith, H. D. (1967). Mate selection in a population of Sockeye Salmon (*Oncorhynchus nerka*) of mixed age-groups. *Journal of the Fisheries Research Board of Canada*, 24(9), 1955–1977. <https://doi.org/10.1139/f67-160>
- Hanson, K. C., Cooke, S. J., Hinch, S. G., Crossin, G. T., Patterson, D. A., English, K. K., Donaldson, M. R., Shrimpton, J. M., Van Der Kraak, G., & Farrell, A. P. (2008). Individual variation in migration speed of upriver-migrating Sockeye Salmon in the Fraser River in relation to their physiological and energetic status at marine approach. *Physiological and Biochemical Zoology*, 81(3), 255–268. <https://doi.org/10.1086/529460>
- Haro, A., & Castro-Santos, T. (2012). Passage of American Shad: paradigms and realities. *Marine and Coastal Fisheries*, 4(1), 252–261. <https://doi.org/10.1080/19425120.2012.675975>

- Harrison, X. A., Donaldson, L., Correa-Cano, M. E., Evans, J., Fisher, D. N., Goodwin, C. E. D., Robinson, B. S., Hodgson, D. J., & Inger, R. (2018). A brief introduction to mixed effects modelling and multi-model inference in ecology. *PeerJ*, 6, e4794. <https://doi.org/10.7717/peerj.4794>
- Hauer, C., Unfer, G., Tritthart, M., & Habersack, H. (2011). Effects of stream channel morphology, transport processes and effective discharge on salmonid spawning habitats. *Earth Surface Processes and Landforms*, 36(5), 672–685. <https://doi.org/10.1002/esp.2087>
- Hawcroft, M. K., Shaffrey, L. C., Hodges, K. I., & Dacre, H. F. (2012). How much Northern Hemisphere precipitation is associated with extratropical cyclones? *Geophysical Research Letters*, 39(24), 2012GL053866. <https://doi.org/10.1029/2012GL053866>
- Hay, L. E., & McCabe, G. J. (2010). Hydrologic effects of climate change in the Yukon River Basin. *Climatic Change*, 100(3–4), 509–523. <https://doi.org/10.1007/s10584-010-9805-x>
- Hemeon, K. M., Peterson, D. P., Twibell, R. G., Kennedy, B. M., & Piteo, M. S. (2024). Rates of PIT tag ingestion and gastric retention in three species of hatchery-reared salmonids and potential implications for postrelease monitoring. *North American Journal of Fisheries Management*, 44(6), 1489–1511. <https://doi.org/10.1002/nafm.11050>
- Henderson, M. A., Levy, D. A., & Stockner, J. S. (1992). Probable consequences of climate change on freshwater production of Adams River sockeye salmon (*Oncorhynchus nerka*). *GeoJournal*, 28(1), 51–59. <https://doi.org/10.1007/BF00216406>
- Hersbach, H., Bell, B., Berrisford, P., Hirahara, S., Horányi, A., Muñoz-Sabater, J., Nicolas, J., Peubey, C., Radu, R., Schepers, D., Simmons, A., Soci, C., Abdalla, S., Abellan, X., Balsamo, G., Bechtold, P., Biavati, G., Bidlot, J., Bonavita, M., ... Thépaut, J. (2020). The ERA5 global reanalysis. *Quarterly Journal of the Royal Meteorological Society*, 146(730), 1999–2049. <https://doi.org/10.1002/qj.3803>
- Hiebert, S., Helfrich, L. A., Weigmann, D. L., & Liston, C. (2000). Anadromous Salmonid passage and video image quality under infrared and visible light at Prosser Dam, Yakima River, Washington. *North American Journal of Fisheries Management*, 20(3), 827–832. [https://doi.org/10.1577/1548-8675\(2000\)020<0827:ASPAVI>2.3.CO;2](https://doi.org/10.1577/1548-8675(2000)020<0827:ASPAVI>2.3.CO;2)
- Hinch, S. G., & Bratty, J. (2000). Effects of swim speed and activity pattern on success of adult Sockeye Salmon migration through an area of difficult passage. *Transactions of the American Fisheries Society*, 129(2), 598–606. [https://doi.org/10.1577/1548-8659\(2000\)129<0598:EOSSAA>2.0.CO;2](https://doi.org/10.1577/1548-8659(2000)129<0598:EOSSAA>2.0.CO;2)
- Hinch, S. G., & Rand, P. S. (1998). Swim speeds and energy use of upriver-migrating Sockeye Salmon (*Oncorhynchus nerka*): Role of local environment and fish characteristics. *Canadian Journal of Fisheries and Aquatic Sciences*, 55(8), 1821–1831. <https://doi.org/10.1139/f98-067>
- Hooke, J. M. (1979). An analysis of the processes of river bank erosion. *Journal of Hydrology*, 42(1–2), 39–62. [https://doi.org/10.1016/0022-1694\(79\)90005-2](https://doi.org/10.1016/0022-1694(79)90005-2)
- Hosmer, D. W., Lemeshow, S., & Sturdivant, R. X. (2013). *Applied Logistic Regression* (Third edition). Wiley.

- Howard, K. G., & Von Biela, V. (2023). Adult spawners: A critical period for subarctic Chinook salmon in a changing climate. *Global Change Biology*, 29(7), 1759–1773. <https://doi.org/10.1111/gcb.16610>
- Hruska, K. A., Hinch, S. G., Healey, M. C., Patterson, D. A., Larsson, S., & Farrell, A. P. (2010). Influences of sex and activity level on physiological changes in individual adult Sockeye Salmon during rapid senescence. *Physiological and Biochemical Zoology*, 83(4), 663–676. <https://doi.org/10.1086/652411>
- Huang, S., Krysanova, V., Zhai, J., & Su, B. (2015). Impact of intensive irrigation activities on river discharge under agricultural scenarios in the semi-arid Aksu River Basin, Northwest China. *Water Resources Management*, 29(3), 945–959. <https://doi.org/10.1007/s11269-014-0853-2>
- Ide, J., Finér, L., Laurén, A., Piirainen, S., & Launiainen, S. (2013). Effects of clear-cutting on annual and seasonal runoff from a boreal forest catchment in eastern Finland. *Forest Ecology and Management*, 304, 482–491. <https://doi.org/10.1016/j.foreco.2013.05.051>
- IPCC. (2025). *Special Report: Global Warming of 1.5 °C*. <https://www.ipcc.ch/sr15/chapter/glossary/>
- Islam, S. U., Hay, R. W., Déry, S. J., & Booth, B. P. (2019). Modelling the impacts of climate change on riverine thermal regimes in western Canada's largest Pacific watershed. *Scientific Reports*, 9(1), 11398. <https://doi.org/10.1038/s41598-019-47804-2>
- Jeffries, K. M., Hinch, S. G., Sierocinski, T., Clark, T. D., Eliason, E. J., Donaldson, M. R., Li, S., Pavlidis, P., & Miller, K. M. (2012). Consequences of high temperatures and premature mortality on the transcriptome and blood physiology of wild adult Sockeye Salmon (*Oncorhynchus nerka*). *Ecology and Evolution*, 2(7), 1747–1764. <https://doi.org/10.1002/ece3.274>
- Jeoung, H., Shi, S., & Liu, G. (2022). A novel approach to validate satellite snowfall retrievals by ground-based point measurements. *Remote Sensing*, 14(3), 434. <https://doi.org/10.3390/rs14030434>
- Kalnay, E., Kanamitsu, M., Kistler, R., Collins, W., Deaven, D., Gandin, L., Iredell, M., Saha, S., White, G., Woollen, J., Zhu, Y., Leetmaa, A., Reynolds, R., Chelliah, M., Ebisuzaki, W., Higgins, W., Janowiak, J., Mo, K. C., Ropelewski, C., ... Joseph, D. (1996). The NCEP/NCAR 40-year reanalysis project. *Bulletin of the American Meteorological Society*, 77(3), 437–471. [https://doi.org/10.1175/1520-0477\(1996\)077<0437:TNYRP>2.0.CO;2](https://doi.org/10.1175/1520-0477(1996)077<0437:TNYRP>2.0.CO;2)
- Kang, D. H., Shi, X., Gao, H., & Déry, S. J. (2014). On the changing contribution of snow to the hydrology of the Fraser River Basin, Canada. *Journal of Hydrometeorology*, 15(4), 1344–1365. <https://doi.org/10.1175/JHM-D-13-0120.1>
- Kattel, D. B., & Yao, T. (2018). Temperature–topographic elevation relationship for high mountain terrain: An example from the southeastern Tibetan Plateau. *International Journal of Climatology*, 38(S1). <https://doi.org/10.1002/joc.5418>
- Kendall, M. G. (1948). *Rank Correlation Methods*. https://www.cambridge.org/core/product/identifier/S0020268100013019/type/journal_article

- Khrustaleva, A. (2024). Spatial and ecological structure of the Sockeye Salmon population *Oncorhynchus nerka* of Kuril Lake. *E3S Web of Conferences*, 548, 07010. <https://doi.org/10.1051/e3sconf/202454807010>
- Kocan, R., LaPatra, S., Gregg, J., Winton, J., & Hershberger, P. (2006). *Ichthyophonus*-induced cardiac damage: A mechanism for reduced swimming stamina in salmonids. *Journal of Fish Diseases*, 29(9), 521–527. <https://doi.org/10.1111/j.1365-2761.2006.00745.x>
- Kolot, J., Mischler, A., Bier, A., & Goulding, H. (2021). *Yukon snow survey bulletin and water supply forecast*. Yukon Government.
- Kouki, K., Luojus, K., & Riihelä, A. (2023). Evaluation of snow cover properties in ERA5 and ERA5-Land with several satellite-based datasets in the Northern Hemisphere in spring 1982–2018. *The Cryosphere*, 17(12), 5007–5026. <https://doi.org/10.5194/tc-17-5007-2023>
- Lauritzen, D. V., Hertel, F., & Gordon, M. S. (2005). A kinematic examination of wild Sockeye Salmon jumping up natural waterfalls. *Journal of Fish Biology*, 67(4), 1010–1020. <https://doi.org/10.1111/j.0022-1112.2005.00799.x>
- Lavers, D. A., Ralph, F. M., Richardson, D. S., & Pappenberger, F. (2020). Improved forecasts of atmospheric rivers through systematic reconnaissance, better modelling, and insights on conversion of rain to flooding. *Communications Earth & Environment*, 1(1), Article 1. <https://doi.org/10.1038/s43247-020-00042-1>
- Lazic, S. E., Mellor, J. R., Ashby, M. C., & Munafo, M. R. (2020). A Bayesian predictive approach for dealing with pseudoreplication. *Scientific Reports*, 10(1), 2366. <https://doi.org/10.1038/s41598-020-59384-7>
- Lenzi, M. A., Mao, L., & Comiti, F. (2006). Effective discharge for sediment transport in a mountain river: Computational approaches and geomorphic effectiveness. *Journal of Hydrology*, 326(1–4), 257–276. <https://doi.org/10.1016/j.jhydrol.2005.10.031>
- Li, Y., Sun, F., Chen, Y., Fang, G., Li, Z., Duan, W., Qin, J., Zhang, X., & Li, B. (2025). Unraveling the complexities of rain-on-snow events in High Mountain Asia. *Npj Climate and Atmospheric Science*, 8(1), 118. <https://doi.org/10.1038/s41612-025-00943-y>
- Li, Y., Zeng, Z., Zhao, L., & Piao, S. (2015). Spatial patterns of climatological temperature lapse rate in mainland China: A multi-time scale investigation. *Journal of Geophysical Research: Atmospheres*, 120(7), 2661–2675. <https://doi.org/10.1002/2014JD022978>
- Magnoni, L. J., Patterson, D. A., Farrell, A. P., & Weber, J.-M. (2006). Effects of long-distance migration on circulating lipids of Sockeye Salmon (*Oncorhynchus nerka*). *Canadian Journal of Fisheries and Aquatic Sciences*, 63(8), 1822–1829. <https://doi.org/10.1139/f06-083>
- Mai, J., Kornelsen, K. C., Tolson, B. A., Fortin, V., Gasset, N., Bouhemhem, D., Schäfer, D., Leahy, M., Anctil, F., & Coulibaly, P. (2020). The Canadian Surface Prediction Archive (CaSPAR): a platform to enhance environmental modeling in Canada and globally. *Bulletin of the American Meteorological Society*, 101(3), E341–E356. <https://doi.org/10.1175/BAMS-D-19-0143.1>
- Mann, H. B. (1945). Nonparametric tests against trend. *Econometrica*, 13(245).

- Martins, E. G., Hinch, S. G., Patterson, D. A., Hague, M. J., Cooke, S. J., Miller, K. M., Robichaud, D., English, K. K., & Farrell, A. P. (2012). High river temperature reduces survival of Sockeye Salmon (*Oncorhynchus nerka*) approaching spawning grounds and exacerbates female mortality. *Canadian Journal of Fisheries and Aquatic Sciences*, 69(2), 330–342. <https://doi.org/10.1139/f2011-154>
- Mathers, K. L., Robinson, C. T., & Weber, C. (2022). Patchiness in flow refugia use by macroinvertebrates following an artificial flood pulse. *River Research and Applications*, 38(4), 696–707. <https://doi.org/10.1002/rra.3941>
- Mathes, M. T., Hinch, S. G., Cooke, S. J., Crossin, G. T., Patterson, D. A., Lotto, A. G., & Farrell, A. P. (2010). Effect of water temperature, timing, physiological condition, and lake thermal refugia on migrating adult Weaver Creek sockeye salmon (*Oncorhynchus nerka*). *Canadian Journal of Fisheries and Aquatic Sciences*, 67(1), 70–84. <https://doi.org/10.1139/F09-158>
- Mattikalli, N. M., Devereux, B. J., & Richards, K. S. (1996). Prediction of river discharge and surface water quality using an integrated geographical information system approach. *International Journal of Remote Sensing*, 17(4), 683–701. <https://doi.org/10.1080/01431169608949038>
- Maynard, G. A., Kinnison, M. T., & Zydlewski, J. D. (2017). Size selection from fishways and potential evolutionary responses in a threatened Atlantic Salmon population. *River Research and Applications*, 33(7), 1004–1015. <https://doi.org/10.1002/rra.3155>
- McArdle, B. H. (1988). The structural relationship: regression in biology. *Canadian Journal of Zoology*, 66(11), 2329–2339. <https://doi.org/10.1139/z88-348>
- Milliman, J. D., Farnsworth, K. L., Jones, P. D., Xu, K. H., & Smith, L. C. (2008). Climatic and anthropogenic factors affecting river discharge to the global ocean, 1951–2000. *Global and Planetary Change*, 62(3–4), 187–194. <https://doi.org/10.1016/j.gloplacha.2008.03.001>
- Modarres, R., & Ouarda, T. B. M. J. (2013). Modeling rainfall–runoff relationship using multivariate GARCH model. *Journal of Hydrology*, 499, 1–18. <https://doi.org/10.1016/j.jhydrol.2013.06.044>
- Morton, W. M. (1965). The taxonomic significance of the kype in American Salmonids. *Copeia*, 1965(1), 14. <https://doi.org/10.2307/1441233>
- Mosley, M. P. (1982). Analysis of the effect of changing discharge on channel morphology and instream uses in a braided river, Ohau River, New Zealand. *Water Resources Research*, 18(4), 800–812. <https://doi.org/10.1029/WR018i004p00800>
- Mueller, R. P., Southard, S. S., May, C. W., Pearson, W. H., & Cullinan, V. I. (2008). Juvenile Coho Salmon leaping ability and behavior in an experimental culvert test bed. *Transactions of the American Fisheries Society*, 137(4), 941–950. <https://doi.org/10.1577/T06-244.1>
- Muñoz, S. E., Hamilton, B., & Parazin, B. (2023). Contrasting ocean–atmosphere dynamics mediate flood hazard across the Mississippi River Basin. *Earth Interactions*, 27(1). <https://doi.org/10.1175/EI-D-22-0015.1>

- Muñoz-Sabater, J., Dutra, E., Agustí-Panareda, A., Albergel, C., Arduini, G., Balsamo, G., Boussetta, S., Choulga, M., Harrigan, S., Hersbach, H., Martens, B., Miralles, D. G., Piles, M., Rodríguez-Fernández, N. J., Zsoter, E., Buontempo, C., & Thépaut, J.-N. (2021). ERA5-Land: A state-of-the-art global reanalysis dataset for land applications. *Earth System Science Data*, 13(9), 4349–4383. <https://doi.org/10.5194/essd-13-4349-2021>
- Neiman, P. J., Ralph, F. M., Wick, G. A., Lundquist, J. D., & Dettinger, M. D. (2008). Meteorological characteristics and overland precipitation impacts of atmospheric rivers affecting the west coast of North America based on eight years of SSM/I satellite observations. *Journal of Hydrometeorology*, 9(1), 22–47. <https://doi.org/10.1175/2007JHM855.1>
- Park, C., Son, S., & Kim, H. (2021). Distinct features of atmospheric rivers in the early versus late east Asian summer monsoon and their impacts on monsoon rainfall. *Journal of Geophysical Research: Atmospheres*, 126(7). <https://doi.org/10.1029/2020JD033537>
- Payne, A. E., Demory, M.E., Leung, L. R., Ramos, A. M., Shields, C. A., Rutz, J. J., Siler, N., Villarini, G., Hall, A., & Ralph, F. M. (2020). Responses and impacts of atmospheric rivers to climate change. *Nature Reviews Earth & Environment*, 1(3). <https://doi.org/10.1038/s43017-020-0030-5>
- Peng, C.Y. J., Lee, K. L., & Ingersoll, G. M. (2002). An introduction to logistic regression analysis and reporting. *The Journal of Educational Research*, 96(1), 3–14. <https://doi.org/10.1080/00220670209598786>
- Poff, N. L., Allan, J. D., Bain, M. B., Karr, J. R., Prestegard, K. L., Richter, B. D., Sparks, R. E., & Stromberg, J. C. (1997). The natural flow regime. *BioScience*, 47(11), 769–784. <https://doi.org/10.2307/1313099>
- Preston-Thomas, H. (1990). The international temperature scale of 1990 (ITS-90). *Metrologia*, 27(1), 3–10. <https://doi.org/10.1088/0026-1394/27/1/002>
- Quinn, T. P. (1988). Estimated swimming speeds of migrating adult Sockeye Salmon. *Canadian Journal of Zoology*, 66(10), 2160–2163. <https://doi.org/10.1139/z88-322>
- Quinn, T. P. (Ed.). (2005). *The behavior and ecology of Pacific Salmon and Trout*. American Fisheries Society.
- Quinn, T. P., Hodgson, S., & Peven, C. (1997). Temperature, flow, and the migration of adult sockeye salmon (*fmodel*) in the Columbia River. *Canadian Journal of Fisheries and Aquatic Sciences*, 54(6), 1349–1360. <https://doi.org/10.1139/f97-038>
- R Core Team. (2024). *R: The R project for statistical computing*. <https://www.r-project.org/>
- Radchenko, V. I., & Mathisen, O. A. (2004). Distribution, growth, and feeding of Sockeye Salmon in the western Bering Sea. *Transactions of the American Fisheries Society*, 133(3), 606–621. <https://doi.org/10.1577/T03-072.1>
- Radić, V., Cannon, A. J., Menounos, B., & Gi, N. (2015). Future changes in autumn atmospheric river events in British Columbia, Canada, as projected by CMIP5 global climate models. *Journal of Geophysical Research: Atmospheres*, 120(18), 9279–9302. <https://doi.org/10.1002/2015JD023279>

- Rahman, M. S., Senkbeil, J. C., & Keellings, D. J. (2023). Spatial and temporal variability of extreme precipitation events in the Southeastern United States. *Atmosphere*, 14(8), 1301. <https://doi.org/10.3390/atmos14081301>
- Rahmat, A., Noda, K., Onishi, T., & Senge, M. (2018). Runoff characteristics of forest watersheds under different forest managements. *Reviews in Agricultural Science*, 6, 119–133. <https://doi.org/10.7831/ras.6.119>
- Ralph, F. M., Cannon, F., Tallapragada, V., Davis, C. A., Doyle, J. D., Pappenberger, F., Subramanian, A., Wilson, A. M., Lavers, D. A., Reynolds, C. A., Haase, J. S., Centurioni, L., Ingleby, B., Rutz, J. J., Cordeira, J. M., Zheng, M., Hecht, C., Kawzenuk, B., & Delle Monache, L. (2020). West coast forecast challenges and development of atmospheric river reconnaissance. *Bulletin of the American Meteorological Society*, 101(8). <https://doi.org/10.1175/BAMS-D-19-0183.1>
- Ralph, F. M., Rutz, J. J., Cordeira, J. M., Dettinger, M., Anderson, M., Reynolds, D., Schick, L. J., & Smallcomb, C. (2019). A scale to characterize the strength and impacts of atmospheric rivers. *Bulletin of the American Meteorological Society*, 100(2). <https://doi.org/10.1175/BAMS-D-18-0023.1>
- Rand, P. S., Hinch, S. G., Morrison, J., Foreman, M. G. G., MacNutt, M. J., Macdonald, J. S., Healey, M. C., Farrell, A. P., & Higgs, D. A. (2006). Effects of river discharge, temperature, and future climates on energetics and mortality of adult migrating Fraser River Sockeye Salmon. *Transactions of the American Fisheries Society*, 135(3), 655–667. <https://doi.org/10.1577/T05-023.1>
- Ravi, S., & D’Odorico, P. (2005). A field-scale analysis of the dependence of wind erosion threshold velocity on air humidity. *Geophysical Research Letters*, 32(21). <https://doi.org/10.1029/2005GL023675>
- Reed, T. E., Schindler, D. E., Hague, M. J., Patterson, D. A., Meir, E., Waples, R. S., & Hinch, S. G. (2011). Time to evolve? Potential evolutionary responses of Fraser River Sockeye Salmon to climate change and effects on persistence. *PLoS ONE*, 6(6), e20380. <https://doi.org/10.1371/journal.pone.0020380>
- Reid, K. A., Reid, D. G., & Brown, C. D. (2022). Patterns of vegetation change in Yukon: Recent findings and future research in dynamic subarctic ecosystems. *Environmental Reviews*, 30(3), 380–401. <https://doi.org/10.1139/er-2021-0110>
- Ruggerone, G. T., & Irvine, J. R. (2018). Numbers and biomass of natural and hatchery origin Pink Salmon, Chum Salmon, and Sockeye Salmon in the North Pacific Ocean, 1925–2015. *Marine and Coastal Fisheries*, 10(2), 152–168. <https://doi.org/10.1002/mcf2.10023>
- Saberioon, M., Gholizadeh, A., Cisar, P., Pautsina, A., & Urban, J. (2017). Application of machine vision systems in aquaculture with emphasis on fish: State-of-the-art and key issues. *Reviews in Aquaculture*, 9(4), 369–387. <https://doi.org/10.1111/raq.12143>
- Sagar, B. (2023). *Llewellyn Data* [Dataset].

- Shanley, J. B., & Chalmers, A. (1999). The effect of frozen soil on snowmelt runoff at Sleepers River, Vermont. *Hydrological Processes*, 13(12–13), 1843–1857. [https://doi.org/10.1002/\(SICI\)1099-1085\(199909\)13:12/13<1843::AID-HYP879>3.0.CO;2-G](https://doi.org/10.1002/(SICI)1099-1085(199909)13:12/13<1843::AID-HYP879>3.0.CO;2-G)
- Sharma, A. R., & Déry, S. J. (2020). Contribution of atmospheric rivers to annual, seasonal, and extreme precipitation across British Columbia and Southeastern Alaska. *Journal of Geophysical Research: Atmospheres*, 125(9). <https://doi.org/10.1029/2019JD031823>
- SNAP-EWHALE. (2012). Predicting future potential climate-biomes for the Yukon, Northwest Territories and Alaska. *Scenarios Network for Arctic Planning, and Ecological Wildlife Habitat Data Analysis for the Land and Seascape Laboratory*. University of Alaska Fairbanks. <http://www.snap.uaf.edu/attachments/Cliomes-FINAL.pdf>
- Sobral, B. S., & Déry, S. J. (2023). Spatiotemporal distribution and trend analyses of atmospheric rivers affecting British Columbia's Nechako Watershed. *International Journal of Climatology*, 43(14). <https://doi.org/10.1002/joc.8230>
- Steinhausen, M. F., Sandblom, E., Eliason, E. J., Verhille, C., & Farrell, A. P. (2008). The effect of acute temperature increases on the cardiorespiratory performance of resting and swimming Sockeye Salmon (*Oncorhynchus nerka*). *Journal of Experimental Biology*, 211(24), 3915–3926. <https://doi.org/10.1242/jeb.019281>
- Sueyoshi, M., Nakano, D., & Nakamura, F. (2014). The relative contributions of refugium types to the persistence of benthic invertebrates in a seasonal snowmelt flood. *Freshwater Biology*, 59(2), 257–271. <https://doi.org/10.1111/fwb.12262>
- Surian, N., Mao, L., Giacomini, M., & Ziliani, L. (2009). Morphological effects of different channel-forming discharges in a gravel-bed river. *Earth Surface Processes and Landforms*, 34(8), 1093–1107. <https://doi.org/10.1002/esp.1798>
- Taku River Tlingit Fisheries Department. (2017). *Kuthai Lake Access Improvement Assessment*.
- Taku River Tlingit Fisheries Department. (2019). *2019 Summary Report for the Silver Salmon River Sockeye Access Improvement Project*.
- Taku River Tlingit Fisheries Department. (2022). *Silver Salmon Passage Remediation Report*.
- Tarek, M., Brissette, F. P., & Arsenault, R. (2020). Evaluation of the ERA5 reanalysis as a potential reference dataset for hydrological modelling over North America. *Hydrology and Earth System Sciences*, 24(5), 2527–2544. <https://doi.org/10.5194/hess-24-2527-2020>
- Thériault, J. M., Leroux, N. R., Tchuente, O., & Stewart, R. E. (2023). Characteristics of rain-snow transitions over the Canadian Rockies and their changes in warmer climate conditions. *Atmosphere-Ocean*, 61(5), 352–367. <https://doi.org/10.1080/07055900.2023.2251938>
- Thomas, J. O. (2010). *Fraser River Sockeye recreational hook and release mortality study*. J.O. Thomas and Associates Ltd. <https://psf.ca/wp-content/uploads/2021/10/Download-PDF152-1.pdf#:~:text=The%20mean%20fork%20length%20was,4%20cm%20for%20beach%20seined>
- Thornton, M. M., Shrestha, R., Wei, Y., Thornton, P. E., & Kao, S.-C. (2022). *Daymet: daily surface weather data on a 1-km grid for North America, version 4 R1*. ORNL Distributed Active Archive Center. <https://doi.org/10.3334/ORNLDAAAC/2129>

- Turcotte, B., Morse, B., Bergeron, N. E., & Roy, A. G. (2011). Sediment transport in ice-affected rivers. *Journal of Hydrology*, 409(1–2), 561–577. <https://doi.org/10.1016/j.jhydrol.2011.08.009>
- Tyler, A. V., Swanton, C. O., & McIntosh, B. C. (2001). *Feeding ecology of maturing Sockeye Salmon (Oncorhynchus nerka) in nearshore waters of the Kodiak Archipelago*. <https://www.boem.gov/sites/default/files/boem-newsroom/Library/Publications/2001/2001-059.pdf>
- United States Geological Survey. (2024). *USGS 15041200 TAKU R NR JUNEAU AK*.
- Vallejo-Bernal, S. M., Wolf, F., Boers, N., Traxl, D., Marwan, N., & Kurths, J. (2023). The role of atmospheric rivers in the distribution of heavy precipitation events over North America. *Hydrology and Earth System Sciences*, 27(14). <https://doi.org/10.5194/hess-27-2645-2023>
- Wagner, G. N., Hinch, S. G., Kuchel, L. J., Lotto, A., Jones, S. R., Patterson, D. A., Macdonald, J. S., Kraak, G. V. D., Shrimpton, M., English, K. K., Larsson, S., Cooke, S. J., Healey, M. C., & Farrell, A. P. (2005). Metabolic rates and swimming performance of adult Fraser River Sockeye Salmon (*Oncorhynchus nerka*) after a controlled infection with *Parvicapsula minibicornis*. *Canadian Journal of Fisheries and Aquatic Sciences*, 62(9), 2124–2133. <https://doi.org/10.1139/f05-126>
- Wang, T., Hamann, A., Spittlehouse, D., & Carroll, C. (2016). Locally downscaled and spatially customizable climate data for historical and future periods for North America. *PLOS ONE*, 11(6). <https://doi.org/10.1371/journal.pone.0156720>
- White, J. C., Hannah, D. M., House, A., Beatson, S. J. V., Martin, A., & Wood, P. J. (2017). Macroinvertebrate responses to flow and stream temperature variability across regulated and non-regulated rivers. *Ecohydrology*, 10(1). <https://doi.org/10.1002/eco.1773>
- Wickham, H. (2016). *Ggplot2*. Springer International Publishing. <https://doi.org/10.1007/978-3-319-24277-4>
- Wood, R. A., Crucifix, M., Lenton, T. M., Mach, K. J., Moore, C., New, M., Sharpe, S., Stocker, T. F., & Sutton, R. T. (2023). A climate science toolkit for high impact-low likelihood climate risks. *Earth's Future*, 11(4). <https://doi.org/10.1029/2022EF003369>
- Zhou, Y., North, J. S., Rhoades, A. M., Tao, J., Rudisill, W., Risser, M. D., & Collins, W. D. (2025). Atmospheric river frequency-category characteristics shape U.S. West coast runoff. *Journal of Geophysical Research: Atmospheres*, 130(2). <https://doi.org/10.1029/2024JD041805>